Nonlinear Experimental Modal Analysis and its Application to the Identification of Nonlinear Structures

Von der Fakultät Konstruktions-, Produktions- und Fahrzeugtechnik
der Universität Stuttgart zur Erlangung der Würde eines
Doktor-Ingenieurs (Dr.-Ing.) genehmigte Abhandlung

Vorgelegt von
Simon Peter
aus Bietigheim-Bissingen

Hauptberichter:	Prof. Dr. ir. habil. Remco I. Leine
Mitberichter:	Jun.-Prof. Dr.-Ing. Malte Krack

Tag der mündlichen Prüfung: 11.07.2018

Institut für Nichtlineare Mechanik
der Universität Stuttgart

2018

Abstract

In this work, a novel framework for nonlinear experimental modal analysis and its application to the identification of nonlinear dynamic structures is presented. The method is based on the theory of nonlinear modes, which provides a solid theoretical foundation along with intuitive concepts, such as nonlinear eigenfrequencies and mode shapes. The thesis covers a complete identification process including numerical analysis, measurement and the derivation, validation and verification of predictive models. Special emphasis is put on the development of a robust and efficient experimental method for the extraction of nonlinear modal parameters, which has been a major concern in previous approaches.

The measurement method relies on an extension of phase resonance testing to nonlinear structures. It is proposed to automate the realization of an appropriated excitation force by a Phase-Locked-Loop controller. Thereby, the conventionally used combination of manual force appropriation and free-decay analysis can be replaced, leading to a more robust, accurate and efficient experimental approach. Furthermore, the issue of experimental mode isolation quality is assessed based on power characteristics of the excitation force, providing a novel theoretical perspective on nonlinear experimental modal analysis.

The use of experimentally extracted nonlinear modes for the derivation of predictive models of nonlinear structures is discussed and different identification methods are presented. The functionality of the proposed methods and the significance of experimentally extracted nonlinear modal parameters is demonstrated in several laboratory experiments. The focus is put on systems with local conservative and smooth nonlinearities, but the extendability to nonsmooth and nonconservative systems is also demonstrated.

Kurzfassung

In der vorliegenden Arbeit wird eine neue Methodik zur nichtlinearen experimentellen Modalanalyse und deren Anwendung auf die Identifikation nichtlinearer dynamischer Strukturen vorgestellt. Die Methodik basiert auf der Theorie nichtlinearer Moden, welche eine solide theoretische Grundlage mit intuitiven Konzepten, wie nichtlinearen Eigenfrequenzen und Modenformen, vereint. Die Arbeit behandelt den gesamten Systemidentifikationsprozess, welcher die numerische Analyse, die Messung, die Identifikation sowie die Validierung und Verifikation prädiktiver Modelle beinhaltet. Besonderes Augenmerk liegt dabei auf der Entwicklung einer robusten und effizienten Methode zur experimentellen Extraktion nichtlinearer modaler Parameter, die zu den Hauptproblemen vorheriger Ansätze gehörte.

Die Messmethode besteht aus einer Erweiterung der Phasenresonanzmethode auf nichtlineare Strukturen. Es wird vorgeschlagen, die Anpassung der Anregungskraft mithilfe einer Phasenregelschleife zu automatisieren. Dadurch kann die bisher verwendete Kombination aus manueller Anpassung der Anregungskraft und Analyse des Abklingverhaltens ersetzt werden. Dies ermöglicht eine robustere, genauere und effizientere experimentelle Vorgehensweise. Zudem wird die Frage der Beurteilung der Qualität der Modenisolation anhand von Leistungsgrößen der Anregungskraft beleuchtet, was eine neue theoretische Sichtweise auf die nichtlineare experimentelle Modalanalyse darstellt.

Die Verwendung experimentell bestimmter nichtlinearer Moden zur Ableitung prädiktiver Modelle nichtlinearer Strukturen wird diskutiert und verschiedene Identifikationsmethoden werden aufgezeigt. Die Funktionalität der vorgeschlagenen Methoden und die Aussagekraft experimentell bestimmter nichtlinearer Moden werden anhand verschiedener Laborexperimente veranschaulicht. Der Fokus liegt dabei auf Systemen mit lokalen glatten und konservativen Nichtlinearitäten, jedoch wird auch die Erweiterbarkeit auf nichtglatte und nichtkonservative Systeme demonstriert.

Acknowledgments

No one can whistle a symphony. It takes a whole orchestra to play it.

H. E. Luccock

First of all, I would like to thank Professor Remco Leine for his constant support. Without his faith and openness to new ideas this thesis would not have been possible. His critical comments and our open-minded discussions have always been a great source of motivation for me. I also thank Professor Malte Krack for the collaboration, fruitful discussions and for accepting his role in the examination board. Furthermore, I would like to thank Professor Arnold Kistner for his support in my first years at the institute.

Special thanks goes to Pascal Reuß who encouraged me to join the institute and helped to find this interesting topic. I benefited a lot from his expertise.

Moreover, I thank Maren Scheel and Frédéric Schreyer for their interesting comments and discussions in our collaborative projects. I am particularly grateful to Maren for carefully proofreading my entire thesis.

I would like to acknowledge my colleagues and students for being part of my journey through academia and creating a unique working atmosphere. In particular, I thank Johann Groß, Daniel Steinepreis, Simon Walker, Timo Theurich and Benjamin Seeger.

A journey is best measured in friends, rather than miles.

T. Cahill

I am especially grateful to my parents Dory-Anne and Klaus for their unconditional support and for always encouraging me. Furthermore, I would like to thank my grandmother Gaby for her genuine interest in my work. Last but not least, I thank my wife Julia for her patience, her support and her love that has been invaluable for me in difficult times.

Contents

List of Frequently Used Symbols

Matrices

$\mathbf{B}$	signed Boolean matrix
$\mathbf{D}$	damping matrix
$\mathbf{H}$	dynamic stiffness matrix
$\mathbf{I}_N$	identity matrix of dimension $N \times N$
$\mathbf{J}$	Jacobian matrix
$\mathbf{K}$	stiffness matrix
$\mathbf{M}$	mass matrix
$\mathbf{\Phi}$	mass normalized linear eigenvector matrix
$\mathbf{\Omega}_0$	modal stiffness matrix

Vectors

$\boldsymbol{f}_{\mathrm{ex}}$	excitation force
$\boldsymbol{f}_{\mathrm{exm}}$	excitation force in linear modal coordinates
$\boldsymbol{f}_{\mathrm{nl}}$	nonlinear force
$\boldsymbol{f}_{\mathrm{nlm}}$	nonlinear force in linear modal coordinates
$\boldsymbol{g}_{\mathrm{nl}}$	nonlinear force in local coordinates
$\boldsymbol{q}$	vector of linear modal coordinates
$\boldsymbol{u}$	(relative) local coordinates in the interface
$\boldsymbol{w}$	generalized force direction
$\boldsymbol{x}$	vector of generalized coordinates
$\boldsymbol{x}_{\mathrm{em}}$	vector describing enforced nonlinear modal motion
$\boldsymbol{x}_{\mathrm{nm}}$	vector describing nonlinear modal motion
$\boldsymbol{\alpha}_{\mathrm{ln}}$	vector of linear model parameters
$\boldsymbol{\Gamma}$	vector of ansatz functions
$\boldsymbol{\kappa}$	vector of nonlinear model parameters
$\boldsymbol{\nu}$	vector of modal participation factors
$\boldsymbol{\phi}$	mass normalized eigenvector

$\boldsymbol{\psi}$ eigenvector

Scalars

D	distortion power
e	Euler's number
E_kin	mean kinetic energy
F	effective value of force
i	imaginary unit
p	instantaneous mechanical power
P	active power
Q	reactive power
S	apparent power
t	time
V	effective value of velocity
x_ex	displacement of the excitation point
α_1	stiffness proportional Rayleigh damping coefficient
α_2	mass proportional Rayleigh damping coefficient
β	cubic spring constant
Δ	Modal Purity Index
λ	local force at an excitation point
Λ	Power Based Mode Indicator Function
ξ	self-excitation parameter
Ξ	objective function for model updating
φ	phase difference between force and velocity
χ	local velocity at an excitation point
ω	(circular) frequency
ω_0	eigenfrequency
Ω	circular excitation frequency

Labels and Operators

$(\underset{\raise1pt\hbox{.}}{\cdot})$	complex Fourier coefficient
$(\tilde{\cdot})$	nonlinear modal quantity
$(\underset{\raise1pt\hbox{.}}{\cdot})$	complex conjugate Fourier coefficient
$(\cdot)^\mathrm{T}$	transpose

$(\cdot)^{\mathrm{H}}$	hermitian
$\mathrm{Re}\{(\cdot)\}$	real part
$\mathrm{Im}\{(\cdot)\}$	imaginary part
$\lvert(\cdot)\rvert$	absolute value
$\mathrm{diag}\{(\cdot)\}$	diagonal matrix
$\mathrm{sign}\{(\cdot)\}$	signum function
$\otimes$	Kronecker product
$\mathrm{FFT}\{(\cdot)\}$	Fast Fourier Transform

Indices

$i \cdots N$	index of degree of freedom
N_i	number of extracted linear modes
$j \cdots N_j$	index of excitation point
$n \cdots N_h$	harmonic index
$m \cdots N_m$	index of data point on the backbone curve
r	index of nonlinear mode

Abbreviations

CB	Craig-Bampton
CMS	Component Mode Synthesis
DOF	degree of freedom
EMA	(linear) Experimental Modal Analysis
ENM	enforced nonlinear mode
FE	finite element
FFT	Fast Fourier Transform
FRF	Frequency Response Function
HBM	Harmonic Balance Method
MPI	Modal Purity Index
MSHBM	Mixed Shooting Harmonic Balance Method
NEMA	Nonlinear Experimental Modal Analysis
NNM	nonlinear normal mode
NSID	Nonlinear Subspace Identification
ODE	ordinary differential equation
PBMIF	Power Based Mode Indicator Function

PDE	partial differential equation
PI	Proportional-Integral
PLL	Phase-Locked-Loop
RFSM	Restoring Force Surface Method
TFA	time-frequency analysis
VCO	Voltage Controlled Oscillator
WT	Wavelet Transform

Chapter 1

Introduction

The growing complexity of engineering structures together with an increasing demand for light-weight and cost-efficient designs poses new challenges in structural dynamics. Large deflections in slender structures, the use of composite materials, or contact interfaces in jointed structures lead to vibration behavior that cannot be predicted by linear models. Therefore, the identification of nonlinear structural models has recently become an eminent research topic in structural dynamics. For the identification of linear structures, experimental modal analysis (EMA) is a standard procedure. The individualistic nature of nonlinear structures, however, complicates the development of such a standard identification approach in nonlinear structural dynamics. Nonlinear modes are regarded as one promising concept in this context, yet, nonlinear experimental modal analysis (NEMA) is still in its infancy and the few existing approaches are associated with numerous practical difficulties and conceptual limitations. This thesis addresses these issues and contributes to the development of a more versatile NEMA method.

In this chapter, the motivation for the identification of nonlinear mechanical systems is explained in Section 1.1. The process of nonlinear system identification is introduced in Section 1.2 and nonmodal and modal approaches for system identification are briefly reviewed in Section 1.3. In Section 1.4, it is explained why a modal approach is particularly suitable for the identification of nonlinear vibrating structures and the objective of this work is defined. The chapter closes, in Section 1.5, with the outline of the thesis.

1.1 Motivation for Nonlinear System Identification

In many technical systems, structural vibrations are of major concern with regard to failure, wear or discomfort. Therefore, the investigation of the vi-

bration behavior is an important task in the design of mechanical systems. Even though the importance of numerical investigations has increased in recent years, the demand for experimental investigation is consistently high. For mechanical structures that can accurately be described by linear models the identification and validation of models is rather mature. The EMA, which has been developed since the 1960s, is nowadays considered a standard tool for the practicing engineer.

However, the examples mentioned in the introductory part of this chapter lead to models in which the generalized forces may depend in a nonlinear way on the generalized displacements or velocities. Such nonlinear dependencies can significantly influence the dynamic behavior of the structures. Characteristic features of nonlinear systems, such as resonance frequencies, may depend on the vibration level. Moreover, frequencies which are not present in the excitation spectrum may be important in the response spectrum. Coexisting attractors may occur, leading to different steady-state vibrations dependent on the initial condition. Furthermore, nonlinearity can lead to self-excited vibrations and quasi-periodic or chaotic response to periodic excitation. All of these effects are missed out by the restriction to linear models, resulting at best in a suboptimal design.

It is desired to include nonlinear effects in the design phase to achieve a save design and to exploit the potential of nonlinearity as a design space. Such a proactive approach inherently requires accurate numerical models including nonlinear effects leading to the problem of nonlinear system identification, which is still a very active field of research. The main issue complicating nonlinear system identification is the highly individualistic nature of nonlinear structures. For instance, distributed geometric nonlinearities due to large deformation are of a totally different nature than local nonsmooth nonlinearities such as friction in joints and may cause different dynamic effects. The various forms of nonlinearity require each a different treatment in the identification process. For this reason, the methodology in nonlinear system identification is fundamentally different to linear system identification in which most problems are treated with the same or very similar approaches.

1.2 A General Methodology for Nonlinear System Identification

This section discusses the general structure of a nonlinear system identification process, giving the reader a means to orient himself throughout the discussion of system identification methods in this thesis. The focus is put on the identification of nonlinear effects in mechanical dynamic systems, although it is noted at this point that nonlinear system identification in structural dynamics is greatly influenced by adjacent engineering fields such as control and electrical engineering. The process for the identification of such systems is shown in Fig. 1.1 and includes a classification of typical errors that are encountered in a system identification process. Moreover, typical actions to minimize the error are classified into the categories of model upgrading and updating.

The aim of system identification is to derive a mathematical model of a structure that is capable of predicting its dynamic behavior. This mathematical model is generally an approximation of reality and an optimal mathematical model should capture all effects that are deemed relevant within the operating range of interest with a minimal complexity of the model. Therefore, the identification process typically includes a combination of the theoretical and numerical analysis of trial models and the experimental analysis of the dynamic behavior of the structure under investigation. Modeling approaches that are based on first principles and exclusively rely on theoretical analysis are termed *white-box* modeling approaches, whereas modeling approaches that exclusively rely on experimental data are called *black-box* modeling approaches (Isermann and Münchhof, 2010). Both approaches are rarely used in reality. Pure white-box modeling requires exact a priori knowledge of all physical effects that are relevant for the model, which is infeasible in real life structures. Pure black-box approaches, however, lead to unnecessary identification cost as some a priori knowledge of the physics involved in a dynamic structure is at hand in most practical cases. Therefore, most identification approaches rely on *gray-box* modeling of some shade.

To evaluate the *validity* of a model, a set of measurement data is compared against the model predictions. If the model is capable of correctly capturing this experimental data or training data, then the model is regarded as a *validated numerical model*. In most cases, a first trial model is used that provides erroneous predictions of experimental reality. The
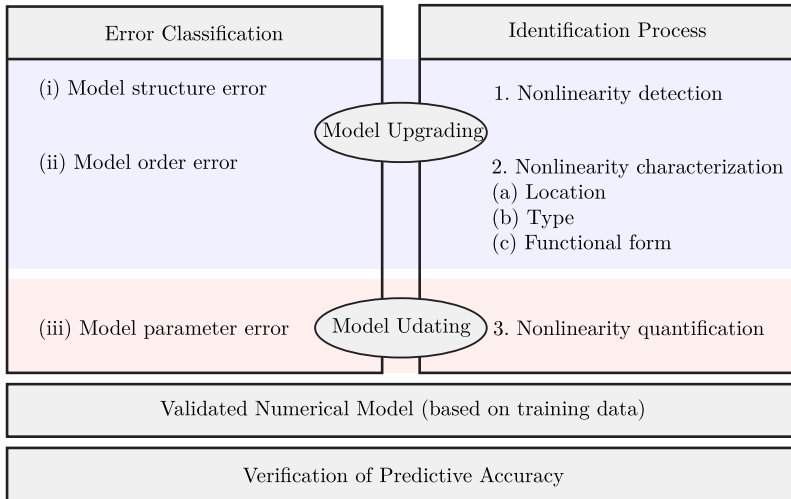
Figure 1.1: General structure of a nonlinear system identification process.

model error can, according to Mottershead and Friswell (1993), be traced down to three different error sources: errors based on (i) the model structure, (ii) the model order and (iii) the model parameters. The *model structure error* signifies that the model does not include all relevant features. A typical example of a model structure error is the use of a linear model for a system that actually shows nonlinear behavior. The *model order error* stems from the fact that models of mechanical structures are in most cases discrete representations of continuous structures. This class of errors includes errors that may occur due to an inappropriate spatial or temporal discretization of the model. Examples include a too coarse discretization of a finite element (FE) model or an inadequate number of harmonics in harmonic balance simulations. The *model parameter errors* are caused by wrongly estimated model parameters, such as a wrongly estimated Young's modulus or nonlinear spring coefficients.

The nonlinear system identification procedure is, following Kerschen et al. (2006), divided into the three steps: nonlinearity detection, nonlinearity characterization and nonlinearity quantification. As a result of the *nonlinearity detection* step the need for a nonlinear model is deter-

mined. Although there are specific methods for nonlinearity detection, in most cases the detection is naturally included in a linear identification procedure such as an EMA. The inspection of the measured frequency responses or ambiguities in the pole calculation can often be the first evidence of non-negligible nonlinear behavior. The *nonlinearity characterization* in terms of the location, the type of nonlinearity and its functional form is an important step in nonlinear system identification and marks a significant difference to linear system identification, in which the structure of the model is inherently determined by assuming linearity. The last step of the identification is the *nonlinearity quantification*. Thereby, the coefficients of the nonlinear functions are determined.

It is emphasized that the process for nonlinear system identification is closely related to the type of model error that is sought to be minimized. While the detection and characterization are mainly a way of improving the model structure by additional features, e.g., nonlinear elements, or, less common, choosing the model order based on experimental observations, the quantification step is solely concerned with adjusting the model parameters and thereby reducing the model parameter error. An interesting distinction of the actions made to improve a model that has been proposed by Ewins et al. (2015) is the distinction between model upgrading and updating. *Model upgrading* is the extension of a model by adding new features that essentially change the model structure. In nonlinear identification, this step is based on the detection and characterization steps and aims at reducing the model structure and model order error. In contrast *model updating* is a method for reducing the model parameter error based on the nonlinearity quantification.

Generally, all nonlinear system identification methods can be structured based on the procedure proposed in Fig. 1.1. It should be noted, however, that the class of black-box identification methods and the class of model updating methods, which recently attract increasing attention in structural dynamics (Noël and Kerschen, 2016), represent extreme cases in which the individual steps of the process become indistinct or are omitted. Black-box methods aim at performing all three steps of the identification process at once, without any knowledge of the involved physics. Mostly, however, even for such approaches some a priori knowledge of the model structure significantly improves the performance and accuracy of the identification leading to a (dark) gray-box strategy, which is embedded in the process shown in Fig. 1.1. In contrast, model updating strategies require an a priori estimate of the model, e.g., based on first principle white-box

modeling. Depending on the quality of the white-box model one or more of the identification steps become obsolete. Typically, such white-box model updating focuses on the quantification of nonlinearity, leading to a (light) gray-box strategy.

The last step of the identification procedure shown in Fig. 1.1 is the *verification* of the obtained model. The goal of this step is to evaluate the predictive accuracy of a model for situations that are not included in the training data for which it is validated. Of course, a predictive model for a wide range of operating conditions is the ultimate goal of system identification. However, it is emphasized that particularly for nonlinear systems special care must be taken if predictions are made for operating ranges which have not been included in the range spanned by the training data.

1.3 Literature Survey

This section gives an overview of the most important developments in the identification of nonlinear dynamic structures. Detailed reviews of identification methods can be found in the book of Worden and Tomlinson (2001) and the review articles of Kerschen et al. (2006) and Noël and Kerschen (2016). Most conventional nonlinear identification methods operate in physical coordinates, i.e., are nonmodal based, and the following survey, therefore, starts with a brief overview of nonmodal methods. However, this thesis focuses on a modal approach towards nonlinear system identification. Therefore, the developments in this particular class of methods is described seperately in a more comprehensive way in Section 1.3.2.

1.3.1 Nonmodal Nonlinear System Identification

In the following overview, the identification methods are categorized into methods operating in time domain, in frequency domain and in time-frequency domain.

One widespread *time domain* methods is the Restoring Force Surface Method (RFSM)[1], which was originally proposed by Masri and Caughey (1979) for single degree of freedom (DOF) systems with stiffness nonlinearities. The fundamental idea of the RFSM is that, for single DOF systems

---

[1]The RFSM is also known as force-state mapping, which goes back to the work of Crawley and O'Donnell (1986).

with a known mass and measured acceleration, the restoring forces can be directly estimated by the balance of linear momentum. The restoring force is then plotted over the phase space and a surface is fitted to obtain the coefficients of the displacement and velocity dependent restoring forces. The generalization to multi DOF systems was addressed by Masri et al. (1982) and Al-Hadid and Wright (1989). Simple continuous structures were identified by Al-Hadid and Wright (1990) and Kerschen et al. (2001). Systems with damping nonlinearities can be treated with a related approach as shown by Gaul and Lenz (1997) for bolted joints with friction nonlinearity. However, for systems with a larger number of DOFs, the nonlinearity quantification remains difficult and time consuming (Worden and Tomlinson, 2001). Therefore, in most recent works the RFSM is solely used for the characterization step[2], for which it is regarded as one of the simplest and most powerful approaches (Kerschen et al., 2006). A similar time domain approach which can be used for multi DOF systems of limited complexity is the direct parameter estimation method proposed by Mohammad et al. (1992). This method uses a chain of lumped masses which are connected by unknown force elements. Similarly to the RFSM the relative acceleration between the lumped masses is measured to obtain an estimate of the relative restoring forces and a least squares fit is used to obtain an appropriate force law. A black-box time domain approach originating from control engineering is the Nonlinear Auto-Regressive Moving Average with Exogenous inputs (NARMAX) method, which is based on a discrete-time form of the dynamic system (Leontaritis and Billings, 1985a,b). In structural dynamics the method was, for instance, adopted by Thouverez and Jezequel (1996) in modal coordinates or more recently by Worden and Barthorpe (2012) and Worden et al. (2012) for simple hysteretic systems. A method that recently attracted increasing attention in structural dynamics is Nonlinear Subspace Identification (NSID), which can be implemented either in the time domain or frequency domain. The time domain version was suggested by Marchesiello and Garibaldi (2008).

Many of the popular *frequency domain* methods for nonlinear system identification are based on a generalization of the concept of Frequency Response Functions (FRFs) to nonlinear systems. While the definition of FRFs is clear for linear systems, the notion is ambiguous in the nonlinear case, resulting in several different identification methods that claim to be

---

[2]This version of the RFSM is sometimes referred to as Acceleration Surface Method, e.g., in Cooper et al. (2017).

based on nonlinear FRFs. Probably the most straightforward approach of extending FRFs to nonlinear systems is to relate a specific, usually harmonic, excitation to the response of the system at a certain frequency. This approach is typically used for the purpose of model validation, mostly in conjunction with the numerical calculation of FRFs using the Harmonic Balance Method (HBM) (see, e.g., Bograd et al. (2011); Schwingshackl et al. (2012)). If the approach is used for identification purposes, then an a priori model of the structure and nonlinearity has to be known and the focus is put on the nonlinearity quantification step. For instance, Meyer and Link (2003) propose to use a direct model updating procedure based on measured FRF data and HBM simulations for the purpose of parameter identification. A more sophisticated generalization of FRFs is provided by the concept of higher order FRFs based on Volterra or Wiener series (Storer, 1991). Due to the high computational and experimental effort, applications of these concepts are relatively scarce and limited to examples of moderate complexity (Khan and Vyas, 2001; Tawfiq and Vinh, 2004). Further spectral methods for identification that are based on the separation of the FRF of the underlying linear system and the distortions caused by a nonlinear force, are the conditional reverse path method (Richards and Singh, 1998) and the nonlinear identification through feedback of the output method (Adams and Allemang, 2000). Both methods have in common that they mainly focus on the quantification step and can be performed with random excitation signals. A central idea of the nonlinear identification through feedback of the output method is that the nonlinear forces are regarded as internal feedback forces. This concept also forms the foundation for the more recent NSID techniques. A frequency domain version of NSID was proposed by Noël and Kerschen (2013) and compared to the time domain NSID approach in Noël et al. (2014).

The class of *time-frequency* methods for nonlinear system identification aims at extracting the instantaneous frequency of vibration, which may be a function of time in nonlinear systems. In addition to the instantaneous frequency, a time-frequency analysis (TFA) typically yields the envelope of the time signal. Therefore, time-frequency methods are commonly used for extracting damping characteristics of nonlinear systems by analyzing decay processes of the free system. The most basic approach for time-frequency analysis is the Short-Time Fourier Transform. More advanced methods for TFA are the Hilbert Transform (Feldman, 1994) and the Wavelet Transform (WT) (Staszewski, 2000). The extraction of the instantaneous frequency is often used for free-decay processes starting at resonance yielding

an approximation of the systems backbone curve, which can be regarded as a means of extracting the nonlinear modal characteristics of the system. This application of TFA is described in more detail in the following section.

1.3.2 Modal Nonlinear System Identification

Since a modal approach for system identification is common practice for linear systems, it seems to be an obvious question to which extent modal methods can be extended to nonlinear systems. Against this backdrop, it is quite remarkable that the use of modal methods for nonlinear system identification is a rather recent, yet active, field of research (Noël and Kerschen, 2016). Probably, the backlog in research in this area can be attributed to the fact that the standard linear EMA is conceptually built upon the superposition principle, which immediately fails for nonlinear systems. Therefore, a rigorous NEMA requires a fundamentally different conceptual basis.

There are a few methods that provide reasonable approximations for the case of weak nonlinearitiy which are based on concepts known from linear EMA. A simple method to include a nonlinear analysis in the process of an EMA using the phase separation method performed with stepped-sine measurements, is the amplitude dependent linearization proposed by Carrella and Ewins (2011). Force appropriation based EMA methods, which are mostly used in ground vibration testing of aircraft, open the door to the identification of amplitude dependent modal parameters and the characterization of modal coupling as demonstrated by Atkins et al. (2000). This idea has been augmented by Platten et al. (2009) using an analysis of the free-decay from an appropriated mode or set of modes, which is referred to as nonlinear resonant decay method. It should be noted that these methods, which have successfully been applied to rather complex structures, such as a full scale aircraft (Fuellekrug and Goege, 2012), are based on a linear modal framework combined with a modal RFSM and are particularly attractive for large scale structures with weak local nonlinearities.

A milestone in the development of NEMA was the work of Peeters et al. (2011), who related concepts of force appropriation to the theory of nonlinear (normal) modes[3]. The method combines an approximate appropriation of the nonlinear mode with a TFA using the WT of the free-decay from

---

[3]The word normal is omitted in the following for reasons which will be detailed in Section 2.1.

resonance. The experimental applicability was demonstrated at a bench-mark beam structure in Peeters et al. (2010). Subsequently, this method for NEMA in the framework of nonlinear modes has successfully been applied to several structures of moderate complexity (Ehrhardt and Allen, 2016; Londono et al., 2015; Zapico-Valle et al., 2013). Recently, Renson et al. (2016) has proposed a method for a more robust force appropriation procedure with which the free-decay analysis can be omitted. A different approach to identify nonlinear modes is pursued by Noël et al. (2016), who propose the use of a NSID technique in combination with a shooting method for the extraction of nonlinear modal characteristics under broad band excitation.

Another concept for modal identification of nonlinear systems is based on a direct decomposition of experimental data into so-called intrinsic modal oscillators. This method, which is based on a TFA of the recorded time series using the Hilbert transform, is referred to as empirical mode decomposition (Huang et al., 1998). The extracted modal oscillators are generally neither the linear nor the nonlinear modes of the system, however, they have successfully been used, e.g., to characterize the process of targeted energy transfer (Lee et al., 2010) and to identify a beam featuring a bolted connection (Eriten et al., 2013). A related modal approach is the method of proper orthogonal decomposition, which is based on a statistical analysis of the systems response. Applications of this method in structural dynamics are reviewed in Kerschen et al. (2005). Similarly to the empirical mode decomposition, a clear physical interpretation of proper orthogonal modes remains difficult, particularly for nonlinear systems, but they have been used for the identification of nonlinear systems, for instance, using a model updating strategy (Lenaerts et al., 2001) or a machine learning framework (Worden and Green, 2017).

1.4 Objective and Scope of the Thesis

In this section, the purpose and scope of this thesis are elucidated. The section starts with an explanation why a modal approach towards nonlinear system identification is found to be a necessary addition to the nonlinear system identification toolbox. In the following, the shortcomings of current modal approaches are summarized and the goals and scope of the present thesis are derived.

Advantages of a Modal Approach

Based on the fact that EMA is by far the most popular concept for the identification of vibrating structures, it seems to be the most intuitive approach for nonlinear system identification to extend the concept of modes to nonlinear systems. In this context, the theory of nonlinear modes provides a solid theoretical foundation with a clear connection to linear modes. In particular, a nonlinear system identification approach based on nonlinear modes offers the following advantages:

- Nonlinear modes provide a clear physical meaning and the use of modal characteristics, i.e., modal frequencies, deflection shapes and damping measures, is an intuitive concept for most practicing engineers, even though they may become energy dependent in the nonlinear case.

- Similarly to linear modes, nonlinear modes typically determine the resonant behavior of structures, which is often the most relevant operating condition in the design of vibrating structures. A model identified based on nonlinear modes provides high confidence in such operating conditions.

- Nonlinear modal characteristics are system properties and, thus, independent of a specific forcing scenario or load case.

- The theory of nonlinear modes is well-developed and provides a valuable tool for understanding nonlinear dynamics. This solid foundation is helpful for the interpretation of the observed experimental dynamics and the derived nonlinear modal characteristics.

Shortcomings of Nonlinear Experimental Modal Analysis

The application of nonlinear modes for the purpose of system identification is still in its infancy and so far mostly academic structures of low complexity have been successfully identified. The reasons for this are primary seen in the following shortcomings of current NEMA approaches:

- The current experimental procedures, which are almost exclusively based on the method proposed by Peeters et al. (2010), are very time consuming and lack robustness.

- The identification of predictive models based on experimental non-linear modes has rarely been discussed in literature. The significance of experimentally extracted nonlinear modal parameters for this purpose has not sufficiently been demonstrated.

- The efficiency of numerical algorithms for the calculation of nonlinear modes has not fully been exploited for the purpose of system identification.

- It is not clear whether current methods for NEMA can be generalized to nonsmooth and nonlinearly damped systems and how this could be accomplished.

Aim and Scope of the Thesis

The goal of this monograph is to develop a strategy for the nonlinear system identification in the framework of nonlinear modes. The proposed strategy shall pave the way towards nonlinear modal identification of more complex real life structures. To this end, in particular, the following issues are addressed:

- A reliable experimental strategy for the measurement and extraction of nonlinear modal characteristics is proposed.

- An efficient numerical algorithm for the calculation of nonlinear modes is derived, which is used to complement the experimental data with numerical analysis.

- The experimental and numerical analysis are embedded in different system identification strategies, providing a framework for the derivation of predictive models based on nonlinear modal data.

- The use of NEMA for nonlinear system identification is illustrated with several experimental application examples. The validation and verification of derived models is thoroughly discussed to shed light on the significance of experimentally extracted nonlinear modal parameters.

The main focus of this thesis is put on the identification of structures with smooth local stiffness nonlinearities. However, it is also demonstrated that the methods can be generalized to systems with *nonsmooth nonlinearities*,

such as unilateral constrained systems undergoing impacts, and systems subjected to *nonlinear damping*, e.g., due to frictional joints. The generalization to spatially distributed nonlinearities is possible, but considered beyond the scope of this thesis. Moreover, the quantitative measurement of internally resonant structures is an open research question that is considered beyond the scope of the thesis, although the methods proposed here are likely to be extendable for this purpose.

1.5 Outline of the Thesis

In the first part of the thesis, modal based nonlinear system identification methods have been set into the context of a more general identification methodology. The current state of knowledge has been briefly introduced and the need for research in this area has been identified.

In Chapter 2, the fundamental and more recent definitions of nonlinear modes are reviewed. The definition used in this thesis is introduced and important terminology in the field of nonlinear modes is clarified.

Chapter 3 is concerned with the numerical simulation of nonlinear modes. Numerical simulations, which can be used for model validation or nonlinearity quantification, are an important addition to purely experimental based identification methods, particularly, when complex nonlinear structures are investigated. Therefore, special emphasis is put on the suitability of the numerical algorithm for the purpose of system identification with regard to efficiency and robustness. The potential of the numerical algorithm to treat complex real life structures is demonstrated using the numerical example of an industrial scale model of a commercial vehicle.

The experimental extraction of nonlinear modes is addressed in Chapter 4. Due to the numerous deficiencies of current approaches, a completely new framework for NEMA is proposed. In particular, the practical realization of nonlinear mode appropriation, the estimation of the quality of the mode isolation and the extraction of nonlinear modal parameters are discussed. The method is demonstrated using a numerical example and the extension to structures subjected to nonsmooth and damping nonlinearities is addressed.

In Chapter 5, the numerical and experimental developments of the previous chapters are put into the context of system identification procedures. More specifically, three different identification strategies are proposed: a gray-box strategy in nonlinear modal domain, an analytical-experimental

approach in mixed-modal-physical coordinates and a white-box model up-
dating strategy in physical coordinates. The first approach is purely based
on experimental data, whereas the second approach combines experimental
data with analytical estimation of the nonlinear forces based on the HBM.
The third method integrates the numerical algorithm for nonlinear mode
calculation and the experimental data in a model updating procedure.

The derived methods are applied to three different test cases in Chap-
ter 6. In the first test case, the identification strategies are investigated
using a benchmark beam structure featuring a local stiffness nonlinearity.
The second test case illustrates the applicability of the proposed method
in the case of nonsmooth nonlinearities by studying the capability of non-
linear modal based model validation for an impacting beam. The third
test case examines the capability of treating nonlinearly damped struc-
tures by a purely experimental based identification strategy applied to a
simple benchmark structure showing nonlinear behavior due to a bolted
joint connection.

In Chapter 7, the main contributions of this thesis are summarized and
conclusions are drawn. Finally, open questions are highlighted and direc-
tions of future research are indicated.

Chapter 2

Nonlinear Modes

In this thesis, a modal approach towards the identification of nonlinear systems is pursued. In contrast to linear systems, where the definition of a mode is more or less consensus, there are several different definitions of modes in nonlinear systems. Thus, this chapter briefly introduces the most important definitions, clarifies the approach pursued in this study and discusses some important terminology.

The chapter starts with the introduction of the fundamental definitions of nonlinear modes in Section 2.1. In Section 2.2, recent developments regarding the definition of nonlinear modes are briefly addressed. In Section 2.3, important terminology used in nonlinear modal analysis is clarified.

2.1 Fundamental Definitions of Nonlinear Modes

There are two fundamentally different definitions of nonlinear modes, on which other definitions are based on. The first definition, which is attributed to Rosenberg (1960), can be regarded as a straightforward extension of the concept on linear normal modes and is exclusively valid for conservative mechanical systems. The details of this definition and a generalization used in this thesis are presented in the first part of this section. The second basic definition by Shaw and Pierre (1991) views nonlinear modes as an invariant manifold in phase space and is also valid for nonconservative nonlinear systems. This definition is introduced in the second part of this section.

2.1.1 Nonlinear Modes of Conservative Systems

Periodic solutions of autonomous nonlinear systems have been studied for more than a century (Ljapunov, 1992; Poincaré, 1892), but the notion of nonlinear modes emerges in the work of Rosenberg (1960). Rosenberg

highlighted the analogy of linear normal modes and periodic solutions of nonlinear autonomous systems to define a *nonlinear normal mode* (NNM). However, it is interesting to note that the book of Kauderer (1958) already contains a major part of the derivations and similar terminology (in German language) as the work of Rosenberg. A NNM according to Rosenberg is a synchronous periodic vibration of a nonlinear conservative system with symmetric potential. In the displacement space, which is sometimes referred to as configuration space in later publications, this motion forms a line[1] which intersects lines of constant potential orthogonally. The notion of a synchronous periodic motion implies that all points of a structure vibrating in a NNM reach their maximum displacements simultaneously, as in the case of linear normal modes. Rosenberg's definition subsequently served as a basis of hundreds of publications which are summarized in a book of Vakakis et al. (1996) and several review articles by Vakakis (1997), Kerschen et al. (2009), Mikhlin and Avramov (2010) and Avramov and Mikhlin (2013). It can be observed that the initial definition of Rosenberg evolved over the years. In particular, the requirements for a symmetric potential and a synchronous motion have been relaxed to include more generic nonlinearities and the effect of *internal resonances*. Internal resonances are caused by nonlinear interactions of different nonlinear modes, typically when their frequencies are (nearly) commensurable (Nayfeh, 2000).

In this thesis, an extended version of Rosenberg's definition, including generic conservative nonlinearities and internal resonances, serves as a foundation[2].

Definition 2.1. Consider an autonomous, conservative, nonlinear system in a discrete form

$$\mathbf{M}\ddot{\boldsymbol{x}}(t) + \mathbf{K}\boldsymbol{x}(t) + \boldsymbol{f}_{\mathrm{nl}}(\boldsymbol{x}(t)) = \mathbf{0}, \tag{2.1}$$

where $\mathbf{M} = \mathbf{M}^{\mathrm{T}} \in \mathbb{R}^{N \times N}$ denotes the positive definite mass matrix, $\mathbf{K} = \mathbf{K}^{\mathrm{T}} \in \mathbb{R}^{N \times N}$ the positive definite linear stiffness matrix, $\boldsymbol{x}(t) \in \mathbb{R}^{N}$ represents the vector of generalized coordinates and $\boldsymbol{f}_{\mathrm{nl}}(\boldsymbol{x}(t)) \in \mathbb{R}^{N}$ represents the vector of nonlinear conservative forces. A <u>nonlinear modal motion</u> is a periodic solution $\boldsymbol{x}_{\mathrm{nm}}(t) = \boldsymbol{x}_{\mathrm{nm}}(t + \tilde{T}_0)$ of Eq. (2.1) with the nonlinear

---

[1]NNMs describing a straight line are referred to as similar NNMs, NNMs describing a curved line are referred to as nonsimilar NNMs.

[2]It is assumed for simplicity that continuous systems have been discretized, e.g., using the FE method.

modal frequency $\tilde{\omega}_0 = \frac{2\pi}{T_0}$. A <u>nonlinear mode</u> is a family of nonlinear modal motions, which are connected in a frequency-energy diagram.

The theory of nonlinear modes shall not be reviewed at length here, however, a few important characteristics of nonlinear modes are briefly recapitulated. The first important characteristic is that nonlinear modes do generally not, in contrast to linear normal modes, possess any simple orthogonality relations, which is also the reason why the author refrains from using the notion NNM. Another important difference to linear modes is that the principle of superposition does not hold for nonlinear modes. These two properties, however, are essential in most applications of linear modes such as EMA and model order reduction. Additional important differences with respect to linear modes are the energy dependence of the frequency and shape (for nonsimilar modes) and the occurrence of mode bifurcations. Finally, it is noted that the number of nonlinear modes may exceed the number of linear modes of a system.

Despite all differences, some important properties of linear modes also hold for nonlinear modes. First of all, nonlinear modes are invariant, i.e., a motion initiated on a nonlinear mode remains on the nonlinear mode for all times. Other than that, the resonant behavior of nonlinear systems is typically determined by its nonlinear modes. This feature is particularly appealing in the context of system identification, because a model identified based on nonlinear modes promises to accurately capture the technically relevant resonant behavior of a system.

2.1.2 Nonlinear Modes of Nonconservative Systems: The Invariant Manifold Approach

A major limitation of the previously mentioned definitions is that they are only valid for conservative systems. To overcome this limitation Shaw and Pierre (1991) proposed a new definition of nonlinear modes which is inspired by the center manifold theory:

Definition 2.2. Consider an autonomous, nonconservative, nonlinear system in a discrete form

$$\mathbf{M}\ddot{\boldsymbol{x}}(t) + \mathbf{D}\dot{\boldsymbol{x}}(t) + \mathbf{K}\boldsymbol{x}(t) + \boldsymbol{f}_{\mathrm{nl}}(\boldsymbol{x}(t), \dot{\boldsymbol{x}}(t)) = \mathbf{0}, \tag{2.2}$$

with $\mathbf{M} = \mathbf{M}^{\mathrm{T}} \in \mathbb{R}^{N \times N}$, $\mathbf{D} \in \mathbb{R}^{N \times N}$, $\mathbf{K} \in \mathbb{R}^{N \times N}$ and the generalized nonlinear forces $\boldsymbol{f}_{\mathrm{nl}}(\boldsymbol{x}(t), \dot{\boldsymbol{x}}(t)) \in \mathbb{R}^{N}$, which include conservative and

nonconservative forces. A nonlinear mode of a nonconservative system is a motion governed by Eq. (2.2) which takes place on a two dimensional invariant manifold in the phase space of the system. The invariant manifold has its origin in a stable equilibrium point $\boldsymbol{x}^* = \dot{\boldsymbol{x}}^* = \boldsymbol{0}$ and is tangent to the eigenspace of the system's linearization about $\boldsymbol{x}^*$, i.e., $\boldsymbol{f}_{\mathrm{nl}}(\boldsymbol{x}^*, \dot{\boldsymbol{x}}^*) = \boldsymbol{0}$. The motion on the invariant manifold can be fully described as a function of the set of master coordinates $x^{\mathrm{m}}, \dot{x}^{\mathrm{m}}$.

The description of the systems dynamics in terms of the master coordinates corresponds to constraining the motion to a two dimensional subspace in the phase space. Therefore, the dynamics of the constrained system can be interpreted as a single DOF oscillator on the invariant manifold. The dependence of the remaining coordinates on the master coordinates is calculated similarly to the center manifold reduction technique (Khalil, 1996) and is not reviewed here in detail. The fact that the nonlinear modal dynamics of potentially high dimensional systems is described by a single DOF oscillator on the invariant manifold motivates the primary application of the invariant manifold definition, namely, the use for model order reduction (Pierre et al., 2006). Finally, it is noted that the definition only includes nonlinear modes which are a continuation of linear modes and that the treatment of internal resonances requires a different parameterization yielding a multi DOF modal oscillator (Blanc et al., 2013).

2.2 Recent Definitions of Nonlinear Modes

Although nonlinear modes have been studied for more than half of a century and most of the work, particularly until the last decade, focused on theoretical and analytical developments, there are still recent attempts for novel definitions of nonlinear modes addressing deficiencies of the fundamental definitions. The work of Haller and Ponsioen (2016) aims at theoretical ambiguities of different approaches based on the invariant manifold theory. The notion of spectral submanifolds is used to propose a unified definition of invariant manifolds for autonomous, nonautonmous, conservative and nonconservative systems.

A completely different, application driven perspective motivates the definition of Laxalde and Thouverez (2009). According to their definition nonlinear modes are characterized by complex nonlinear eigenvalues and eigenvectors, representing the fast oscillatory behavior as well as the slow amplitude modulation due to damping (or self-excitation). The definition

is based on a straightforward extension of complex eigenvalues of linear systems with the main objective of efficient numerical calculation of the nonlinear modes of damped systems using a generalized Ritz-Galerkin approach. A salient feature of this method is that the nonlinear modes are by definition approximate solutions to the system's equation of motion. The definition of Laxalde and Thouverez (2009) is conceptually similar to the extended periodic motion definition, which is also used in this thesis and therefore described in some detail in the following.

2.2.1 The Extended Periodic Motion Concept for Nonconservative Systems

The limitation of Definition 2.1 to conservative systems and numerical difficulties related to Definition 2.2 motivates the following definition proposed by Krack (2015):

Definition 2.3. An <u>enforced periodic nonlinear mode</u> (ENM)[3] is a periodic solution $\boldsymbol{x}_{\mathrm{em}}(t) = \boldsymbol{x}_{\mathrm{em}}(t + \tilde{T}_{\mathrm{em}})$ of the equation

$$\mathbf{M}\ddot{\boldsymbol{x}}(t) + \mathbf{D}\dot{\boldsymbol{x}}(t) + \mathbf{K}\boldsymbol{x}(t) + \boldsymbol{f}_{\mathrm{nl}}(\boldsymbol{x}(t), \dot{\boldsymbol{x}}(t)) - \xi\mathbf{M}\dot{\boldsymbol{x}}(t) = \mathbf{0}. \qquad (2.3)$$

with $\mathbf{M} = \mathbf{M}^{\mathrm{T}} \in \mathbb{R}^{N \times N}$, $\mathbf{D} \in \mathbb{R}^{N \times N}$, $\mathbf{K} \in \mathbb{R}^{N \times N}$ and the generalized nonlinear forces $\boldsymbol{f}_{\mathrm{nl}}(\boldsymbol{x}(t), \dot{\boldsymbol{x}}(t)) \in \mathbb{R}^{N}$, which include conservative and nonconservative forces. The term $\xi\mathbf{M}\dot{\boldsymbol{x}}(t)$ represents an artificial mass proportional self-excitation. The parameter ξ is chosen such that the motion becomes periodic. If the system is conservative, the parameter $\xi = 0$, such that the definition reduces to Definition 2.1.

Similarly to the definition of Laxalde and Thouverez (2009), Definition 2.3 aims at exploiting numerically efficient methods for the calculation of damped nonlinear modes. The advantage of Definition 2.3 lies in the fact that the ENMs are by definition periodic, i.e., can be calculated with the mature numerical methods for calculation of periodic solutions of ordinary differential equations (ODEs). Another advantage pointed out by Krack (2015) is that the ENMs often provide a good approximation for steady-state vibrations of the forced system, which is of great practical relevance. Furthermore, it will be shown in this thesis that the extended

---

[3]In the work of Krack (2015) ENMs are simply referred to as nonlinear modes. In this thesis, the notion ENM is used to differentiate ENMs from nonlinear modes of conservative systems.

periodic motion concept can be easily adapted to experimental methods forming the basis of a novel method for NEMA of damped systems.

2.3 Auxiliary Terminology

This section contains a collection of important terminology related to non-linear modes to avoid ambiguities. The terminology supplements Definition 2.1 and shall provide orientation throughout the thesis. Because a system governed by Eq. (2.1) may generally posses infinitely many periodic solutions, a subset of nonlinear modes of great practical relevance is pointed out:

Definition 2.4. A <u>fundamental nonlinear mode</u> is a nonlinear mode according to Definition 2.1 which forms a continuation of the linear modes of the linearized system in a frequency-energy diagram.

A different graphical representation of nonlinear modes yields the following definition:

Definition 2.5. A <u>backbone curve</u> is a nonlinear mode plotted in the amplitude-frequency plane. Herein, the word <u>amplitude</u>, denotes the magnitude of the fundamental harmonic Fourier coefficient, i.e., at the nonlinear modal frequency $\tilde{\omega}_0$.

It is pointed out that, although the notion backbone curve is almost colloquially used in literature, there are two concurrent meanings: the backbone curve is defined (a) in the framework of nonlinear modes (c.f. Definition 2.5) or (b) as the curve connecting the maxima of FRFs for different excitation levels. Obviously, both curves are not the same, not even for linear systems. The fact that the curves are in many cases close to one another[4] often leads to the misinterpretation that the nonlinear modes, i.e., the backbone according to (a), generally also forms the backbone of the forced response, i.e., (b). It is emphasized, that Definition 2.5 is used throughout this thesis as this definition provides the advantage of having a profound theoretical basis and does not depend on the considered load case or damping hypothesis.
The last term which is introduced, is particularly important in the practical realization of numerical and experimental nonlinear modal analysis in the frequency domain.

---

[4]An example showing that this is not necessarily the case is included in Section 3.3.

Definition 2.6. A <u>monophase nonlinear modal motion</u> is a periodic motion $\boldsymbol{x}_{\mathrm{nm}}(t) = \boldsymbol{x}_{\mathrm{nm}}(t + \tilde{T}_0)$, of which the Fourier transform is monophase, i.e., can be represented by a pure sine or cosine series.

The limitation to monophase nonlinear modes reduces the computational effort in numerical modal analysis and is also of interest for the nonlinear mode isolation in experiments. Furthermore, the concept of monophase nonlinear modes is closely related to the Rosenberg's definition of synchronous nonlinear modes, which are inherently monophase, giving the term some historical significance[5].

---

[5]It is noted that the opposite does not hold, because internally resonant nonlinear modes can be monophase, but are not necessarily synchronous.

Chapter 3

Numerical Calculation of Nonlinear Modes

The process of system identification typically involves numerical and theoretical analysis (c.f. Chaper 1.2). Depending on the identification strategy, the efficiency of numerical calculations is of major concern. Therefore, this chapter proposes an efficient algorithm for the calculation of nonlinear modes. To this end, in Section 3.1, the state of knowledge for the numerical calculation of nonlinear modes is briefly recapitulated and requirements for the numerical algorithm are clarified. The calculation method is then introduced in Section 3.2. An industrial scale application example is used in Section 3.3 to demonstrate the numerical method. Subsequently, the extension of the method to nonconservative and nonsmooth systems is discussed in Sections 3.4 and 3.5. The developments made in this chapter are summarized in Section 3.6.

3.1 State of Knowledge

This section starts with a brief overview of existing numerical approaches for nonlinear modal analysis. The requirements for a numerical approach suitable for nonlinear system identification are outlined in the remainder of this section.

3.1.1 Numerical Methods for Nonlinear Modal Analysis

There are various approaches for the calculation of nonlinear modes, including analytical and numerical methods. The analytical methods, such as the method of multiple scales or averaging, are for instance described in the books of Vakakis et al. (1996) and Nayfeh (2000). These analytical techniques are typically restricted to systems of limited complexity, whereas recent numerical methods are capable of treating real life structures. The

numerical methods can be divided into methods for the calculation of (a) nonconservative modes based on the invariant manifold concept (c.f. Definition 2.2) and (b) the calculation of conservative modes, i.e., modes which are described by a periodic motion, (c.f. Definition 2.1).

The approaches based on (a) typically lead to the problem of solving a nonlinear partial differential equation (PDE), which describes the geometry of the invariant manifold. This PDE is generally difficult to solve in closed form such that approximate solution techniques are used. Besides the Taylor series expansion, which was used by Shaw and Pierre (1991), the numerical methods include several classical techniques for the solution of PDEs. For instance, Galerkin methods were applied by Pesheck et al. (2002) and Pierre et al. (2006) and a finite element formulation was proposed by Renson and Deli (2012). For the invariant manifold approaches often difficulties arise due to the parametrization of the manifold. The uniqueness of the parametrization is lost when folds in the invariant manifold occur, e.g., due to internal resonances (Blanc et al., 2013). Furthermore, the computational effort for the solution of the PDE is often considerable. These conceptual drawbacks might also be the reason why the invariant manifold concept has mostly been applied to rather academical examples so far. Moreover, the direct measurement of the invariant manifolds seems to be infeasible at present, such that invariant manifold based approaches are of limited use in the context of system identification.

In contrast to (a), the numerical methods for (b) lead to the problem of finding periodic solutions of an ODE. For the calculation of periodic solutions of ODEs there exist numerous methods. Of particular importance in this context are shooting methods and Harmonic Balance based approaches. Even though the shooting method is comparatively old, it has for the first time been applied to the computation of nonlinear modes quite recently by Peeters et al. (2009). It is noted that, in an earlier work by Slater (1996), a related method was used for the calculation nonlinear modes. Subsequently, the shooting algorithm has been widely used and proved its applicability even to complex numerical structures, such as an aircraft (Kerschen et al., 2013) or a satellite structure (Renson et al., 2012). Furthermore, the shooting method has been applied to a benchmark system for comparison with experimentally obtained nonlinear modes (Peeters et al., 2010) and it has been proposed to use subspace identification methods together with a shooting algorithm to extract nonlinear modes with broadband testing (Noël et al., 2016).

An approximate technique for the calculation of periodic solutions of nonlinear systems is the HBM, which is in literature sometimes attributed to Krylov and Bogoliubov (1936) [1]. However, it is noted that similar techniques have already been used before, e.g., in the work of Duffing (1918) in the appendix a Ritz-method with a fundamental harmonic ansatz function (and an ansatz function including the third harmonic) was proposed which is closely related to HBM. For the purpose of the calculation of nonlinear modes HBM approaches were used, for instance, by Szemplinska-Stupnicka (1983) for the approximation of nonlinear modes of continuous systems. In Arquier et al. (2006) the HBM was used in the framework of the asymptotic numerical method for the computation of nonlinear modes of simple 2DOF systems. More recently, Detroux (2016) has used the HBM for the calculation of nonlinear modes of a satellite structure. The works of Laxalde and Thouverez (2009) and Krack et al. (2013) addressed the computation of pseudo-periodic complex nonlinear modes. Moreover, Krack (2015) used the extended periodic motion concept for nonconservative systems (c.f. Definition 2.3) for the calculation of ENMs of larger scale FE models subjected to friction and contact nonlinearities.

3.1.2 Requirements and Approach for Numerical Nonlinear Modal Analysis

The field of numerical calculation of periodic solutions of systems with local nonlinearities is comparatively advanced. There are several examples, where numerical algorithms have successfully been applied to large scale industrial examples such as aircraft engines (Krack et al., 2017) or automotive disc brakes (Cochelin and Vergez, 2009). However, most publications focus on the calculation of FRFs, whereas the efficient calculation of nonlinear modes is less common. In particular, the capabilities of advanced computational algorithms in the context of nonlinear modal based system identification have not been exploited yet. Previous work in this field mostly relies on the shooting algorithm proposed by Peeters et al. (2009), which provides a high accuracy but is computationally comparatively expensive. Furthermore, the relation of numerical calculations to

---

[1] Therefore, the method is sometimes referred to as Krylov-Bogoliubov method or, particularly in system identification literature, as describing function method. It is emphasized, however, that the HBM is only a special case of these methods for periodic motions.

experimental data is rarely discussed and not exploited for the identification of predictive models.

The goal of this chapter is to propose a numerical algorithm which is more appropriate for the purpose of nonlinear system identification and which can be used for the derivation of predictive models. To this end, the following requirements have to be met:

1. high computational efficiency and robustness

2. direct comparability to experimental results

3. potential for the treatment of complex structures

4. extendability to nonsmooth and nonconservative nonlinearities

To fulfill these requirements, a HBM based approach is used instead of a shooting method. A conceptual advantage of the HBM is that the computational efficiency can be increased by the filtering of internal resonances. Whereas in shooting methods the complexity of the frequency-energy plot is solely determined by the system's properties, the HBM allows for a reduction of computational complexity by choosing the number of frequencies included in the ansatz functions. The filtering characteristic is particularly appealing in conjunction with experimentally obtained nonlinear modes as the quantitative measurement of internally resonant structures is currently infeasible and the role of damping for the practical significance of internal resonances is unclear (Hill et al., 2016). If the numerical simulations are compared to experimental results, it is possible to give an a priori estimate which frequencies are significant and chose a suitable ansatz function. Moreover, the results of the HBM are obtained in the frequency domain, which allows for a direct comparison with experimental results, which are typically obtained after WT or Fast Fourier Transform (FFT) of the measured signals. A particular advantage that can be exploited in cases when the frequency domain representation of nonlinear forces can be calculated analytically, is that measured Fourier coefficients can directly be inserted in a HBM based formulation of the equation of motion to identify coefficients of the nonlinear forces as shown in Chapter 5.2.

To retain generality the HBM approach is embedded in a general substructure framework, such that it can be used for the calculation of nonlinear modes of any spatially discretized structure with local nonlinearities. The emphasis is put on structures with smooth polynomial stiffness nonlinearities as these are the primary focus of the experimental analysis in
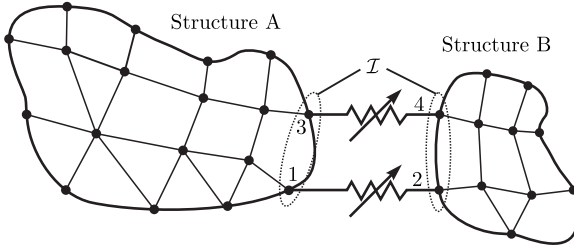
Figure 3.1: Discretized substructures coupled with nonlinear elements.

Chapter 6. However, it is desired that methods for the analysis of non-linearly damped and nonsmooth structures can be included. Finally, it is noted that recent developments in HBM based stability and bifurcation analysis provide the possibility of including these topics in the simulations (Detroux, 2016), although this is considered beyond the scope of this thesis.

3.2 Harmonic Balance Method

In this section, the HBM is derived in a general substructure framework based on the work of Reuss et al. (2012) and Voormeeren et al. (2011). The approach is adapted for the computation of nonlinear modes according to Definition 2.1. For the sake of clarity, the substructure formulation is derived in the physical domain, however, it is noted that it can be derived analogously in the frequency domain using a frequency based substructuring formulation or modal domain where it can be combined with model reduction techniques yielding a Component Mode Synthesis (CMS) formulation (De Klerk et al., 2008). The latter approach is briefly addressed in Section 3.2.5.

For illustration, an example of a mechanical system, which consists of two substructures A and B, as it is shown in Fig. 3.1, is considered. The substructures are spatially discretized, e.g., using the FE method, and each of the substructures can be modeled by a set of linear ODEs. The DOFs associated to the nodes at which the structures are coupled to one another are attributed to the set of interface DOFs $\mathcal{I}$. For the case of nonlinear modes as defined in Definition 2.1, the system is considered to be conservative such that the linear substructures as well as the coupling

forces are conservative. The equation of motion of a system of this form can be written as

$$\mathbf{M}\ddot{\boldsymbol{x}}(t) + \mathbf{K}\boldsymbol{x}(t) + \boldsymbol{f}_{\mathrm{nl}}(\boldsymbol{x}(t)) = \mathbf{0}, \tag{3.1}$$

where $\mathbf{M}$ and $\mathbf{K}$ contain the mass and stiffness matrices of all substructures in a block-diagonal form. In the example in Fig. 3.1 the mass and stiffness matrices are

$$\mathbf{M} = \mathrm{diag}\{\mathbf{M}_{\mathrm{A}}, \mathbf{M}_{\mathrm{B}}\} \quad \text{and} \quad \mathbf{K} = \mathrm{diag}\{\mathbf{K}_{\mathrm{A}}, \mathbf{K}_{\mathrm{B}}\}, \tag{3.2}$$

where $\mathbf{M}_{\mathrm{A}}$ and $\mathbf{M}_{\mathrm{B}}$ denote the mass matrices and $\mathbf{K}_{\mathrm{A}}$ and $\mathbf{K}_{\mathrm{B}}$ the stiffness matrices of the individual substructures. The vector $\boldsymbol{f}_{\mathrm{nl}}(\boldsymbol{x}(t))$ contains the coupling forces $\boldsymbol{\lambda}$ acting on the interface DOFs. The coupling forces $\boldsymbol{\lambda}$ can be written as (potentially nonlinear) functions of the (relative) displacement $\boldsymbol{u}(t)$ in the interface as

$$\boldsymbol{\lambda} = \boldsymbol{g}_{\mathrm{nl}}(\boldsymbol{u}(t)) \tag{3.3}$$

which are related to $\boldsymbol{x}(t)$ by the signed Boolean matrix $\mathbf{B}$ as

$$\boldsymbol{u}(t) = \mathbf{B}\boldsymbol{x}(t). \tag{3.4}$$

The relationship between the local coupling forces and the generalized force vector follows from the principle of virtual work:

$$\begin{aligned} \delta W = \delta \boldsymbol{x}^{\mathrm{T}} \boldsymbol{f}_{\mathrm{nl}} &\overset{!}{=} \delta \boldsymbol{u}^{\mathrm{T}} \boldsymbol{\lambda} = \delta \boldsymbol{x}^{\mathrm{T}} \mathbf{B}^{\mathrm{T}} \boldsymbol{\lambda} \quad \forall \delta \boldsymbol{x} \\ &\Rightarrow \boldsymbol{f}_{\mathrm{nl}} = \mathbf{B}^{\mathrm{T}} \boldsymbol{\lambda} \end{aligned} \tag{3.5}$$

which can be expressed in terms of the function $\boldsymbol{g}_{\mathrm{nl}}(\boldsymbol{u}(t))$ in Eq. (3.3) yielding

$$\boldsymbol{f}_{\mathrm{nl}}(\boldsymbol{x}(t)) = \mathbf{B}^{\mathrm{T}} \boldsymbol{g}_{\mathrm{nl}}(\boldsymbol{u}(t)) = \mathbf{B}^{\mathrm{T}} \boldsymbol{g}_{\mathrm{nl}}(\mathbf{B}\boldsymbol{x}(t)). \tag{3.6}$$

It is noted that the signed Boolean matrix $\mathbf{B}$ can be calculated based on the force equilibrium in the interface

$$\mathbf{L}^{\mathrm{T}} \boldsymbol{f}_{\mathrm{nl}}(t) = \mathbf{0}, \tag{3.7}$$

where $\mathbf{L}$ is a Boolean matrix localizing the interface DOFs within the set of global DOFs using the relation $\mathbf{B}^{\mathrm{T}} = \mathrm{null}(\mathbf{L}^{\mathrm{T}})$(Reuss et al., 2012; Voormeeren et al., 2011).

In the following, the linear substructures are coupled to one another with nonlinear elements such that the force $\boldsymbol{g}_{\mathrm{nl}}(\boldsymbol{u}(t))$ in Eq. (3.6) is a nonlinear function of $\boldsymbol{u}(t)$.

Definition 3.1. The DOFs which are linked to nonlinear coupling elements are included in the set $\mathcal{I}$ and called <u>nonlinear DOFs</u>. The number of nonlinear DOFs is N_{nl}. All generalized coordinates associated with the nonlinear DOFs are included in the vector $\boldsymbol{x}_{\mathrm{nl}}(t) \in \mathbb{R}^{N_{\mathrm{nl}}}$. The remaining DOFs are called <u>linear DOFs</u> and their generalized coordinates are included in the vector $\boldsymbol{x}_{\mathrm{ln}}(t) \in \mathbb{R}^{(N-N_{\mathrm{nl}})}$.

It is noted that the vector of relative generalized coordinates $\boldsymbol{u}(t)$ in the interface only depends on the nonlinear DOFs included in $\boldsymbol{x}_{\mathrm{nl}}(t)$, i.e., $\boldsymbol{g}_{\mathrm{nl}}(\boldsymbol{u}(t)) = \boldsymbol{g}_{\mathrm{nl}}(\boldsymbol{x}_{\mathrm{nl}}(t))$. Therefore, Eq. (3.1) can be rewritten as

$$\mathbf{M}\ddot{\boldsymbol{x}}(t) + \mathbf{K}\boldsymbol{x}(t) + \mathbf{B}^{\mathrm{T}}\boldsymbol{g}_{\mathrm{nl}}(\boldsymbol{x}_{\mathrm{nl}}(t)) = \mathbf{0}. \tag{3.8}$$

To include nonlinear forces in numerical simulations the HBM including higher harmonics is utilized to approximate those forces (Reuss et al., 2012). The HBM can also be interpreted as a Galerkin method with Fourier ansatz functions. The generalized displacements of the system $\boldsymbol{x}(t)$ are assumed to be periodic functions of time with the period length[2] $T = (2\pi)/\omega$ and can be represented by a Fourier series which is truncated to a finite number of harmonics N_h

$$\boldsymbol{x}(t) \approx \boldsymbol{x}_0 + \sum_{n=1}^{N_h} \boldsymbol{x}_{\mathrm{c},n} \cos(n\omega t) + \boldsymbol{x}_{\mathrm{s},n} \sin(n\omega t). \tag{3.9}$$

The assumption of periodicity does not pose any restriction in the context of nonlinear mode calculation as conservative nonlinear modes are periodic motions by definition (c.f. Definition 2.1). The Fourier series can be associated to the set of orthonormal Fourier basis functions

$$\mathcal{F} = \left\{ \frac{1}{\sqrt{T}} c_0 \right\} \cup \left\{ \sqrt{\frac{2}{T}} c_n(t), \sqrt{\frac{2}{T}} s_n(t) | n \in \mathbb{N} \right\}, \tag{3.10}$$

---

[2]The ansatz can be generalized to include subharmonic motions. Then the period length has to be chosen based on the lowest subharmonic frequency (c.f. Peter et al. (2014))

which includes the orthogonal ansatz functions

$$
\left.
\begin{aligned}
c_0 &= 1, \\
c_n(t) &= \cos\left(n\omega t\right), \\
s_n(t) &= \sin\left(n\omega t\right)
\end{aligned}
\right\} \quad \text{for } n \in \mathbb{N} \text{ and } t \in [0, T]. \tag{3.11}
$$

In the function space $\mathcal{F}$, the inner product of two functions $f(t)$ and $h(t)$ is defined as

$$
\langle f(t), h(t) \rangle = \int_0^T f(t)h(t)\mathrm{d}t. \tag{3.12}
$$

The ansatz functions in Eq. (3.11) can be written in a compact vector notation:

$$
\boldsymbol{\Gamma}(t) = [c_0, c_1(t), s_1(t), ..., c_{N_h}(t), s_{N_h}(t)]^{\mathrm{T}} = [\Gamma_1, ..., \Gamma_{2N_h+1}(t)]^{\mathrm{T}}. \tag{3.13}
$$

Using this vector of ansatz functions, the Fourier series in Eq. (3.9) can be written in a matrix-vector notation

$$
\boldsymbol{x}(t) = \mathbf{V}(t)^{\mathrm{T}}\boldsymbol{x}, \tag{3.14}
$$

where $\mathbf{V}(t)^{\mathrm{T}} \in \mathbb{R}^{N \times N(2N_h+1)}$ is defined as

$$
\begin{aligned}
\mathbf{V}(t)^{\mathrm{T}} &= [c_0\mathbf{I}_N, c_1(t)\mathbf{I}_N, s_1(t)\mathbf{I}_N, ..., c_{N_h}(t)\mathbf{I}_N, s_{N_h}(t)\mathbf{I}_N]^{\mathrm{T}} \\
&= \left(\boldsymbol{\Gamma}(t)^{\mathrm{T}} \otimes \mathbf{I}_N\right)^{\mathrm{T}},
\end{aligned} \tag{3.15}
$$

with the $N \times N$ identity matrix $\mathbf{I}_N$ and the Kronecker product $\otimes$. Herein, $\boldsymbol{x}$ contains the Fourier coefficients of the generalized displacement, i.e., $\boldsymbol{x} = [\boldsymbol{x}_0^{\mathrm{T}}, \boldsymbol{x}_{\mathrm{c},1}^{\mathrm{T}}, \boldsymbol{x}_{\mathrm{s},1}^{\mathrm{T}}, ..., \boldsymbol{x}_{\mathrm{c},N_h}^{\mathrm{T}}, \boldsymbol{x}_{\mathrm{s},N_h}^{\mathrm{T}}]^{\mathrm{T}} \in \mathbb{R}^{N(2N_h+1)}$. For the Galerkin method, the virtual displacements are expanded using the same ansatz functions $\boldsymbol{\Gamma}(t)$ yielding

$$
\delta\boldsymbol{x}(t) = \mathbf{V}(t)^{\mathrm{T}}\delta\boldsymbol{x}. \tag{3.16}
$$

The virtual action integral of the system in Eq. (3.1) can be written as

$$
0 = \delta A = \int_0^T \delta W \mathrm{d}t = \int_0^T \delta\boldsymbol{x}(t)^{\mathrm{T}}\left(\mathbf{M}\ddot{\boldsymbol{x}}(t) + \mathbf{K}\boldsymbol{x}(t) + \boldsymbol{f}_{\mathrm{nl}}(\boldsymbol{x}(t))\right)\mathrm{d}t \ \ \forall\delta\boldsymbol{x}(t),
$$

$$
\tag{3.17}
$$

which has to vanish for all virtual displacements. The ansatz functions in
Eq. (3.14) and their time derivatives

$$
\begin{aligned}
\dot{\boldsymbol{x}}(t) &= \left(\boldsymbol{\Gamma}(t)^{\mathrm{T}}\nabla \otimes \mathbf{I}_N\right)\boldsymbol{x} = \mathbf{V}(t)^{\mathrm{T}}(\nabla \otimes \mathbf{I}_N)\boldsymbol{x} \\
\ddot{\boldsymbol{x}}(t) &= \left(\boldsymbol{\Gamma}(t)^{\mathrm{T}}\nabla^2 \otimes \mathbf{I}_N\right)\boldsymbol{x} = \mathbf{V}(t)^{\mathrm{T}}(\nabla^2 \otimes \mathbf{I}_N)\boldsymbol{x}
\end{aligned}
\tag{3.18}
$$

with (Laxalde et al., 2008)

$$
\nabla = \mathrm{diag}\left\{0, \begin{bmatrix} 0 & \omega \\ -\omega & 0 \end{bmatrix}, ..., \begin{bmatrix} 0 & N_h\omega \\ -N_h\omega & 0 \end{bmatrix}\right\} \text{ and } \nabla^2 = \nabla\nabla \quad (3.19)
$$

are inserted in Eq. (3.17) together with the virtual displacement field ex-
panded on the same ansatz functions (c.f. Eq. (3.16)) yielding

$$
0 = \delta A =
$$
$$
\delta\boldsymbol{x}^{\mathrm{T}} \int_0^T \left(\mathbf{V}(t)\mathbf{M}\mathbf{V}(t)^{\mathrm{T}}(\nabla^2 \otimes \mathbf{I}_N)\boldsymbol{x} + \mathbf{V}(t)\mathbf{K}\mathbf{V}(t)^{\mathrm{T}}\boldsymbol{x} + \mathbf{V}(t)\boldsymbol{f}_{\mathrm{nl}}(\boldsymbol{x}(t))\right)\mathrm{d}t.
$$
$$
\tag{3.20}
$$

The orthogonality properties of the ansatz functions yield

$$
\langle \Gamma_i(t), \Gamma_j(t) \rangle = \int_0^T \Gamma_i(t)\Gamma_j(t)\mathrm{d}t = \delta_{ij}G_{ij}.
\tag{3.21}
$$

where δ_{ij} denotes the Kronecker delta and G_{ij} a constant scaling factor
related to the norm of the ansatz functions in $\boldsymbol{\Gamma}(t)$. For the orthonormal
Fourier basis functions in $\mathcal{F}$, the ansatz functions are normalized, i.e., then
$G_{ij}^{\mathcal{F}} = 1$. Therefore, a normalization is performed upon integration, to
obtain the Fourier coefficients by introducing a matrix $\mathbf{G} = \mathrm{diag}\{1/G_{ii}\}$.
The orthogonality relations allow for a direct evaluation of the linear terms
of Eq. (3.20) yielding

$$
0 = \delta A = \delta\boldsymbol{x}^{\mathrm{T}}\left(\mathbf{H}(\omega)\boldsymbol{x} + \mathbf{G}\int_0^T \mathbf{V}(t)\boldsymbol{f}_{\mathrm{nl}}(\boldsymbol{x}(t))\mathrm{d}t\right) \quad \forall\delta\boldsymbol{x}
\tag{3.22}
$$

with the blockdiagonal dynamic stiffness matrix

$$
\mathbf{H}(\omega) = \mathrm{diag}\left\{\mathbf{K}, (-\omega^2\mathbf{M} + \mathbf{K}), ..., (-N_h{}^2\omega^2\mathbf{M} + \mathbf{K})\right\},
\tag{3.23}
$$

which can be written in a compact form as

$$\mathbf{H}(\omega) = \nabla^2 \otimes \mathbf{M} + \mathbf{I}_{2N_h+1} \otimes \mathbf{K}. \tag{3.24}$$

This type of Galerkin projection can be viewed as a means of transforming the equation of motion into the frequency domain as in this case a Fourier series is used as projection basis. However, it should be noted that also modified projection bases can be used, for instance to compute complex nonlinear modes (c.f. Section 3.5) or quasi-periodic motions (Guskov and Thouverez, 2012; Krack et al., 2016). The transformation of the nonlinear terms of Eq. (3.22), i.e.,

$$\boldsymbol{f}_{\mathrm{nl}}(\boldsymbol{x}, \omega) = \mathbf{G} \int_0^T \mathbf{V}(t) \boldsymbol{f}_{\mathrm{nl}}(\boldsymbol{x}(t)) \mathrm{d}t \tag{3.25}$$

into the frequency domain is nontrivial, as for most nonlinear functions $\boldsymbol{f}_{\mathrm{nl}}(\boldsymbol{x}(t))$ no simple orthogonality relations are retained. There are different methods for the evaluation of these Fourier integrals and its realization is regarded a key factor for a computational efficient HBM algorithm (Petrov and Ewins, 2002). Therefore, the implementation within this work is discussed in some detail in Section 3.2.4.

The general problem which has to be solved to obtain periodic solutions can be formulated as

$$\mathbf{H}(\omega)\boldsymbol{x} + \boldsymbol{f}_{\mathrm{nl}}(\boldsymbol{x}, \omega) = \mathbf{0}, \tag{3.26}$$

which is an implicit nonlinear algebraic equation system of dimension $N(2N_h + 1)$. It should be noted that the number of unknowns in the system in Eq. (3.26) exceeds the number of equations by one, as the frequency is unknown as well as all Fourier coefficients. Furthermore, there exists an infinite number of solutions dependent on the magnitude of $\boldsymbol{x}$. Therefore, in the next section a normalization procedure is discussed to obtain a specific solution.

3.2.1 Phase Normalization and Continuation on Energy

The implicit nonlinear algebraic equation in Eq. (3.26) has to be solved iteratively. Therefore, a residual $\boldsymbol{r}(\boldsymbol{x}, \omega)$ is defined as

$$\boldsymbol{r}(\boldsymbol{x}, \omega) = \mathbf{H}(\omega)\boldsymbol{x} + \boldsymbol{f}_{\mathrm{nl}}(\boldsymbol{x}, \omega), \tag{3.27}$$

which has to be iterated towards zero to obtain an approximation of a periodic solution. As explained in Chapter 2, a nonlinear mode consists of infinitely many periodic nonlinear modal motions, e.g., solutions of Eq. (3.27). Therefore, a normalization procedure with respect to some parameter has to be applied to obtain a specific solution. The parameter is then varied by a path-following algorithm to calculate a branch of solutions. For the normalization, different strategies can be found in literature. Based on the fact that the frequency of oscillation may change depending on the total energy, strategy (a), which is for instance followed by Peeters et al. (2009), is to use the frequency (or period time) as parameter. This method can be applied in cases when the nonlinear modal frequency changes, whereas problems are encountered when the nonlinear modal frequency remains constant with energy, e.g., in the linear regime. Strategy (b) is to directly use the initial displacement or velocity as a parameter, which can be adapted to frequency domain approaches by simply setting one Fourier coefficient to a specific value (Laxalde and Thouverez, 2009). Method (b) inherently requires the choice of a master coordinate x^{m}, for which the Fourier coefficient is used as parameter. This approach can cause problems in cases where a strong change in mode shape occurs, e.g., caused by an internal resonance, such that the master coordinate may actually go to zero. Furthermore, in cases where strong and sudden changes of the system behavior are expected, e.g., due to nonsmooth behavior, the method may affect the convergence of the solution process. Alternatively, strategy (c) is to directly parametrize the solution branch in the frequency-energy plot with respect to the energy. This strategy is, for instance, followed by Arquier et al. (2006), who parametrized the solutions with respect to the total energy in the system. For frequency domain approaches Krack et al. (2013) propose to use the average kinetic energy over one period

$$E_{\mathrm{kin}} = \frac{1}{T} \int_0^T \frac{1}{2} \dot{\boldsymbol{x}}(t)^{\mathrm{T}} \mathbf{M} \dot{\boldsymbol{x}}(t) \mathrm{d}t, \tag{3.28}$$

because this quantity is independent of the nonlinear force and can be directly evaluated in the frequency domain with Parseval's theorem yielding

$$E_{\mathrm{kin}} = -\frac{1}{4} \boldsymbol{x}^{\mathrm{T}} (\nabla^2 \otimes \mathbf{M}) \boldsymbol{x}. \tag{3.29}$$

The advantage of the energy based parametrization is that the energy is dependent on the frequency and the complete nonlinear mode shape, such that problems related to the strategies (a) and (b) are circumvented and a robust computational procedure is achieved. With this additional energy equation the number of unknowns is equal to the number of equations in Eq. (3.27).

Another issue, that is well-known for autonomous systems, is that the periodic solutions form closed curves in phase space and the absolute phase is arbitrary. Therefore, the initial condition is not unique, such that the solution of Eq. (3.27) is also not unique, which may cause numerical problems. Hence, a phase normalization is performed. One strategy for phase normalization, which is for instance used by Peeters et al. (2009) in the shooting method, is to set the initial condition of the velocity of a specific DOF to zero, i.e., $\dot{x}^{\mathrm{m}}(t = 0) = 0$. By doing this, the number of unknowns is reduced by one and the system becomes overdetermined. The resulting system can then be solved in a least squares sense. A different approach is to introduce an artificial damping term, as proposed by Arquier et al. (2006), which goes to zero in the case of a periodic motion. This method increases the number of unknowns by one, such that a unique solution can be obtained for the system with phase condition. It is interesting to note, that the approaches by Laxalde and Thouverez (2009) and Krack (2015) for the calculation of nonconservative nonlinear modes essentially lead to the same formulation, i.e., an additional damping parameter is introduced which is zero in the case of a conservative system.

In this work a different method for the phase normalization is adopted, which does neither require the solution of an overdetermined system nor the calculation of artificial parameters. It is shown by Petrov (2012) for the case of limit cycle oscillations that the phase condition in time domain can be transferred into the frequency domain by setting one Fourier coefficient of the Fourier series in Eq. (3.14) to an admissible arbitrary value, which is below the maximum amplitude of vibration. In the case of nonlinear mode calculation the condition

$$x_{\mathrm{s},1}^{\mathrm{m}} = 0, \tag{3.30}$$

is a natural choice for fixing the phase. For the HBM, the phase condition can directly be included in the ansatz functions with which the Galerkin projection is carried out, reducing the dimension of the function space $\mathcal{F}$ by one. In other words, a periodic solution is calculated which inherently

fulfills the phase condition stated in Eq. (3.30). This approach can be extended to simplify the computation of monophase nonlinear modes as explained in Section 3.2.5.

3.2.2 Condensation to Nonlinear Degrees of Freedom

A computational advantage which can be exploited if nonlinear modes are calculated with a HBM approach is that the resulting algebraic system in Eq. (3.26) allows for an exact condensation on the nonlinear DOFs in cases in which there is a (relative) motion in the interface. Thereby, the dimension of the problem can be reduced from $N(2N_h+1)$ to $N_{nl}(2N_h+1)$, which can considerably reduce the computational burden particularly for large linear models with few nonlinear DOFs, i.e., for $N_{nl} << N$. As proposed by Nacivet et al. (2003) the problem stated in Eq. (3.26) can be partitioned by separating the linear and nonlinear DOFs:

$$\begin{bmatrix} \mathbf{H}_{lnln}(\omega) & \mathbf{H}_{lnnl}(\omega) \\ \mathbf{H}_{nlln}(\omega) & \mathbf{H}_{nlnl}(\omega) \end{bmatrix} \begin{bmatrix} \boldsymbol{x}_{ln} \\ \boldsymbol{x}_{nl} \end{bmatrix} + \begin{bmatrix} \mathbf{0} \\ \boldsymbol{g}_{nl}(\boldsymbol{x}_{nl}, \omega) \end{bmatrix} = \mathbf{0}. \tag{3.31}$$

The nonlinear forces acting on the linear part of the structure are zero, such that the first line of Eq. (3.31) can be explicitly solved for $\boldsymbol{x}_{ln}$ and inserted in the second line yielding

$$\left(\mathbf{H}_{nlnl}(\omega) - \mathbf{H}_{nlln}(\omega)\mathbf{H}_{lnln}^{-1}(\omega)\mathbf{H}_{lnnl}(\omega) \right) \boldsymbol{x}_{nl} + \boldsymbol{g}_{nl}(\boldsymbol{x}_{nl}, \omega) = \mathbf{0}, \tag{3.32}$$

which can be written in a compact form as

$$\mathbf{H}_{red}(\omega)\boldsymbol{x}_{nl} + \boldsymbol{g}(\boldsymbol{x}_{nl}, \omega) = \mathbf{0}. \tag{3.33}$$

Hence, the size of the problem which has to be solved iteratively is determined solely by the number of nonlinear DOFs and the linear DOFs $\boldsymbol{x}_{ln}$ can be calculated a posteriori by evaluating the first line of Eq. (3.31):

$$\boldsymbol{x}_{ln} = \mathbf{H}_{lnln}^{-1}(\omega)\mathbf{H}_{lnnl}(\omega)\boldsymbol{x}_{nl} = \mathbf{A}\boldsymbol{x}_{nl}. \tag{3.34}$$

For the evaluation of the energy in Eq. (3.29) the matrix $\check{\mathbf{M}}(\omega) = \nabla^2 \otimes \mathbf{M}$ is partitioned analogously to the dynamic stiffness matrix. Using Eq. (3.34) the energy can be expressed as a function of the nonlinear displacements

as

$$
\begin{aligned}
E_{\text{kin}} &= -\frac{1}{4} \boldsymbol{x}_{\text{nl}}^{\text{T}} \left(\check{\mathbf{M}}_{\text{nlnl}} + \mathbf{A}^{\text{T}} \check{\mathbf{M}}_{\text{lnnl}} + \check{\mathbf{M}}_{\text{nlln}} \mathbf{A} + \mathbf{A}^{\text{T}} \check{\mathbf{M}}_{\text{lnln}} \mathbf{A} \right) \boldsymbol{x}_{\text{nl}} \\
&= -\frac{1}{4} \boldsymbol{x}_{\text{nl}}^{\text{T}} \check{\mathbf{M}}_{\text{red}}(\omega) \boldsymbol{x}_{\text{nl}}.
\end{aligned}
\tag{3.35}
$$

Although the exact condensation considerably reduces the computational effort, when the system is modeled with a large number of linear DOFs, it should be noted that the calculation of the reduced dynamic stiffness matrix $\mathbf{H}_{\text{red}}(\omega)$ involves the calculation of the inverse $\mathbf{H}_{\text{lnln}}^{-1}(\omega)$. Furthermore, these matrices depend on ω which makes a recalculation of $\mathbf{H}_{\text{red}}(\omega)$ in every iteration necessary. As this may generally diminish the computational advantage, a reformulation of the system in mixed-modal-physical coordinates based on a Craig-Bampton reduction basis is proposed in Section 3.2.5.

3.2.3 Predictor-Corrector Method

The residual of the reduced system of equations can be formulated together with the condition for the parametrization with respect to the mean kinetic energy as

$$
\boldsymbol{r}_{\text{e}}(\boldsymbol{x}_{\text{nl}}, \omega) = \begin{bmatrix} \mathbf{H}_{\text{red}}(\omega) \boldsymbol{x}_{\text{nl}} + g(\boldsymbol{x}_{\text{nl}}, \omega) \\ E_{\text{kin}} + \frac{1}{4} \boldsymbol{x}_{\text{nl}}^{\text{T}} \check{\mathbf{M}}_{\text{red}}(\omega) \boldsymbol{x}_{\text{nl}} \end{bmatrix}.
\tag{3.36}
$$

For the iterative solution of a system of nonlinear algebraic equations there exist numerous methods (Dahmen and Reusken, 2008). In the case of nonlinear mode calculation, multiple solutions may occur for the same energy, e.g., caused by internal resonances. Therefore, the solution method has to be combined with a path-following algorithm to be able to calculate a complete branch of the frequency-energy plot. To this end, several path-following algorithms are available (Seydel, 2009). For the purpose of nonlinear mode calculation the performance of several algorithms has been explored by Jerschl et al. (2014a,b). In this thesis, a predictor-corrector method which is based on the work of Allgower and Georg (1994) is implemented, which is briefly outlined in the following. For notational convenience an extended vector of unknowns $\boldsymbol{y} = [\boldsymbol{x}_{\text{nl}}, \omega, E_{\text{kin}}]^{\text{T}}$ is introduced, where E_{kin} is the path following parameter. For the prediction, a tangent

predictor step is used based on the previous solution, i.e.,

$$\boldsymbol{y}_{m+1}^{\mathrm{pred}} = \boldsymbol{y}_m + h\boldsymbol{v}_m, \tag{3.37}$$

where $\boldsymbol{v}_m$ denotes the normalized tangent vector at the m-th point along the solution curve and h a step size factor. The corrector step is performed using Newton-like iterations

$$
\begin{aligned}
\boldsymbol{y}_{m+1}^{i+1} &= \boldsymbol{y}_{m+1}^i - \begin{bmatrix} \mathbf{J} \\ \boldsymbol{v}_{m+1}^{i\ \mathrm{T}} \end{bmatrix}^{-1} \begin{bmatrix} \boldsymbol{r}_{\mathrm{e}}^i \\ \mathbf{0} \end{bmatrix}, \\
\boldsymbol{v}_{m+1}^{i+1} &= \boldsymbol{v}_{m+1}^i - \begin{bmatrix} \mathbf{J} \\ \boldsymbol{v}_{m+1}^{i\ \mathrm{T}} \end{bmatrix}^{-1} \begin{bmatrix} \mathbf{J}\boldsymbol{v}_{m+1}^i \\ \mathbf{0} \end{bmatrix},
\end{aligned}
\tag{3.38}
$$

where i denotes the iteration number and $\mathbf{J}$ the Jacobian matrix of the extended system in Eq. (3.36), i.e.,

$$\mathbf{J} = \begin{bmatrix} \dfrac{\partial \boldsymbol{r}_{\mathrm{e}}(\boldsymbol{x}_{\mathrm{nl}}, \omega)}{\partial \boldsymbol{x}_{\mathrm{nl}}}, \dfrac{\partial \boldsymbol{r}_{\mathrm{e}}(\boldsymbol{x}_{\mathrm{nl}}, \omega)}{\partial \omega}, \dfrac{\partial \boldsymbol{r}_{\mathrm{e}}(\boldsymbol{x}_{\mathrm{nl}}, \omega)}{\partial E_{\mathrm{kin}}} \end{bmatrix}. \tag{3.39}$$

With this Newton-like corrector step the residual $\boldsymbol{r}_{\mathrm{e}}$ is iterated towards zero with the condition

$$\left(\boldsymbol{y}_{m+1}^{i+1} - \boldsymbol{y}_{m+1}^i \right) \perp \boldsymbol{v}_{m+1}^i, \tag{3.40}$$

i.e., the iterations are performed in a hyperplane perpendicular to the tangent vector $\boldsymbol{v}_{m+1}^{i\ \mathrm{T}}$. Simultaneously, the tangent vector is updated in each iteration by iterating $\mathbf{J}\boldsymbol{v}_{m+1}^i$ to zero with the condition

$$\left(\boldsymbol{v}_{m+1}^{i+1} - \boldsymbol{v}_{m+1}^i \right) \perp \boldsymbol{v}_{m+1}^i. \tag{3.41}$$

This type of Newton-like continuation algorithm, which is is also implemented, e.g., in the MATCONT software package (Dhooge et al., 2003), provides robust convergence properties for nonlinear mode calculation. Furthermore, it has been shown by Detroux et al. (2015) that this method can be easily extended for the use in bifurcation analysis.

A critical factor regarding the computational performance of a predictor-corrector algorithm is the choice of the step length h for the prediction (c.f. Eq. (3.37)). If the step size is chosen to be a constant factor, at most a suboptimal computational performance can be achieved. Therefore, the step size factor is typically adjusted based on the convergence properties
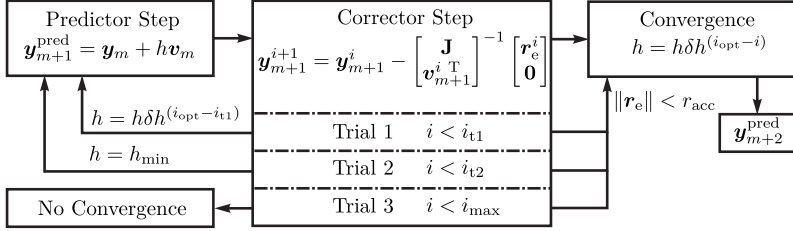
Figure 3.2: Schematic sketch of step size algorithm.

of the corrector step, such that an optimal number of corrections is achieved (Seydel, 2009). In this work this strategy is augmented by a multi-level trial and error procedure. A trial and error based step size control is found to be beneficial in cases where strong and sudden changes in the solution curve appear (Niet, 2002). This is, for instance, expected for nonsmooth problems (c.f. Section 3.4). The proposed step size algorithm is shown in Fig. 3.2. The predictor step is performed with a given step size h. Then the corrector step iterates the residual towards zero. In a first trial, a small number of i_{t1} iterations is performed. If no convergence is achieved within $i < i_{t1}$ iterations, then the predictor step is repeated with a reduced step size. The step size is adjusted based on a pre-set number of optimal iterations i_{opt} and a step size multiplier $\delta h > 1$. In the second trial stage a larger number of corrector iterations i_{t2} is tolerated, before prediction is repeated and the step size is reduced to the minimal value h_{min}. In the third and last trial the maximal number of correction iterations i_{max} is performed. In the case of convergence in one of the trial stages, i.e., if the norm of the residual is smaller than an accepted value r_{acc}, a new step size is calculated for the prediction of the next point on the curve $\boldsymbol{y}_{m+2}^{pred}$.

3.2.4 Analytical Formulations for Nonlinear Forces and Jacobian Matrices

For the solution of the residual equation the nonlinear forces have to be evaluated in the frequency domain and the Jacobian matrix of the system has to be calculated. The calculation of the Jacobian matrix of the

linear part of the system is rather straightforward[3]. In the following the attention is drawn towards the evaluation of the nonlinear forces and their derivatives.

For the calculation of the nonlinear forces in the frequency domain the integral in Eq. (3.25) has to be evaluated. Generally, the functional dependence of the Fourier coefficients of the force on the Fourier coefficients of the displacements is unknown and, in contrast to the linear forces, no simple orthogonality relations can be found which would facilitate the evaluation. As shown above, in addition to the nonlinear forces, also their derivatives with respect to the displacement and the frequency are required for the solution process. The efficient realization of this task often turns out to be a bottleneck of the computational algorithm such that numerous publications are dedicated to this subject. The most common approach for the solution of the integral in Eq. (3.25) is the Alternating-Frequency-Time (AFT) method, which has been proposed by Cameron and Griffin (1989). The basic idea of AFT algorithms is to exploit the efficiency of the FFT to transform the Fourier coefficients of the displacement into the time domain, calculate the nonlinear forces in the time domain and transform the non-linear forces back into the frequency domain. The main advantage of this method is that it is applicable to any kind of nonlinearity and the implementation effort is limited. Furthermore, the method provides a good computational performance, if it is combined with a semi-analytic evaluation of the Jacobian matrix as proposed by Cardona et al. (1994). A different approach for the evaluation of the nonlinear forces is the combination of a quadratic recast, i.e., a reformulation of the problem yielding polynomial nonlinearities with at most quadratic terms, and the asymptotic numerical method (ANM), which allows for the calculation of the nonlinear forces directly in the frequency domain (Cochelin and Vergez, 2009). Besides the computational efficiency of this method, it has the drawback that it requires the quadratic recast of the system, which is particularly difficult to achieve for systems with nonsmooth nonlinearities.

In this work a different approach is used, with which the dependency of the Fourier coefficients of the nonlinear forces and their derivatives in the frequency domain are calculated analytically in closed form. This method provides the advantage of a high computational efficiency, but does not require the quadratic recast of the system, such that it can be easily combined

---

[3]For completeness all derivatives of the linear parts of the condensed system are included in Appendix B.

with well-known approaches for the treatment of nonsmooth nonlinearities, which typically rely on the AFT method or the Mixed Shooting HBM (c.f. Section 3.4). The method proposed here can be regarded as a generalization of the work by Petrov and Ewins (2002), who derived an analytical formulation for the treatment of nonlinear contact forces. The focus in this thesis is put on polynomial nonlinearities, however, the general idea is transferable to other types of nonlinearity. It is noted that a related approach has been used by Krack et al. (2013) for systems with distinct states and polynomial nonlinearties, under application of the convolution theorem.

In the following, for notational convenience, the local nonlinear force of a single nonlinear DOF is considered, however, the treatment of multiple nonlinear DOFs is straightforward. The local nonlinear force of a specific nonlinear DOF can be written according to Eq. (3.25) as

$$g_{nl}(\boldsymbol{u}, \omega) = \mathbf{G} \int_0^T \boldsymbol{\Gamma}(t) g_{nl}(u(t)) \mathrm{d}t = \int_0^T \boldsymbol{\Gamma}_+(t) g_{nl}(\boldsymbol{\Gamma}(t)^{\mathrm{T}} \boldsymbol{u}) \mathrm{d}t \quad (3.42)$$

with

$$\boldsymbol{\Gamma}_+(t) = \mathbf{G} \boldsymbol{\Gamma}(t) \tag{3.43}$$

and $\boldsymbol{u}$ being the Fourier coefficients of the local displacements. The fundamental idea is to separate the time dependent terms in the integral from the Fourier coefficients, such that the integral can be solved analytically and the integration is independent of the Fourier coefficients in $\boldsymbol{u}$. If this separation is possible, then Eq. (3.42) can be replaced by a simple matrix-vector multiplication

$$g_{nl}(\boldsymbol{u}, \omega) = \kappa \mathbf{W}(\omega) \check{\boldsymbol{u}}(\boldsymbol{u}) \tag{3.44}$$

where κ is some coefficient representing the nonlinear stiffness and the matrix $\mathbf{W}(\omega)$ can be calculated analytically by integration of

$$\mathbf{W}(\omega) = \int_0^T \boldsymbol{\Gamma}_+(t) \check{\boldsymbol{\Gamma}}(\boldsymbol{\Gamma}(t))^{\mathrm{T}} \mathrm{d}t. \tag{3.45}$$

Herein the $(\check{\cdot})$ indicates that the vector $\check{\boldsymbol{u}}(\boldsymbol{u})$ is a vector containing the Fourier coefficients $\boldsymbol{u}$ and the vector $\check{\boldsymbol{\Gamma}}(\boldsymbol{\Gamma}(t))$ is a vector containing the

ansatz functions included in $\mathbf{\Gamma}(t)$. The practical calculation of these vectors is illustrated at the examples of a monomial stiffness nonlinearity.

Example 3.1. Consider a nonlinear function of the monomial form

$$g_{\mathrm{nl}}(u(t)) = \kappa(u(t))^p, \tag{3.46}$$

where κ denotes the coefficient of the monomial and p its degree. The Fourier coefficients of the monomial force can be calculated with Eq. (3.42) as

$$g_{\mathrm{nl}}(\boldsymbol{u}, \omega) = \int_0^T \mathbf{\Gamma}_+(t) g(\mathbf{\Gamma}(t)^{\mathrm{T}} \boldsymbol{u}) \mathrm{d}t = \int_0^T \mathbf{\Gamma}_+(t) \kappa(\mathbf{\Gamma}(t)^{\mathrm{T}} \boldsymbol{u})^p \mathrm{d}t. \tag{3.47}$$

Which includes a polynomial of the form

$$(\mathbf{\Gamma}(t)^{\mathrm{T}} \boldsymbol{u})^p = (\Gamma_1(t) u_1 + ... + \Gamma_K(t) u_K)^p, \tag{3.48}$$

where $K = 2N_h + 1$ denotes the number of elements included in $\mathbf{\Gamma}(t)$ and $\boldsymbol{u}$ respectively. The polynomial can be expanded and written as a multinomial sum in a multi-index notation as

$$(\mathbf{\Gamma}(t)^{\mathrm{T}} \boldsymbol{u})^p = \sum_{k_1 + ... + k_K = p} \binom{p}{k_1, ..., k_{N_\eta}} (\Gamma_1(t) u_1)^{k_1} ... (\Gamma_K(t) u_K)^{k_K} \tag{3.49}$$

which contains

$$\eta = \binom{K + p - 1}{p} = \binom{2N_h + p}{p} = \frac{(2N_h + p)!}{(2N_h)! p!} \tag{3.50}$$

summands. Each of these summands is a product of monomials included in $\mathbf{\Gamma}(t)$ and $\boldsymbol{u}$ up to power p and a constant represented by the binomial coefficient. The expanded polynomial can then be written in terms of two vectors $\check{\mathbf{\Gamma}}(\mathbf{\Gamma}(t))$ and $\check{\boldsymbol{u}}(\boldsymbol{u})$ of the size $\eta \times 1$ such that the nonlinear force can be rearranged as

$$\boldsymbol{g}_{\mathrm{nl}}(\boldsymbol{u}, \omega) = \kappa \int_0^T \mathbf{\Gamma}_+(t) \check{\mathbf{\Gamma}}(\mathbf{\Gamma}(t)) \check{\boldsymbol{u}}(\boldsymbol{u}) \mathrm{d}t, \tag{3.51}$$

which is the form of Eq. (3.44) and allows for an analytical integration of the time dependent parts.

Example 3.1 illustrates how the nonlinear forces can be calculated analytically in the frequency domain. The advantage of the proposed method is that the obtained expressions for the nonlinear forces are exact and do not involve any numerical errors. Furthermore, the calculation of the Jacobian matrix of the nonlinear force can also be performed analytically yielding

$$\frac{\partial g_{\mathrm{nl}}(\boldsymbol{x}_{\mathrm{nl}}, \omega)}{\partial \boldsymbol{x}_{\mathrm{nl}}} = \kappa \mathbf{W}(\omega) \frac{\partial \check{\boldsymbol{u}}(\boldsymbol{x}_{\mathrm{nl}})}{\partial \boldsymbol{x}_{\mathrm{nl}}} \tag{3.52}$$

and

$$\frac{\partial g_{\mathrm{nl}}(\boldsymbol{x}_{\mathrm{nl}}, \omega)}{\partial \omega} = \kappa \frac{\partial \mathbf{W}(\omega)}{\partial \omega} \check{\boldsymbol{u}}(\boldsymbol{x}_{\mathrm{nl}}). \tag{3.53}$$

The calculation of the matrix $\mathbf{W}(\omega)$ involves the analytical integration of a potentially large matrix of combinations of trigonometric functions. For instance, for the polynomial stiffness nonlinearity the dimensions of the matrix is $\eta \times 2N_h + 1$, where η increases rapidly for an increasing number of harmonics and degree of the polynomial. However, the integration only has to be performed once for each type of nonlinear function and number of harmonics, yielding a closed form solution for the nonlinear force and their derivatives which can then be used for the calculation of arbitrary systems including the respective nonlinearity.

It is noted that the proposed approach is generally not limited to contact (c.f. Petrov and Ewins (2002)) or polynomial stiffness nonlinearities, but can be extended to any nonlinear function which allows for a separation of time and amplitude dependent terms of the integral in Eq. (3.25). For piecewise defined functions, the integral generally has to be split between different state transitions instead of an integration over the whole period (Krack et al., 2013; Petrov and Ewins, 2002). The state transitions can be efficiently calculated with the method proposed by Boyd (2006). In the numerical code used in this thesis three different nonlinearities are implemented: polynomial stiffness, polynomial damping and piecewise linear functions[4]. The formulations for these three types of nonlinearities are summarized in Tab. 3.1.

---

[4]Details the derivation of the analytical formulation for the piecewise linear forces can be found in Peter et al. (2014).
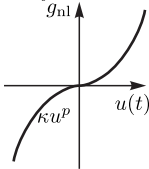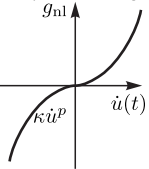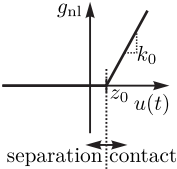
	Poly. Stiffness	Poly. Damping	Piecewise Linear
$g_{\mathrm{nl}}(u(t))$	$\kappa(u(t))^p$	$\kappa(\dot{u}(t))^p$	$\begin{cases} k_0(u(t) - z_0) & \text{con.} \\ 0 & \text{sep.} \end{cases}$
$\boldsymbol{g}_{\mathrm{nl}}(\boldsymbol{u},\omega)$	$\kappa\mathbf{W}\check{\boldsymbol{u}}(\boldsymbol{u})$	$\kappa\mathbf{W}(\omega)\check{\boldsymbol{u}}(\boldsymbol{u})$	$\begin{cases} k_0(\mathbf{W}(\omega)\boldsymbol{u} - \boldsymbol{w}(\omega)z_0) & \text{con.} \\ 0 & \text{sep.} \end{cases}$
η	$\dfrac{(2N_h + p)!}{(2N_h)!p!}$	$\dfrac{(2N_h + p)!}{(2N_h)!p!}$	$2N_h + 1$
$\dfrac{\partial \boldsymbol{g}_{\mathrm{nl}}(u,\omega)}{\partial \boldsymbol{u}}$	$\kappa\mathbf{W}\dfrac{\partial\check{\boldsymbol{u}}(\boldsymbol{u})}{\partial\boldsymbol{u}}$	$\kappa\mathbf{W}\dfrac{\partial\check{\boldsymbol{u}}(\boldsymbol{u})}{\partial\boldsymbol{u}}$	$\begin{cases} k_0\mathbf{W} & \text{con.} \\ 0 & \text{sep.} \end{cases}$
$\dfrac{\partial \boldsymbol{g}_{\mathrm{nl}}(u,\omega)}{\partial \omega}$	0	$\kappa p\omega^{p-1}\mathbf{W}\check{\boldsymbol{u}}(\boldsymbol{u})$	$\begin{cases} k_0\left(\dfrac{\partial\mathbf{W}(\omega)}{\partial\omega}\boldsymbol{u} - \dfrac{\partial\boldsymbol{w}(\omega)}{\partial\omega}z_0\right) & \text{c.} \\ 0 & \text{s.} \end{cases}$

Table 3.1: Summary of analytical formulations of nonlinear forces and their derivatives in the frequency domain.

3.2.5 Computational Simplifications

The HBM algorithm described above is generally suitable for the calculation of nonlinear modes of systems with many DOFs. However, the computational burden can be further reduced for certain classes of systems and nonlinear modes. Furthermore, the number of linear DOFs can be reduced and the problem can be written in mixed-modal-physical coordinates, which reduces the computational cost for the condensation.

Monophase and Symmetric Nonlinear Modes

From a historical point of view, monophase and symmetric nonlinear modes are of particular interest. This can be attributed to the first definition of nonlinear modes by Rosenberg (1960), which are by concept monophase motions (c.f. Definition 2.6). Moreover, the first method for the measurement of nonlinear modes, which has been proposed by Peeters et al. (2011)

is also limited to monophase motions. Therefore, it is noteworthy that the computational burden for this class of nonlinear modes can considerably be reduced in the proposed HBM framework by modifying the functional basis of the ansatz functions given in Eq. (3.10). For monophase motions a pure cosine (or sine) ansatz can be made yielding a modified function basis

$$\mathcal{F}_{\mathrm{mono}} = \left\{ \frac{1}{\sqrt{T}} c_0 \right\} \cup \left\{ \sqrt{\frac{2}{T}} c_n(t) | n \in \mathbb{N} \right\}, \tag{3.54}$$

which reduces the number of the unknowns in Eq. (3.33) from $N_{\mathrm{nl}}(2N_h + 1)$ to $N_{\mathrm{nl}}(N_h + 1)$. For symmetric motions, the function basis can be further reduced by the constant functions such that the number of the unknowns in Eq. (3.33) reduces to $N_{\mathrm{nl}}N_h$, i.e., the problem size is reduced to less than half of the original problem size.

Component Mode Synthesis and Mixed-Modal-Physical Formulation

The size of the problem in Eq. (3.33), which has to be solved to obtain a nonlinear modal motion, is governed by the number of nonlinear DOFs N_{nl}. However, the calculation of the reduced dynamic stiffness matrix (c.f. Eq. (3.32)) involves the calculation of an inverse matrix of which the size is determined by the number of linear DOFs $N_{\mathrm{ln}} = N - N_{\mathrm{nl}}$. For systems modeled with a large number of linear DOFs this may considerably slow down the calculation. It is common practice to reduce the number of DOFs of linear systems by the CMS method. There are different approaches for CMS, which are described, e.g., in the book of Craig and Kurdila (2006) and the review paper by Craig (2000). A particularly popular method for CMS is the method introduced by Craig and Bampton (1968), yielding a mixed-modal-physical representation of the system. For the Craig-Bampton (CB) reduction, the mass and stiffness matrices are partitioned in the form[5]

$$\begin{bmatrix} \mathbf{M}_{\mathrm{lnln}} & \mathbf{M}_{\mathrm{lnnl}} \\ \mathbf{M}_{\mathrm{lnnl}} & \mathbf{M}_{\mathrm{nlnl}} \end{bmatrix} \begin{bmatrix} \ddot{\boldsymbol{x}}_{\mathrm{ln}} \\ \ddot{\boldsymbol{x}}_{\mathrm{nl}} \end{bmatrix} + \begin{bmatrix} \mathbf{K}_{\mathrm{lnln}} & \mathbf{K}_{\mathrm{lnnl}} \\ \mathbf{K}_{\mathrm{lnnl}} & \mathbf{K}_{\mathrm{nlnl}} \end{bmatrix} \begin{bmatrix} \boldsymbol{x}_{\mathrm{ln}} \\ \boldsymbol{x}_{\mathrm{nl}} \end{bmatrix} = \begin{bmatrix} \mathbf{0} \\ \boldsymbol{g}_{\mathrm{nl}} \end{bmatrix}. \tag{3.55}$$

---

[5]It is assumed, for simplicity, that all interface DOFs are included in the set $\mathcal{I}$ of nonlinear DOFs and the free DOFs are the linear DOFs of the system.

Then the fixed interface modes of the linear DOFs can be calculated solving the linear eigenvalue problem

$$\left(-\omega_{0,\text{ln},i}^2 \mathbf{M}_{\text{lnln}} + \mathbf{K}_{\text{lnln}}\right) \boldsymbol{\phi}_{\text{ln},i} = \mathbf{0}, \tag{3.56}$$

where $\omega_{0,\text{ln},i}$ denotes the i-th eigenfrequency of the linear subsystem and $\boldsymbol{\phi}_{\text{ln},i}$ the corresponding eigenvector. In addition to these fixed interface modes, the CB reduction basis features the constraint modes

$$\boldsymbol{\Psi}_{\text{c}} = -\mathbf{K}_{\text{lnln}}^{-1} \mathbf{K}_{\text{lnnl}} \tag{3.57}$$

obtained by applying a unit displacement to the interface DOFs. The CB transformation can then be written as

$$\begin{bmatrix} \boldsymbol{x}_{\text{ln}} \\ \boldsymbol{x}_{\text{nl}} \end{bmatrix} = \begin{bmatrix} \boldsymbol{\Phi}_{\text{ln}} & \boldsymbol{\Psi}_{\text{c}} \\ \mathbf{0} & \mathbf{I}_{N_{\text{nl}}} \end{bmatrix} \begin{bmatrix} \boldsymbol{q}_{\text{ln}} \\ \boldsymbol{x}_{\text{nl}} \end{bmatrix} = \boldsymbol{\Theta} \begin{bmatrix} \boldsymbol{q}_{\text{ln}} \\ \boldsymbol{x}_{\text{nl}} \end{bmatrix}. \tag{3.58}$$

Herein, $\boldsymbol{q}_{\text{ln}}$ denotes the displacement of the linear DOFs in modal coordinates of the fixed interface modes. Typically, this CB transformation is used in combination with a truncation of the fixed interface modes such that the number of generalized coordinates is reduced. This can also be done in the context of nonlinear mode calculations, however, it is explained in the following that the mixed-modal-physical representation of the system improves the computational performance even in cases where no modal truncation is applied. Using the CB basis $\boldsymbol{\Theta}$ the mass and stiffness matrix can be calculated as

$$\mathbf{M}_{\text{CB}} = \boldsymbol{\Theta}^{\text{T}} \mathbf{M} \boldsymbol{\Theta} \tag{3.59}$$

and

$$\mathbf{K}_{\text{CB}} = \boldsymbol{\Theta}^{\text{T}} \mathbf{K} \boldsymbol{\Theta}. \tag{3.60}$$

The CB transformation matrix contains the fixed interface normal modes, i.e., the normal modes of the linear partition of the system. Thus, the transformation diagonalizes the linear partition of the mass and stiffness matrix. If mass normalized eigenvectors are used, then the linear partition of the mass matrix becomes

$$\mathbf{M}_{\text{CB,lnln}} = \mathbf{I}_{N_{\text{ln}}} \tag{3.61}$$

and the stiffness matrix becomes

$$\mathbf{K}_{\text{CB,lnln}} = \text{diag}\left\{\omega_{0,\text{ln},1}^2, ..., \omega_{0,\text{ln},N_{\text{ln}}}^2\right\}. \tag{3.62}$$

Therefore, the calculation of the inverse of the linear partition of the dynamic stiffness matrix in Eq. (3.32) becomes the trivial inversion of a diagonal matrix. Moreover, since the inverse can be calculated in closed form the calculation of the derivatives of the dynamic stiffness matrix (c.f. Appendix B) is also trivial. It is emphasized that this approach is different to the method proposed by Krack et al. (2013), who applied a spectral decomposition to the complete system to simplify the matrix inversion but solves the system in the physical domain. This approach has the drawbacks that a transformation back into the physical domain is necessary, which involves additional matrix multiplications and the inversion becomes impossible when the nonlinear modal frequency is equal to the linear modal frequency, which makes the spectral matrix singular. Both issues are avoided if the mixed-modal-physical formulation is used, such that it is worthwhile to solve the problem directly in mixed-modal-physical coordinates. Furthermore, it is highlighted that in many practical cases, in which large scale structures are considered, the original FE models are reduced anyway, such that a CB reduction basis may be at hand without additional computational effort. Finally, it is pointed out that the efficient condensation in mixed-modal-physical coordinates is not restricted to undamped systems but can also be generalized to systems with Caughey-type damping, for which the dynamic stiffness matrix becomes block diagonal. This generalization is necessary for frequency response calculations, the calculation of complex nonlinear modes or the calculation of nonlinear modes according to the extended periodic motion concept and is included for completeness in Appendix C.

3.3 Application Example: Truck with Nonlinear Elements

To demonstrate the applicability of the numerical algorithm, the application example of a truck with nonlinear elements is considered. The numerical results have been obtained in a feasibility study in cooperation with an industrial partner and are only briefly discussed for the purpose of demon-
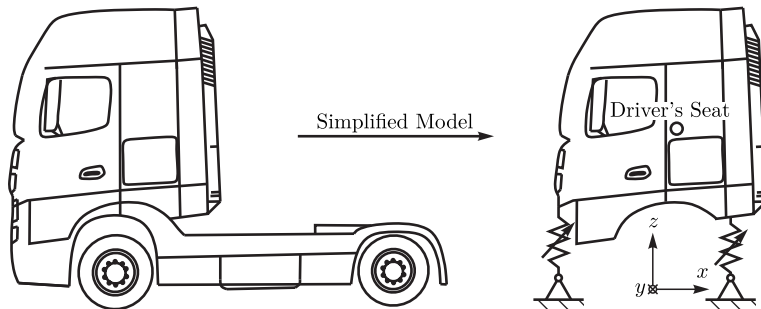
Figure 3.3: Sketch of the truck and the simplified model of the cabin.

stration[6]. In commercial vehicles numerous potential sources of nonlinear behavior can be found, e.g., bushing, bearing and damper elements in chassis parts or in interfaces between different parts of the vehicle assembly. In this demonstration example, the nonlinear elements in the connection between the driver's cabin and the remaining vehicle are studied with regard to their influence on the passenger comfort. Therefore, a truck is divided into two substructures, one consisting of the cabin including its frame and one consisting of the remaining parts of the vehicle. In the following, the model is simplified by removing the remaining vehicle and coupling the frame of the cabin to ground with nonlinear elements as shown in Fig. 3.3.

The numerical model of the cabin assembly consists of a FE model of the frame which is connecting the cabin to the remaining vehicle (see Fig. 3.4), and a rigid body model of the cabin itself. The structure is modeled in PERMAS to obtain the mass matrix and the linear stiffness matrix. For the passenger comfort analysis, a node is placed in the model at the position where the driver's seat is located as indicated in Fig. 3.3. The FE model, that features in total 154858 DOFs, is exported from PERMAS and imported in the MATLAB-based numerical code for the nonlinear analysis. For the nonlinear analysis, in total 14 nonlinear elements are considered, which are marked in Fig. 3.4 with black circles. These nonlinear elements include elements connecting the frame to ground (the remaining vehicle) and nonlinear connections between different parts of the frame assembly.

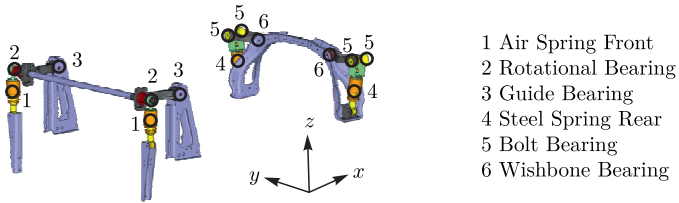[6]More details can be found in Huchler (2018).

Figure 3.4: Model of the frame connecting the cabin to the remaining vehicle.

Due to symmetry, the elements can be modeled with six different types of nonlinear elements each having six DOFs. The nonlinear force law for each DOF has been identified by curve fitting measured data of the respective element and DOF. For the curve fitting, polynomials up to quintic order are considered and all nonlinear forces are of stiffening type. More details on the used polynomial for the individual DOFs are included in Appendix D.

For the HBM calculation, the 154858 DOFs are partitioned into 150 interface DOFs, which include DOFs connected to nonlinear elements and the DOFs at the driver's seat, and 154708 linear DOFs. Then, the CB reduction is carried out and the linear DOFs are reduced to 200 fixed interface modes, which includes modes up to approximately 2 kHz. A number of 200 modes is regarded as sufficient, because the main concern with regard to passenger comfort are low frequency vibrations. Thus, the total number of DOFs of the considered model are $N = 350$ with $N_{\mathrm{nl}} = 150$ nonlinear DOFs.

Low frequency modes which mainly describe a rigid body motion of the cabin are of great importance for the passenger comfort. Therefore, these modes and the impact of the nonlinear elements on the nonlinear modal frequency and mode shape are analyzed here in more detail. The first three linear modes of the structure describe a pitch, roll and heave motion of the cabin. Modes four and five are local bending modes in the frame, which are not relevant for the passenger comfort. In contrast, modes six and seven are relevant yaw motions around two different centers of rotation and mode eight describes a rocking motion of the driver's cabin. A particularity of the test structure is the high modal density of around 15 modes in the frequency regime below 15 Hz. Therefore, in the nonlinear modal analysis, a large variety of nonlinear modal interactions and internal resonances can be observed.
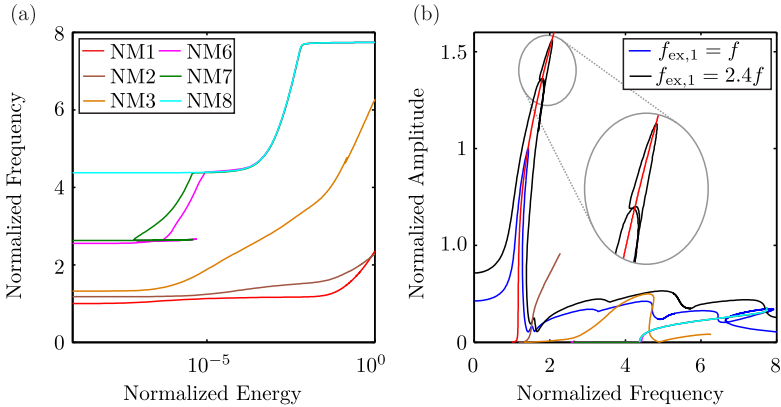
Figure 3.5: Frequency-energy plot of nonlinear modes one to three and six to eight (a) and drive point FRF for two different excitation levels for an excitation at the driver seat including backbone curves (b).

To reduce the complexity, the fundamental harmonic approximation of the frequency-energy plot of the nonlinear modes one to three and six to eight is shown Fig. 3.5(a). The frequency-energy plot shows that the frequencies of the first three modes are very close. Therefore, even a small shift in frequency due to nonlinear effects leads to modal coupling in a 1:1 internal resonance. To be more precise, it can be seen that the first mode, the pitch motion, couples with the second mode, the roll motion at $E_{\mathrm{kin}} \approx 10^{-5}$. For higher energies $E_{\mathrm{kin}} \approx 10^{-3}$ an additional coupling of the second with the third mode, representing a heave motion, can be observed. The yaw motions, nonlinear modes six and seven, are very similar in frequency and shape such that even small influence of the nonlinearity leads to a 1:1 internal resonance at $E_{\mathrm{kin}} \approx 10^{-6}$. The coupled mode then shows a strong stiffening behavior leading to an additional coupling to mode eight at $E_{\mathrm{kin}} \approx 10^{-5}$, such that for higher energies all three nonlinear modes merge to one nonlinear modal motion which is a combination of the two yaw motions and the rock motion. An additional modal coupling can be observed at $E_{\mathrm{kin}} \approx 10^{-1}$, where the third nonlinear mode couples with the combined mode six, seven and eight.

The frequency response for the forced and damped system for two different excitation levels is shown in Fig. 3.5(b) along with the backbone curves of modes one to three and six to eight. The FRF is calculated for sinusoidal excitation at the driver's seat in x-direction and the response at the same DOF is plotted. Rayleigh-damping is used for the FRF calculation[7]. It can be seen that the various internal resonances have a severe influence on the forced response. In particular, additional periodic solutions at the first resonance occur for the high excitation level (see magnification in Fig. 3.5(b)), which is caused by the 1:1 internal resonance of the first and second nonlinear mode. Moreover, the coupling effects between modes six to eight and the additional coupling with mode three leads to a nontrivial relation between the backbone curves of these modes and the forced response. This effect clearly shows that the backbone curve as defined in Definition 2.5 departs from the curve connecting maxima of the FRFs, which is often colloquially referred to as backbone curve. Another interesting effect, that can be observed in this frequency range, is that the maximum amplitudes are generally limited due to the effects of modal coupling. This can be attributed to the fact that the vibration energy is distributed among several modes.

The short digression to an industrial application example demonstrates the capability of the numerical algorithm to treat systems of industrial scale featuring very complex nonlinear modal dynamics. It is noted that the experimental identifications of structures of such complexity using NEMA is still remote. However, the study shows that the numerical analysis does not seem to be the limiting factor in this context. As a closing remark of the numerical study it is pointed out that numerical modal analysis can provide an interesting novel tool for the investigation of commercial vehicles. Especially, as it has been observed in this project that the effect of nonlinear modal interactions is pronounced in such vehicles, due to the high modal density. The positive effects of this modal coupling, such as the limited amplitudes in a wide frequency range, have probably been used for decades, but their design is rather based on experience than on rigorous analysis.

---

[7]A more detailed analysis of damping effects, including the effect of nonlinear damper elements, is omitted here for the sake of brevity.

3.4 Extension to Nonsmooth Nonlinearities

Nonsmooth nonlinearities due to contact and friction are of high practical relevance in many engineering structures. Therefore, the problem of extending the numerical method for nonlinear mode calculation of such systems is briefly outlined here. To be more precise, the extension to systems with unilateral frictionless constraints is discussed. A more comprehensive description of the numerical method, which is based on an extension of the algorithm for FRF calculation proposed by Schreyer and Leine (2016b) and Schreyer and Leine (2016a) is published in Peter et al. (2018b).

The modeling of contact interactions is the topic of numerous publications (Ibrahim, 2009). Three commonly used modeling approaches are shown in Fig. 3.6[8]. The contact can either be modeled by set-valued force laws or regularized by a finite contact stiffness. If a finite contact stiffness is used, then the problem of finding periodic solutions, i.e., also the problem of calculating nonlinear modes, can be solved with conventional algorithms such as the shooting method or the HBM derived above. In contrast, set-valued force laws lead to differential inclusions or measure differential inclusions which require special solution methods such as time-stepping algorithms (Leine and Nijmeijer, 2004). Such time-stepping methods can be included in shooting algorithms to find periodic solutions. It is shown by Schreyer and Leine (2016a) that it is possible to combine shooting methods with the HBM yielding the so-called Mixed Shooting HBM (MSHBM) to include nonsmooth contact dynamics in large scale multi-body or FE systems.

For systems with impacts, a common method for the modeling of the contact process is Newton's impact law. However, for FE models the impact law may become obsolete, as the impact process is sufficiently represented by internal waves propagating in the FE structure. Even worse, an impact coefficient $e \neq 0$ can lead to spurious high frequency vibration and numerical problems. Moreover, a coefficient $e \neq 1$ leads to energy dissipation, which is not admissible in the context of conservative nonlinear mode calculation.

The extension of the MSHBM algorithm by a mass redistribution proposed by Schreyer and Leine (2016b) for the purpose of FRF calculation of FE structures provides a remedy for both problems. The central idea is to

---

[8]The contact models are shown for a single frictionless contact and time dependence is omitted in the figure for the sake of clarity.

$$\mathbf{M}\ddot{\boldsymbol{x}} + \mathbf{K}\boldsymbol{x} + \mathbf{B}^{\mathrm{T}}\boldsymbol{\lambda} = \mathbf{0}$$

set valued contact law   contact stiffness

$$0 \leq u - z_0 \perp -\lambda \geq 0 \qquad\qquad \lambda = \begin{cases} g_{\mathrm{nl}} = k_0(u - z_0) & \text{for } u - z_0 \leq 0 \\ g_{\mathrm{nl}} = 0 & \text{for } u - z_0 \geq 0 \end{cases}$$

$\mathbf{M}(\dot{\boldsymbol{x}}^+ - \dot{\boldsymbol{x}}^-) + \mathbf{B}^{\mathrm{T}}\boldsymbol{\Lambda} = \mathbf{0}$

Newton law   massless boundary:

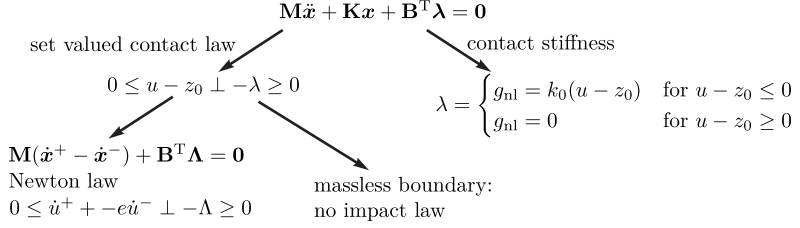$0 \leq \dot{u}^+ + -e\dot{u}^- \perp -\Lambda \geq 0$ no impact law

Figure 3.6: Overview of three different contact models, which can be included in nonlinear mode calculations.

make the contact nodes massless[9] yielding a modified version of Eq. (3.31):

$$\begin{bmatrix} \mathbf{M}_{\mathrm{lnln}} & \mathbf{0} \\ \mathbf{0} & \mathbf{0} \end{bmatrix} \begin{bmatrix} \ddot{\boldsymbol{x}}_{\mathrm{ln}}(t) \\ \ddot{\boldsymbol{x}}_{\mathrm{nl}}(t) \end{bmatrix} + \begin{bmatrix} \mathbf{K}_{\mathrm{lnln}} & \mathbf{K}_{\mathrm{lnnl}} \\ \mathbf{K}_{\mathrm{nlln}} & \mathbf{K}_{\mathrm{nlnl}} \end{bmatrix} \begin{bmatrix} \boldsymbol{x}_{\mathrm{ln}}(t) \\ \boldsymbol{x}_{\mathrm{nl}}(t) \end{bmatrix} + \begin{bmatrix} \mathbf{0} \\ \boldsymbol{\lambda}(t) \end{bmatrix} = \mathbf{0}. \quad (3.63)$$

It can be easily seen that the nonlinear partition of Eq. (3.63) reduces to a quasi-static problem. In addition, the impact equation

$$\mathbf{M}(\dot{\boldsymbol{x}}^+ - \dot{\boldsymbol{x}}^-) + \mathbf{B}^{\mathrm{T}}\boldsymbol{\Lambda} = \mathbf{0} \qquad\qquad (3.64)$$

becomes obsolete. Therefore, no time integration is required to calculate the nonlinear displacements in the time domain and the contact problem can be solved, e.g., using a linear complementary problem. Subsequently, compatibility between the Fourier transform of the nonlinear displacements in time domain and the nonlinear displacements in the frequency domain, i.e.,

$$\boldsymbol{x}_{\mathrm{nl}} \overset{!}{=} \mathrm{FFT}\left\{\boldsymbol{x}_{\mathrm{nl}}(t)\right\} \qquad\qquad (3.65)$$

is enforced to obtain the solution in the frequency domain.

Although the MSHBM originally has been proposed for FRF calculation, the method is particularly suitable for the calculation of nonlinear modes. Besides the numerical advantages, such as the general efficiency, the avoidance of spurious high frequency vibrations and the availability

---

[9]In the example included in this thesis the mass of the contact node is simply neglected. More sophisticated ways of mass redistribution are discussed, e.g., in Khenous et al. (2008).

of a semi-analytical Jacobian matrix, which are also reported in Schreyer and Leine (2016b), the method provides specific numerical advantages for the purpose of nonlinear mode calculation. First of all, the method is energy consistent such that it can be easily incorporated in numerical formulations for the calculation of conservative nonlinear modes according to Definition 2.1. Second, the filtering property, which is well-known for the conventional HBM is retained, such that internal resonances of minor influence can be neglected by choice of the ansatz functions. This is particularly interesting for systems with severe impact nonlinearities which typically encounter numerous internal resonances, making the nonlinear mode calculation cumbersome (Lee et al., 2009).

Finally, it is noted that the MSHBM with redistributed mass matrix does, unlike the Newton impact law or the contact stiffness method, not require any contact parameters. The contact behavior is fully included in the FE discretization allowing for a white-box modeling based on first principles.

3.5 Extension to Nonconservative Nonlinearities

There are two approaches with which the computation of nonlinear modes with the HBM can be easily extended to nonconservative systems. Although the numerical study of nonlinear modes of nonconservative systems is beyond the scope of this thesis, these approaches are briefly outlined here for the sake of completeness.

The first approach of Laxalde and Thouverez (2009) aims at approximating the nonperiodic response of free and damped systems. Therefore, the set $\mathcal{F}$ of basis functions Eq. (3.10) is modified by an exponential decay term. This modification can be regarded as a means of a decomposition of the motion into a slow time scale related to the exponential term representing the decay process and a fast time scale related to the trigonometric function representing the oscillatory behavior of the system. The method can be interpreted as a means of efficiently approximating the invariant manifold of the system (c.f. Definition 2.2). The approach has been applied by Laxalde et al. (2008) and Krack et al. (2013) to bladed disks of aircraft engines with frictional contact. For the purpose of system identification it is conceivable to combine the numerical method with a resonance decay measurement technique.

The second approach by Krack (2015) is based on the extended periodic motion concept for nonconservative systems (c.f. Definition 2.3). Since the ENMs are periodic by definition, the extension of the numerical algorithm for this purpose is straightforward. In the context of system identification this numerical approach can be combined with steady-state measurements as is shown in Scheel et al. (2018b).

3.6 Summary

The numerical calculation of nonlinear modes for the purpose of modal based nonlinear system identification is discussed. In particular, the following aspects of numerical modal analysis are covered:

- An analytical HBM algorithm which is suitable for this purpose with regard to efficiency, robustness and generality is proposed.

- The potential of the proposed numerical algorithm for nonlinear modal analysis of industrial scale structures is demonstrated at the example of a high fidelity model of a truck cabin.

- The extension of the numerical method to nonsmooth systems with the MSHBM is explained and the treatment of nonlinearly damped systems is briefly discussed.

Chapter 4

Experimental Extraction of Nonlinear Modes

In this chapter, the experimental extraction of nonlinear modal characteristics, i.e., NEMA, is discussed. The chapter starts in Section 4.1 with a brief introduction to current methods for NEMA and a summary of their shortcomings. Special emphasis is put on the phase resonance approach, which forms the foundation of the developments in this thesis. Subsequently, in Section 4.2, a new framework for the robust NEMA is proposed. The method is illustrated at a realistic numerical example in Section 4.3. The generalization of the method to systems with nonsmooth and damping nonlinearities is discussed in Sections 4.4 and 4.5, respectively. The contributions of the thesis in the field of NEMA are summarized in Section 4.6.

4.1 Introduction to Nonlinear Experimental Modal Analysis

The experimental extraction of nonlinear modal parameters is a comparatively new area of research (c.f. Section 1.3). While the direct extension of linear EMA methods to nonlinear systems is strictly limited to systems with weak nonlinearities, the concept of nonlinear modes provides a rigorous theoretical framework for the treatment of arbitrary nonlinear systems. The sound theoretical basis and clear physical meaning, as opposed to empirical mode decomposition or proper orthogonal modes, motivates the use of the concept of nonlinear modes in this thesis.

The first approach for the measurement of nonlinear modes, proposed by Peeters et al. (2011), attempts to isolate a single nonlinear mode at a time. The method is conceptually related to phase resonance testing of linear systems and is therefore referred to as *nonlinear phase resonance testing*. A different approach for the extraction of nonlinear modes is pursued by

Noël et al. (2016), who derives a nonlinear state-space model with NSID methods and subsequently calculates the nonlinear modes of this state-space model using a shooting method. The advantage of this method is that theoretically several modes can be extracted at a time with an excitation that is easy to implement experimentally. However, the method requires additional numerical effort and the accuracy may be limited by the derived state-space model. A detailed comparative study of a NSID approach and a nonlinear phase resonance approach by Scheel et al. (2018a) concludes that both methods have their specific advantages and drawbacks depending on the system under investigation and the purpose of the derived model. In this thesis, a phase resonance approach is pursued, which is the only approach to directly measure nonlinear modes. Moreover, the method provides a high confidence model for the prediction of steady-state vibrations, which is deemed highly relevant in practice. Therefore, the general methodology for nonlinear phase resonance testing is introduced in the following.

4.1.1 Nonlinear Phase Resonance Testing

Phase resonance testing, for linear as well as nonlinear systems, aims at exciting a damped structure such that a modal motion of the underlying conservative structure is imitated. In the linear case, where the phase resonance method is mostly used for the extraction of close or strongly coupled modes or in cases where the modal parameters need to be estimated with the highest possible confidence, the appropriate force vector for the isolation of the normal mode motion can often be estimated a priori based on FRF matrices to minimize the tuning effort during experimentation (Wright et al., 1999). In the nonlinear case, however, the energy dependence of the nonlinear modes and the lack of the superposition principle complicates an a priori estimation. Therefore, the force vector for the isolation of a nonlinear modal motion has to be found through successive appropriation during the experiment. The properties of the force which is theoretically required for this purpose have been derived by Peeters et al. (2011) and are briefly reviewed in the following.

Consider the equation of motion of a damped and excited mechanical system with a conservative nonlinearity

$$\mathbf{M}\ddot{\boldsymbol{x}}(t) + \mathbf{D}\dot{\boldsymbol{x}}(t) + \mathbf{K}\boldsymbol{x}(t) + \boldsymbol{f}_{\mathrm{nl}}(\boldsymbol{x}(t)) = \boldsymbol{f}_{\mathrm{ex}}(t), \tag{4.1}$$

where $\mathbf{M} = \mathbf{M}^{\mathrm{T}} \in \mathbb{R}^{N \times N}$ denotes the mass matrix, $\mathbf{K} = \mathbf{K}^{\mathrm{T}} \in \mathbb{R}^{N \times N}$ the linear stiffness matrix, $\boldsymbol{x}(t) \in \mathbb{R}^N$ represents the vector of generalized coordinates and $\boldsymbol{f}_{\mathrm{ex}}(t)$ the vector of excitation forces. The vector $\boldsymbol{f}_{\mathrm{nl}}(\boldsymbol{x}(t)) \in \mathbb{R}^N$ represents the nonlinear restoring forces and the matrix $\mathbf{D} \in \mathbb{R}^{N \times N}$ typically viscous damping effects with some spatial distribution. If it is desired to enforce a nonlinear modal motion according to Definition 2.1, the motion of the system described by Eq. (4.1) must also satisfy the equation of motion of the underlying conservative system, i.e.,

$$\mathbf{M}\ddot{\boldsymbol{x}}(t) + \mathbf{K}\boldsymbol{x}(t) + \boldsymbol{f}_{\mathrm{nl}}(\boldsymbol{x}(t)) = \mathbf{0}. \tag{4.2}$$

Comparison of Eq. (4.1) and Eq. (4.2) yields the condition

$$\mathbf{D}\dot{\boldsymbol{x}}(t) = \boldsymbol{f}_{\mathrm{ex}}(t) \ \forall t, \tag{4.3}$$

which has to be satisfied to isolate a nonlinear modal motion. The nonlinear modal motion is by definition periodic (c.f. Definition 2.1) and can thus be represented by a Fourier series

$$\boldsymbol{x}(t) = \sum_{n=-\infty}^{\infty} \underline{\boldsymbol{x}}_n \mathrm{e}^{\mathrm{i}n\omega t}, \tag{4.4}$$

where $\underline{\boldsymbol{x}}_n$ denotes the vector of complex Fourier coefficients of the n-th harmonic. The excitation forces can be represented by a Fourier series with the same fundamental frequency as

$$\boldsymbol{f}_{\mathrm{ex}}(t) = \sum_{n=-\infty}^{\infty} \underline{\boldsymbol{f}}_{\mathrm{ex},n} \mathrm{e}^{\mathrm{i}n\omega t}, \tag{4.5}$$

with the vector of complex Fourier coefficients $\underline{\boldsymbol{f}}_{\mathrm{ex},n}$. Then, the condition in Eq. (4.3) can be rewritten in the frequency domain as

$$\mathrm{i}n\omega\mathbf{D}\underline{\boldsymbol{x}}_n = \underline{\boldsymbol{f}}_{\mathrm{ex},n} \ \forall n. \tag{4.6}$$

In the case of a monophase motion, this means that the excitation has to be shifted by $\pi/2$ in phase with respect to the response for all generalized coordinates and harmonics (c.f. Peeters et al. (2011)).

Practical Realization

The phase criterion derived above is difficult to realize in practice, because the condition has to be fulfilled for every point on the structure and all frequencies included in the response. However, several experimental studies have shown that in the case of light damping and the absence of internal resonances a single point single harmonic force is sufficient to approximately isolate the nonlinear modal motion (Londono et al., 2015; Peeters et al., 2010; Zapico-Valle et al., 2013). The current practice is to manually adjust the phase of the single harmonic force by tuning the excitation frequency, as illustrated in Fig. 4.1(b), at a constant forcing amplitude. To extract a branch of nonlinear modes, this procedure has to be repeated for several excitation levels. To minimize the tuning effort, typically the excitation is only appropriated for a single high excitation level. Then, the excitation is switched off and the free-decay is analyzed using TFA. The underlying assumption is, that the nonlinear modal motion which is enforced by the appropriated excitation corresponds to an initial condition on or near an invariant manifold of the damped system. In the case of light damping it is further assumed that the motion on the invariant manifold of the damped system closely resembles the nonlinear modal motion of the undamped system. Due to the invariance property the motion is confined to the invariant manifold during the decay process, such that the motion on the invariant manifold can be analyzed to obtain nonlinear modal motions for different energy levels. The procedure is summarized in Fig. 4.1(a) and illustrated in the frequency-amplitude space in Fig. 4.1(b).

Modal Purity Index

To assess the quality of the mode appropriation, Peeters et al. (2011) propose a mode indicator function which will be referred to as Modal Purity Index (MPI)[1] in the following. In the case of a monophase motion all harmonics of the excitation force can be shifted in phase such that they can be represented by a purely sinusoidal signal with the respective frequency. If the response is shifted in phase by $\pi/2$ with respect to the excitation, this means that the response is purely cosine shaped. In complex notation,

---

[1]The notion MPI is used to distinguish this measure from the mode indicator function proposed in Section 4.2.

(a)

1. Manual tuning of
excitation frequency

2. Switching off
the excitation

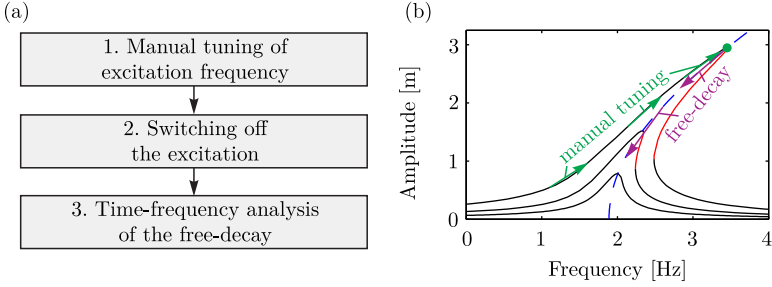3. Time-frequency analysis
of the free-decay

(b)

Figure 4.1: Current procedure for nonlinear phase resonance testing (a) and illustration of the method in frequency-amplitude space (b).

the modal purity index can then be defined for every harmonic as

$$\Delta_n = \frac{\mathrm{Re}\left\{\underline{\bar{x}}_n^{\mathrm{T}}\right\}\mathrm{Re}\left\{\underline{x}_n\right\}}{\underline{\bar{x}}_n^{\mathrm{T}}\underline{x}_n}, \tag{4.7}$$

where $\underline{\bar{x}}_n$ denotes the complex conjugate of the complex Fourier coefficient $\underline{x}_n$. Accordingly, $\underline{\bar{x}}_n^{\mathrm{T}}$ denotes the Hermitian $\underline{x}_n^{\mathrm{H}}$. This purely response based indicator for the force appropriation quality yields a value of unity in the case of perfect appropriation of the respective harmonic. To assess the global mode isolation, the arithmetic mean of all considered harmonics N_h is used yielding

$$\Delta = \frac{1}{N_h}\sum_{n=1}^{N_h}\Delta_n. \tag{4.8}$$

as MPI.

4.1.2 Shortcomings of the Current Practice

Nonlinear phase resonance testing is generally a versatile tool for the extraction of nonlinear modal parameters. Theoretically, the nonlinear modal parameters of complex systems with close and coupled modes or internal resonances can be extracted. However, it is expected that the extraction

of nonlinear modes of such systems requires considerable experimental effort, particularly, to realize an appropriate forcing. Since the development of nonlinear phase resonance testing is still in its infancy, even for the systems of limited complexity to which it has been applied so far, several practical problems arise. Many of these problems are related to the current *experimental procedure* summarized in Fig. 4.1(a):

1. *Manual tuning of the excitation frequency:*
   The manual tuning of the excitation is time consuming. For weakly damped systems, a small frequency difference around resonance causes a strong change in amplitude and phase, such that the frequency increment during the tuning process has to be very small. Moreover, there are systems, such as the Duffing-type example in Fig. 4.1(b), where bifurcation points occur in the vicinity of the backbone curve. Even small disturbances during experimentation may cause a premature transition to another stable attractor such that the tuning procedure has to be restarted.

2. *Switching off the excitation:*
   The instantaneous removal of the excitation to initiate the free-decay process is generally only possible if non-contact excitation techniques are used, e.g., electromagnetic excitation. For commonly used shaker excitation, the switching off is likely to disturb the initial condition, which is supposed to be on the invariant manifold. Additionally, the shape of the invariant manifold is affected when the passive shaker remains connected to the structure during decay.

3. *TFA of the free-decay:*
   The hypothesis that the invariant manifold of the damped system during decay resembles the nonlinear mode of the conservative system does only hold in the case of weak damping. It is not clear how the nonlinear modal parameters are biased through transient effects. Furthermore, accurate TFA requires sophisticated signal processing. Particularly, for systems with a fast decay, the resolution of the obtained backbone curve is limited by the TFA.

Additional practical difficulties are related to the estimation of the *mode isolation quality*. The phase condition and the MPI is, by concept, limited to the case of monophase motions. Both conditions can only be evaluated for the stationary state at which the force is appropriated. The mode

isolation quality during free-decay is not clear. For cases when the MPI can be used, it strongly depends on the number of frequencies considered, such that the MPI cannot be regarded as a conclusive quality indicator (Ehrhardt and Allen, 2016).

All current studies of nonlinear phase resonance testing are limited to systems with smooth nonlinearities and it is not yet clear whether the method can be extended to systems with nonsmooth nonlinearities such as unilateral constraints inducing impacts. It is expected that the strongly nonlinear behavior caused by nonsmooth nonlinearities considerably complicates the manual tuning of the excitation. Furthermore, strong and sudden changes in vibration behavior occur, which are difficult to resolve using TFA of the free-decay.

Besides the practical problems related to the current approach there are a number of conceptual questions related to nonlinear phase resonance testing that have not been addressed to a satisfying extent so far. Even though some amplitude dependent parameters, such as deflection shapes or modal frequencies can be extracted, the definition of nonlinear modal parameters is ambiguous. Particularly, the consistency of the derived parameters to linear theory has not been addressed yet and their significance is not clear. To be more precise, it has not yet been demonstrated if and how experimentally extracted parameters are meaningful for the derivation of predictive models.

Further issues are related to the damping behavior of the structure. Firstly, current methods are limited to structures featuring weak proportional damping and it is not clear how these methods can be generalized to structures with stronger, potentially nonlinear damping. Secondly, even for weakly damped structures, the current approach lacks a method for the quantification of the damping.

The above mentioned limitations of current nonlinear phase resonance approaches are addressed in the following. However, it is acknowledged at this point that there are further limitations, such as the measurement of internal resonant structures or the use of muli-point excitation techniques, which are considered beyond the scope of this thesis. A more detailed discussion of these limitations is included in Section 7.2.

4.2 A New Framework for Robust Nonlinear Experimental Modal Analysis

In this section, a framework for a robust NEMA is proposed, addressing the shortcomings of previous approaches. The section starts with a generalization of the phase condition to non-monophase motions and the derivation of a power based theoretical framework for NEMA. A power based mode indicator function (PBMIF) is presented which can be used to assess the mode isolation quality. Subsequently, the practical realization of the appropriate excitation and the reliable tuning of the excitation force are addressed. Therefore, the concept of Phase-Locked-Loops (PLLs) is introduced and its application in NEMA is explained. Then, the attention is drawn to the extraction of nonlinear modal parameters. Special emphasis is put on the consistency of the nonlinear modal parameters with linear theory, which plays a significant role for the application of the derived nonlinear modal model (c.f. Chapter 5). Furthermore, the extraction of a nonlinear modal damping measure is discussed.

4.2.1 Generalization of the Phase Condition

The theoretical foundation for nonlinear phase resonance testing is so far limited to monophase nonlinear modes. However, the concept can be easily extended to non-monophase situations by a change of coordinates. Therefore, the system described by Eq. (4.2) is written in linear modal coordinates $\boldsymbol{x}(t) = \boldsymbol{\Phi}\boldsymbol{q}(t)$ yielding

$$\mathbf{I}_N \ddot{\boldsymbol{q}}(t) + \boldsymbol{\Omega}_0 \boldsymbol{q}(t) + \boldsymbol{f}_{\text{nlm}}(\boldsymbol{q}(t)) = \boldsymbol{0}. \tag{4.9}$$

with

$$\begin{aligned}
\mathbf{I}_N &= \boldsymbol{\Phi}^{\mathrm{T}}\mathbf{M}\boldsymbol{\Phi}, \\
\boldsymbol{\Omega}_0 &= \boldsymbol{\Phi}^{\mathrm{T}}\mathbf{K}\boldsymbol{\Phi} = \text{diag}\left\{\omega_{0,i}^2\right\} \ \text{for } i = 1,...N, \\
\boldsymbol{f}_{\text{nlm}}(\boldsymbol{q}(t)) &= \boldsymbol{\Phi}^{\mathrm{T}}\boldsymbol{f}_{\text{nl}}(\boldsymbol{\Phi}\boldsymbol{q}(t)).
\end{aligned} \tag{4.10}$$

Analogously to the derivation by Peeters et al. (2011) described in Section 4.1, the displacements in modal coordinates can be developed in a

Fourier series as

$$q(t) = \sum_{n=-\infty}^{\infty} \underline{q}_n \mathrm{e}^{\mathrm{i}n\omega t}, \tag{4.11}$$

yielding a representation of the equation of motion in the frequency domain

$$\left(-n^2\omega^2 \mathbf{I}_N + \mathbf{\Omega}_0\right)\underline{q}_n + \underline{f}_{\mathrm{nlm},n} = \mathbf{0} \quad \forall n, \tag{4.12}$$

where $\underline{f}_{\mathrm{nlm},n}$ is the Fourier coefficient of the n-th harmonic of the nonlinear force in modal coordinates. Since the equations are uncoupled in the linear terms, it can be easily seen that the phase of the inertia forces in the i-th linear modal coordinate and the n-th harmonic,

$$\underline{f}_{i,n}^{\mathrm{M}} = -n^2\omega^2 \underline{q}_{i,n}, \tag{4.13}$$

and the linear restoring forces in the i-th linear modal coordinate and the n-th harmonic,

$$\underline{f}_{i,n}^{\mathrm{K}} = \omega_{0,i}^2 \underline{q}_{i,n}, \tag{4.14}$$

is determined by the phase of the coefficient $\underline{q}_{i,n}$. In the complex plane, this can be illustrated using a pointer diagram as in Fig. 4.2(a). The phase of the Fourier coefficient of the i-th component of the nonlinear restoring force in modal coordinates $\underline{f}_{i,n}^{\mathrm{nlm}}$ can be determined from the dynamic equilibrium condition, which must be fulfilled for a periodic motion, yielding that the pointer of the nonlinear restoring force must be collinear to the linear restoring forces and the inertia forces, respectively.

In the following, the damped and excited system (c.f. Eq. (4.1)) is considered for comparison. If the damping matrix is of Caughey-type (Caughey, 1960), i.e.,

$$\mathbf{\Phi}^{\mathrm{T}}\mathbf{D}\mathbf{\Phi} = \mathrm{diag}\left\{d_i\right\} \text{ for } i = 1, ...N, \tag{4.15}$$

then no additional coupling is induced by the damping. Thus, the damping forces in the i-th linear modal coordinate

$$\underline{f}_{i,n}^{\mathrm{D}} = \mathrm{i}n d_i \underline{q}_{i,n} \tag{4.16}$$
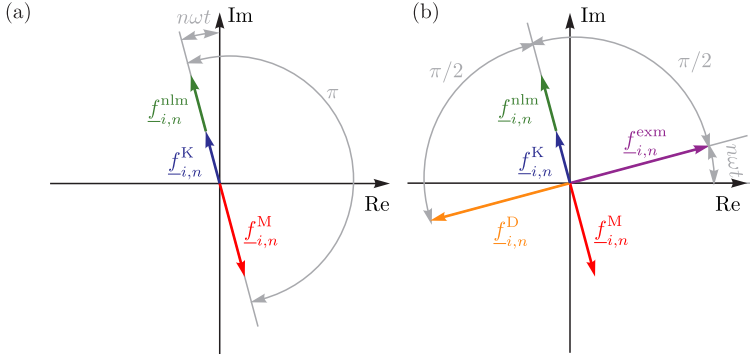
Figure 4.2: Pointer diagram in linear modal coordinates for a nonlinear mode (a) and for a forced and damped system in nonlinear modal motion (b).

are shifted in phase by $\pi/2$ with respect to the forces of the conservative system in nonlinear modal motion, due to the multiplication with the imaginary unit i. Therefore, the excitation of a nonlinear modal motion requires an excitation force $\underline{f}_{i,n}^{\mathrm{exm}}$ in the i-th modal coordinate and the n-th harmonic which is also shifted in phase by $\pi/2$ with respect to the forces in the conservative system and has the same magnitude but opposite sign as the damping forces. The dynamic equilibrium for the forced and damped system in nonlinear modal motion is visualized in the pointer diagram in Fig. 4.2(b). It can be seen that, for the isolation of general nonlinear modal motions of systems with damping properties that can be modeled by Caughey-type damping, the excitation has to fulfill the same phase criterion as in the monophase case, however, in modal coordinates. Analogously to the monophase case, where the phase criterion has to be met for all physical coordinates and all harmonics, in the general case the condition has to be fulfilled for all linear modal coordinates and all harmonics.

Despite the similarities of the monophase case investigated by Peeters et al. (2011) and the generalized case presented here, two notable differences are pointed out:

- In the general case, the phase of the individual harmonics and the individual (modal) coordinates may be different, whereas this is excluded by the concept of monophase motion.

- In the monophase case, the phase of the excitation force can directly be evaluated in the physical coordinates, which is not possible in the general case.

Although particularly the second point complicates the use of the general phase criterion for the tuning of the excitation force during experimentation, the concept allows for a posteriori estimation of the mode isolation quality also in the non-monophase case, e.g., by evaluation of the MPI in modal domain. However, a more practical approach based on power quantities borrowed from electrical engineering is pursued in the following.

4.2.2 Power Quantities in Nonlinear Phase Resonance Testing

A central quantity in the suggested framework for NEMA is the mechanical power of the excitation forces acting on the system. The body of the derivations made here has been published in Peter and Leine (2017). The analysis of power quantities, which is proposed in the first part of this section, is inspired by the power definitions in electrical engineering. To be more precise, power quantities in nonlinear electrical systems, as originally defined by Budeanu (1927), form the basis of the derivations. Furthermore, the analysis can be viewed as an extension of the so-called reactive power method which is used in linear phase resonance testing (Géradin and Rixen, 2015). In this context, the second part of the section discusses the mechanical interpretation and the meaning of power quantities in nonlinear modal testing.

Introduction to Power Theory

Consider the instantaneous mechanical power of an excitation force

$$p(t) = \boldsymbol{f}_{\mathrm{ex}}(t)^{\mathrm{T}} \dot{\boldsymbol{x}}(t), \tag{4.17}$$

where $\boldsymbol{f}_{\mathrm{ex}}(t)$ is a generalized force in $\mathbb{R}^N$. The excitation force acts on the structure at N_j physical points with the generalized force directions

$\boldsymbol{w}_j \in \mathbb{R}^N$ with $j = 1...N_j$ yielding

$$\boldsymbol{f}_{\text{ex}}(t) = \sum_{j=1}^{N_j} \boldsymbol{w}_j \lambda_j(t), \tag{4.18}$$

where $\lambda_j(t)$ denotes the local scalar forces contributing to the generalized force $\boldsymbol{f}_{\text{ex}}(t)$. The excitation power in Eq. (4.17) can be rewritten in terms of the local forces as

$$p(t) = \sum_{j=1}^{N_j} \lambda_j(t) \boldsymbol{w}_j^{\text{T}} \dot{\boldsymbol{x}}(t) = \sum_{j=1}^{N_j} \lambda_j(t) \chi_j(t) = \sum_{j=1}^{N_j} p_j(t), \tag{4.19}$$

with the local velocities $\chi_j(t) = \boldsymbol{w}_j^{\text{T}} \dot{\boldsymbol{x}}(t)$ and the instantaneous power $p_j(t)$ at the j-th excitation location. Under the assumption that the excitation forces and the velocity are periodic with some fundamental frequency ω, both quantities can be represented by Fourier series yielding

$$p_j(t) = \sum_{n=-\infty}^{\infty} \underline{\lambda}_{j,n} e^{\text{i}n\omega t} \sum_{n=-\infty}^{\infty} \underline{\chi}_{j,n} e^{\text{i}n\omega t}, \tag{4.20}$$

where n denotes the harmonic index. For the Fourier coefficients, it holds that $\underline{\lambda}_{j,n} = \bar{\underline{\lambda}}_{j,-n}$ and $\underline{\chi}_{j,n} = \bar{\underline{\chi}}_{j,-n}$, as the quantities $\lambda_j(t)$ and $\chi_j(t)$ are real. The product of Fourier series in Eq. (4.20) can be split into a time constant part and an oscillating part. In analogy to electrical engineering the time constant part

$$P_j = \sum_{n=-\infty}^{\infty} \underline{\lambda}_{j,n} \bar{\underline{\chi}}_{j,n} = \sum_{n=-\infty}^{\infty} |\underline{\lambda}_{j,n}||\bar{\underline{\chi}}_{j,n}| e^{\text{i}(\gamma_{j,n} - \vartheta_{j,n})} \tag{4.21}$$

is referred to as *active power*. Herein, the angles $\gamma_{j,n}$ and $\vartheta_{j,n}$ denote the phase angle of the n-th harmonic of the velocity and the force, respectively. The operator $|.|$ indicates the magnitude of the complex coefficients. As the magnitude of the complex coefficients is equal to the magnitude of their complex conjugate coefficients and the mean value of the velocity is zero,

i.e., $|\underline{\chi}_{j,0}| = 0$, Eq. (4.21) can be rearranged yielding

$$
\begin{aligned}
P_j &= \sum_{n=1}^{\infty} |\underline{\lambda}_{j,n}||\underline{\chi}_{j,n}|(e^{\mathrm{i}(\gamma_{j,n}-\vartheta_{j,n})} + e^{\mathrm{i}(-\gamma_{j,n}+\vartheta_{j,n})}) \\
&= \sum_{n=1}^{\infty} |\underline{\lambda}_{j,n}||\underline{\chi}_{j,n}|(e^{-\mathrm{i}\varphi_{j,n}} + e^{\mathrm{i}\varphi_{j,n}}),
\end{aligned}
\tag{4.22}
$$

where $\varphi_{j,n} = \gamma_{j,n} - \vartheta_{j,n}$. The sum can be rewritten using Euler's formula yielding

$$
P_j = \sum_{n=1}^{\infty} 2|\underline{\lambda}_{j,n}||\underline{\chi}_{j,n}| \cos(\varphi_{j,n}) = \sum_{n=1}^{\infty} F_{j,n} V_{j,n} \cos(\varphi_{j,n}),
\tag{4.23}
$$

with the effective values of the n-th harmonic of the force $F_{j,n} = \sqrt{2}|\underline{\lambda}_{j,n}|$ and the velocity $V_{j,n} = \sqrt{2}|\underline{\chi}_{j,n}|$ at the j-th excitation location.

The active power P_j can be interpreted as the mean value of the mechanical power brought into the system by the excitation over one period. In accordance to Budeanu (1927), the *reactive power* of the excitation forces is defined as

$$
Q_j = \sum_{n=1}^{\infty} F_{j,n} V_{j,n} \sin(\varphi_{j,n}).
\tag{4.24}
$$

In contrast to the active power, this power quantity lacks a clear physical meaning and is based on a rigorous extention of linear theory[2]. Furthermore, the *apparent power* can be defined as

$$
S_j = F_{\mathrm{RMS}} V_{\mathrm{RMS}} = \sqrt{\sum_{n=1}^{\infty} F_{j,n}^2} \sqrt{\sum_{n=1}^{\infty} V_{j,n}^2},
\tag{4.25}
$$

i.e., the product of the total root mean square values of the force and the velocity respectively. The power triangular relation well known from linear

---

[2]For a detailed discussion the reader is referred to Peter and Leine (2017).

systems becomes an inequality[3], i.e.,

$$S_j^2 \geq P_j^2 + Q_j^2, \tag{4.26}$$

which means that the apparent power cannot be calculated solely based on the active and reactive power components. However, a power triangular relation for nonlinear systems can be obtained by the introduction of a *distortion power* component $D_j = \sqrt{S_j^2 - P_j^2 - Q_j^2}$, which includes all parts of the apparent power in Eq. (4.25) which are not covered by the active and reactive power yielding

$$S_j = \sqrt{P_j^2 + Q_j^2 + D_j^2}. \tag{4.27}$$

Power Quantities in Nonlinear Modal Testing

The significance of the above derived power quantities in NEMA is, similarly to the generalization of the phase criterion in Section 4.2.1, illustrated by pointer diagrams in Fig. 4.3. The pointer diagrams are used to show the properties of the powers induced by the dynamic forces in the system. Similarly to the generalization of the phase criterion, the pointer diagrams are shown in modal coordinates, which simplifies the phase relation between dynamic forces and velocities. However, it should be noted that the mechanical power is a scalar quantity which can be evaluated either in physical or modal domain, i.e.,

$$p(t) = \boldsymbol{f}_{\mathrm{ex}}(t)^{\mathrm{T}} \dot{\boldsymbol{x}}(t) = \boldsymbol{f}_{\mathrm{exm}}(t)^{\mathrm{T}} \dot{\boldsymbol{q}}(t), \tag{4.28}$$

such that the derivation in physical coordinates yields an equivalent result, although the phase relations are not obvious for the individual DOFs.

The dynamic forces at a representative modal DOF i are depicted as pointers along with the pointer of the modal velocity $\underline{v}_{i,n} = \mathrm{i}n\underline{q}_{i,n}$ for a representative harmonic n. Moreover, the complex conjugate pointers of the force and velocity for the same harmonic are shown as these are relevant for the derivation of the power quantities. The phase angle between the modal excitation force $\underline{f}_{i,n}^{\mathrm{exm}}$ and the velocity of the n-th harmonic is denoted by $\varphi_{i,n}^{\mathrm{m}}$.

The excitation forces are considered in diagram (a), the inertia forces $\underline{f}_{i,n}^{\mathrm{M}}$ in diagram (b), the conservative restoring forces $\underline{f}_{i,n}^{\mathrm{C}}$, including linear

---

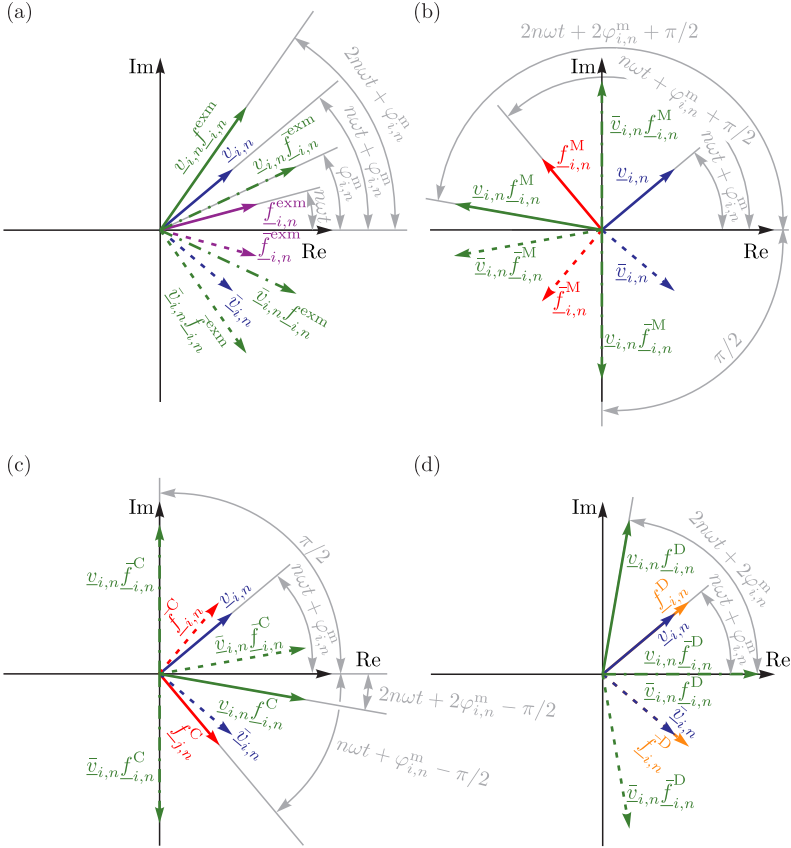[3]A proof of this inequality is provided in Appendix E.

Figure 4.3: Pointer diagram for excitation power (a), power of inertia forces (b), power of conservative restoring forces (c) and damping forces (d).

and nonlinear components, in diagram (c) and the damping forces $\underline{f}^{\mathrm{D}}_{i,n}$ in diagram (d). The power of each of the forces can be calculated as the inner product of the force and the velocity. Hence, the multiplication yields two pairs of complex conjugate power components, one of which has

a constant phase angle and one of which rotates with $2n\omega$. In the case of a dynamic equilibrium all pointers compensate one another resulting in a steady-state motion. In the case of a nonlinear modal motion the damping and excitation forces are zero and the inertia and conservative restoring forces compensate one another. It can be seen that this holds for the rotating pointers as well as for the pointers with constant phase angle. The pointers with constant phase angle are associated with the power quantities derived above. The n-th component of the active power of a force is defined as the real part of the constant pointer, whereas the reactive power represents the imaginary part. It can be seen in diagrams (b) and (c) that the inertia and conservative restoring forces only have a reactive power component. The damping forces in diagram (d), however, solely contribute to the active power. The only force which can have an active and reactive power component, dependent on the phase angle $\varphi_{i,n}^{\mathrm{m}}$ is the excitation force. If it is now desired that the excitation force balances out the damping force without affecting the dynamic equilibrium of the conservative restoring and inertia forces, then the phase angle $\varphi_{i,n}^{\mathrm{m}}$ has to be chosen such that the excitation force only contributes to the active power, i.e., $\varphi_{i,n}^{\mathrm{m}} = \pi$. In this case also the oscillating pointers are in balance. Note that this criterion is in line with the generalized phase condition derived in Section 4.2.1.

The requirement that the excitation force must only contribute to the active power holds for all harmonics and all modal coordinates to which an excitation is applied. If the condition holds and the pointers are in balance for all modal coordinates and harmonics, then no power is transferred to different harmonics or modal coordinates. The damping forces for modal coordinates or harmonics where no excitation is applied theoretically have to be zero. If this is not the case, additional power has to be introduced at the excited coordinates to ensure overall power balance for the structure which affects the local power balance at the excited modal coordinates. As a consequence, the distortion or reactive power of the excitation would not be zero. Therefore, the quality of the nonlinear mode isolation can be evaluated by investigation of the excitation power properties. Finally, it is noted that, although this has been evaluated here in the modal domain, the same requirements are met in the physical domain because the power is a scalar quantity. Of course, the evaluation in the physical coordinates is more suitable in experimental reality.

Power Based Mode Indicator Function

The power considerations derived above can be used to define a PBMIF for the practical evaluation of the mode isolation quality. Therefore, a representative excitation point j is considered. As derived above the force must only contribute to the active power such that the reactive power vanishes, i.e.,

$$Q_j = \sum_{n=1}^{\infty} F_{j,n} V_{j,n} \sin(\varphi_{j,n}) = 0. \tag{4.29}$$

Additionally, the magnitudes of the excitation force must be equal to the damping force such that the distortion power vanishes, i.e.,

$$D_j = 0. \tag{4.30}$$

The nonlinear power triangular relation then yields

$$S_j = |P_j|. \tag{4.31}$$

Note that the active power (see Eq. (4.23)) has a sign depending on the angles $\varphi_{j,n}$, whereas the apparent power is positive by definition (see Eq. (4.27)). In the vicinity of a mode, the sign of the active power as defined above is negative:

$$\varphi_{j,n} \approx \pi \quad \forall n \quad \Rightarrow \quad \cos(\varphi_{j,n}) < 0. \tag{4.32}$$

Therefore, the relation

$$\Lambda_j := -\frac{P_j}{S_j} \in [-1, 1] \tag{4.33}$$

can be used to estimate the quality of the excitation for nonlinear mode isolation. This PBMIF gives a value of unity in the case of a perfectly appropriated force. The negative sign in Eq. (4.33) is chosen for the sake of consistency with the MPI.

It is interesting to note that the phase of the excitation force with respect to the displacement which is required for the PBMIF to take on a value of unity is $\pi/2$ for a single excitation point in physical coordinates. This is in line with the phase criterion for the monophase case. In non-

monophase cases the power consideration suggests the same phase criterion as an approximate condition for single point excitation.

Moreover, it is noted that in the case of multi-point excitation of non-monophase motions there may exist cases where the total reactive power vanishes, but the reactive power at individual excitation locations may be non-zero. Additionally, in the case of multi-point excitation the definitions of apparent power and distortion power is non-trivial due to coupling effects between excitation points as discussed in detail in the electrical engineering community (Czarnecki, 2000). To circumvent these issues, one possibility is to require the PBMIF to be fulfilled for all individual excitation points such that a global indicator could be defined as

$$\Lambda := \frac{1}{N_j} \sum_{j=1}^{N_j} \Lambda_j \in [-1, 1] . \tag{4.34}$$

If this PBMIF takes on a value of unity, then the total power brought into the system is fully characterized by its active power component.

Remarks on Power Theory

The power based framework for NEMA presents an extension of power considerations in linear phase resonance testing to nonlinear systems. The mechanical power of the excitation can be used in linear systems to derive the phase lag quadrature criterion and to directly measure linear modal parameters such as modal mass and damping based on the stationarity of the reactive power (Géradin and Rixen, 2015). A direct extension of the stationary reactive power method to nonlinear systems, however, is complicated due to the influence of the distortion power (c.f. Eq. (4.27)).

Against this backdrop, the reactive power is of limited physical meaning in nonlinear systems. Indeed, the reactive power definition originally proposed by Budeanu (1927), which forms the foundation of the derivations made here, is controversial in the electrical engineering community (Czarnecki, 1987). Even though it still seems to be the most widely used concept, there are numerous alternatives, which are reviewed, e.g., by Svensson (1999). However, the choice of Budeanu's definition in the context of NEMA is reasonable due to two reasons. Firstly, it is a direct extension of linear power theory in electrical engineering which is familiar to most practicing engineers and it is fully consistent to the power based approaches which have already been applied to linear mechanical systems. Secondly,

the derived power quantities can be easily calculated and indicate deficiencies in the appropriated forcing. For instance, a high reactive power indicates a poor fulfillment of the phase criterion, which can even be localized to a certain harmonic, whereas a high distortion power indicates a strong influence of harmonic distortions in the force or the response, respectively.

Finally, it is noted that the active and apparent power can also be defined in the time domain. In time domain, the PBMIF directly follows from the Cauchy-Schwarz inequality, as discussed in detail in Peter and Leine (2017). However, the derivation is made here in the frequency domain because this also allows for the definition of the reactive and distortion power, which is infeasible in time domain. Moreover, the derivation is consistent to the previous approach by Peeters et al. (2011), that was also derived in the frequency domain.

4.2.3 Practical Realization of Appropriated Excitation with Phase-Locked-Loop

The phase of the excitation with respect to the response is the central quantity in nonlinear phase resonance testing. The conventional approach for monophase systems as well as the power analysis have shown that the phase lag of the force with respect to the displacement has to be $\pi/2$ for all harmonics and DOFs to isolate a nonlinear mode. For practical reasons, it is impossible to introduce a forcing at all DOFs with infinitely many frequencies and the suitable phases. However, previous studies have shown that even a single point single harmonic force allows for an approximate nonlinear mode isolation to a satisfying accuracy. In these studies, the phase lag of the excitation has been adjusted indirectly by controlling the frequency of the excitation, which is time consuming and susceptible to errors.

As, indeed, the phase is the quantity which is desired to have a specific value rather than the frequency, it seems to be a natural choice to replace the manual frequency tuning process by a concept of automatic *phase control*. In electrical engineering, controlling the phase of a signal with respect to a reference signal is a common task, e.g., in radio technology. In particular, the PLL in various implementations is a well-known concept. Actually, the first realization of the PLL is attributed to de Bellescize (1932), who proposed an analogue circuit which already contains all three essential components of modern PLLs: A phase detector, a loop filter and a voltage

1. Tuning of the excitation frequency with PLL

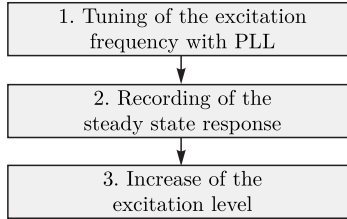| 2. Recording of the steady state response |
|---|

3. Increase of the excitation level

Figure 4.4: PLL based approach for phase resonance testing.

controlled oscillator (c.f. Fig. 4.6). Thus, this control concept is borrowed from the electrical engineering community to facilitate the phase control in NEMA. Due to the efficiency of the automatic phase control, the current procedure of NEMA (c.f. Fig. 4.1) is replaced by the procedure summarized in Fig. 4.4: The tuning is automated with a PLL controller, the free-decay is replaced by a series of steady-state measurements and the excitation is incrementally increased from low to high level. The PLL based phase resonance testing procedure is visualized in the frequency-amplitude domain in Fig. 4.5(a) and phase-amplitude domain in Fig. 4.5(b).

Phase-Locked-Loop

The PLL is a nonlinear oscillator that generates a harmonic output signal with a frequency which is tuned based on its phase difference with respect to a reference signal. The PLL is commonly divided into three blocks: the phase detector, the loop filter and the voltage controlled oscillator (VCO). The structure of the PLL attached to a mechanical structure, which is excited with an electrodynamic shaker, is shown in Fig. 4.6. There are various implementations of PLLs and their individual blocks, which are extensively discussed in review articles, e.g., by Abramovitch (2002) and Hsieh and Hung (1996), and a number of books, e.g., Best (2007) or Gardner (2005). For the application in NEMA, a simple second order analogue PLL is sufficient, which is described in the following.

The first block of the PLL is the phase detector, which extracts the phase of the output signal with respect to the reference signal. In NEMA, the
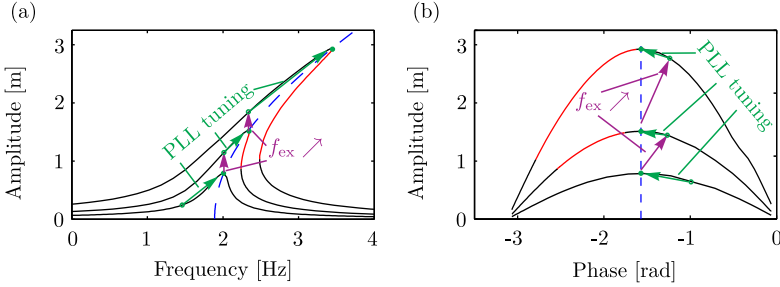
Figure 4.5: Illustration of the method in frequency-amplitude space (a) and phase-amplitude space (b).

output signal is the force $f_{\mathrm{ex}}(t)$ applied to the structure, which is indirectly controlled by the input voltage $u_0(t)$ to the shaker. As a reference signal either the acceleration, velocity or displacement at a reference point on the structure can be chosen. In this example, the reference signal is the displacement $x_{\mathrm{ref}}(t)$. The phase detection is realized by a multiplication of the input signals. Since the output of the multiplier depends on the amplitude of the input signal, a common modification is to replace the input signals by the sign function yielding

$$w(t) = \mathrm{sign}\left\{f_{\mathrm{ex}}(t)\right\}\mathrm{sign}\left\{x_{\mathrm{ref}}(t)\right\}. \tag{4.35}$$

The modification, which can be interpreted as amplitude normalization of the input, makes the output of the phase detector amplitude independent and improves the speed and stability properties of the loop as shown by Fan et al. (2007). The multiplication yields an output signal which is oscillating around a mean value being a function of the phase difference $\theta_{\mathrm{e}}(t)$ of the input signals. To suppress the oscillating component the signal is fed through a low pass filter, which is the first block of the second component of the PLL, the so-called loop filter. The low pass filter can be described by the differential equation

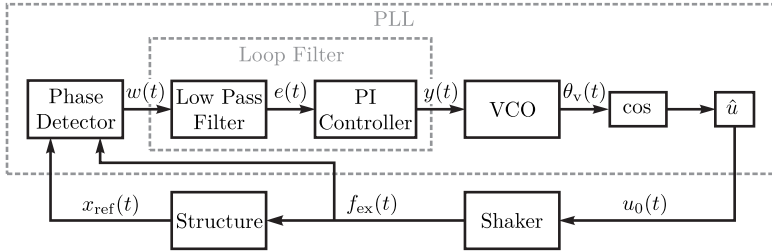$$\frac{1}{\omega_{\mathrm{L}}}\dot{e}(t) + e(t) = w(t), \tag{4.36}$$

Figure 4.6: Block diagram of the PLL attached to a test structure excited with a shaker.

with the cutoff frequency ω_L. If all oscillating components of $w(t)$ are successfully suppressed, then the output of the low pass filter equals $e(t) = f(\theta_e(t))$. This error signal $e(t)$ is then used as an input of a Proportional-Integral(PI)-controller described by the state space model

$$\begin{aligned}
\dot{z}(t) &= e(t), \\
y(t) &= K_P \left(e(t) + \frac{1}{T_I} z(t) \right),
\end{aligned} \tag{4.37}$$

with the tuning parameters K_P and T_I for the proportional and integral part, respectively. The output of the PI-controller is used as the input of the third component of the PLL, the VCO. The VCO generates the instantaneous phase of a harmonic signal by an integrator

$$\theta_v(t) = \int_0^t \omega_c + y(\tau) d\tau, \tag{4.38}$$

using the fact that the phase is the integral of the frequency. Herein, ω_c is the center frequency of the PLL at which the loop oscillates in an open loop configuration. The instantaneous phase is then inserted in a harmonic function

$$u_0(t) = \hat{u} \cos(\theta_v(t)) \tag{4.39}$$

and multiplied with a constant amplitude $\hat{u}$. This output signal of the PLL is, in the application of NEMA, used as voltage input signal for the electrodynamic shaker. If the mean value of the phase detector output is zero, the force and the reference signal are shifted in phase by $\pi/2$. Then, the PLL oscillates at a constant frequency and is said to be in a *locked state.*

There are several parameters in the PLL, which need to be tuned. For closed loop configurations, the stability bounds of the controller can be investigated using linearization techniques or Lyapunov methods (Abramovitch, 1990, 2002). However, when coupled to an unknown nonlinear vibrating structure, as in NEMA, the parameters for a stable operation may depend on the structure such that the stability bounds cannot be estimated in a straightforward way. Under the assumption of a single DOF Duffing-type, system the stability of the PLL is studied in detail by Fan et al. (2007). The analysis is generalized by Denis et al. (2018) for the case of general geometrically nonlinear structures. Both studies show that the stability bounds of the system including structure and PLL depend on the properties of the structure. As the test structure is assumed to be unknown if the PLL is used for system identification purposes, the tuning has to be done in a heuristic way. However, several studies have shown that the tuning of the PLL parameters is uncritical and a stable operation is achieved for a wide parameter range, such that a heuristic procedure is acceptable (Denis et al., 2018; Peter and Leine, 2017; Peter et al., 2016).

Remarks on Phase Control

In the conventional NEMA approach as well as in most other structural dynamics testing procedures, such as FRF tests, frequency-controlled measurements are used, i.e., the frequency of a harmonic excitation is preset by an external device. The PLL controller of the NEMA approach proposed here uses a phase-controlled excitation instead, i.e., the phase of the excitation is controlled with respect to the response and the frequency is a result of the system's response. The structure combined with the controller can be regarded as an *autoresonant* system. This type of excitation provides several advantages, particularly for testing in or near resonance. The phase-amplitude relation in Fig. 4.5(b) is single-valued and bell-shaped, whereas the frequency-amplitude relation shown in Fig. 4.5(a) is multi-valued and has a sharp bend near resonance. An autoresonant approach, therefore, has two favorable properties: (i) small perturbations in phase

have a minor influence on the response even for lightly damped systems and (ii) the phase-amplitude relation is unique, at least locally around resonance. Property (i) simplifies maintaining a resonant vibration and increases the accuracy of measurements in resonance. Property (ii) provides the advantage that, given the phase is controlled successfully, the system can be driven at any point in the phase-amplitude plane even at points which are unstable in the uncontrolled system. This *stabilizing* effect facilitates the measurement near bifurcation points and can even be used to measure the unstable branch of Duffing-type systems as shown experimentally by Mojrzisch et al. (2013).

Analytical studies of Sokolov and Babitsky (2001) show at academic examples that these advantages of phase-controlled excitation are largely independent of most system parameters, such as damping coefficients, the forcing level and even nonlinear restoring forces. Furthermore, it is noted that the concept of autoresonant forcing has been exploited for different applications such as ultrasonically assisted machining (Babitsky and Sokolov, 2007) or atomic force microscopy (García and Pérez, 2002).

In conclusion, the application of an autoresonant forcing concept seems to be particularly suitable for the purpose of NEMA, where weakly damped systems with a priori unknown system parameters are the subject of interest.

4.2.4 Extraction of the Nonlinear Modal Parameters

Once a nonlinear mode is isolated using the phase resonance approach described above, a nonlinear modal model can be extracted. The aim of this step is extracting nonlinear modal parameters which are easy to interpret and consistent with linear theory. A nonlinear modal motion in the r-th nonlinear mode can be described by a Fourier series of the form[4]

$$\boldsymbol{x}_{\mathrm{nm},r}(t) = \mathrm{Re}\left\{ \sum_{n=0}^{\infty} \underline{\tilde{\boldsymbol{\psi}}}_{r,n}\, \mathrm{e}^{\mathrm{i}n\tilde{\omega}_{0,r}t} \right\}. \tag{4.40}$$

Herein, $\tilde{\omega}_{0,r}$ denotes the nonlinear modal frequency and $\underline{\tilde{\boldsymbol{\psi}}}_{r,n}$ the n-th harmonic of the nonlinear modal deflection shape of the r-th nonlinear

---

[4]This form of the Fourier series is chosen for convenience. The relation to Fourier series notations used for the derivation of power quantities and the numerical algorithm is included in Appendix A.

mode. Both quantities are nonlinear modal quantities, which is indicated by the $(\tilde{\cdot})$ symbol, and may depend on the energy (or amplitude) with which the system oscillates. The nonlinear modal frequency $\tilde{\omega}_{0,r}$ can directly be extracted from the measurement, either as an output of the PLL during force appropriation or by Fourier transformation of the measured time series. The deflection shape $\underline{\tilde{\psi}}_{r,n}$ can also be extracted using the Fourier transform, however, to ensure consistency with linear theory where the mode shapes are typically mass normalized, a normalization strategy is proposed.

Normalization of Nonlinear Mode Shapes

For linear systems, the most common strategy is to normalize the mode shapes with respect to the mass matrix, i.e.,

$$\boldsymbol{\Phi}^{\mathrm{T}}\mathbf{M}\boldsymbol{\Phi} = \mathbf{I}_{N_i}, \quad \text{with} \quad \boldsymbol{\Phi} = \begin{bmatrix} \boldsymbol{\phi}_1 ... \boldsymbol{\phi}_{N_i} \end{bmatrix} \quad \text{and} \quad \boldsymbol{\phi}_i = \frac{1}{\sqrt{m_i}}\boldsymbol{\psi}_i, \quad (4.41)$$

where $N_i \leq N$ denotes the number of experimentally extracted linear modes, $\boldsymbol{\phi}_i$ is the mass normalized mode shape of the i-th linear mode and m_i the modal mass. With this normalization a linear modal motion of the i-th mode can be written as

$$\boldsymbol{x}_{\mathrm{lm},i}(t) = \mathrm{Re}\left\{q_i\boldsymbol{\phi}_i\mathrm{e}^{\mathrm{i}\omega_{0,i}t}\right\}, \quad (4.42)$$

with the modal amplitude $q_i = \sqrt{m_i}$. Analogously, the Fourier series describing the nonlinear modal motion in Eq. (4.40) can be recast in the form

$$\boldsymbol{x}_{\mathrm{nm},r}(t) = \mathrm{Re}\left\{\sum_{n=0}^{\infty} \tilde{q}_r\underline{\tilde{\phi}}_{r,n}\mathrm{e}^{\mathrm{i}n\tilde{\omega}_{0,r}t}\right\}, \quad (4.43)$$

with the nonlinear modal amplitude $\tilde{q}_r$ and a normalized nonlinear mode shape $\underline{\tilde{\phi}}_{r,n}$.

To ensure consistency of Eq. (4.43) to the linear modal motion described in Eq. (4.42) the first harmonic of the nonlinear modal deflection shape is chosen to be normalized with respect to the mass matrix, i.e.,

$$\underline{\tilde{\phi}}_{r,1}^{\mathrm{H}}\mathbf{M}\underline{\tilde{\phi}}_{r,1} = 1, \quad \text{with} \quad \underline{\tilde{\phi}}_{r,n} = \frac{1}{\tilde{q}_r}\underline{\tilde{\psi}}_{r,n}. \quad (4.44)$$

The mass matrix is unknown in experiments, such that an experimentally derived estimate of the mass matrix has to be calculated. To this end, the mode shapes from a linear EMA can be used, as they are commonly mass normalized based on the driving point FRF measurement (Ewins, 2000). Using the normalized linear eigenvectors, the mass matrix can be estimated as

$$\mathbf{M}_{\mathrm{exp}} = (\mathbf{\Phi}^{\mathrm{T}})^{+} \mathbf{I}_{N_i} \mathbf{\Phi}^{+}, \tag{4.45}$$

where the $(\cdot)^{+}$ operator denotes the (generalized)[5] inverse of the eigenvector matrix. Inserting Eq. (4.45) in Eq. (4.44) yields the condition

$$\tilde{\underline{\phi}}_{r,1}^{\mathrm{H}} \mathbf{M}_{\mathrm{exp}} \tilde{\underline{\phi}}_{r,1} = \tilde{\underline{\phi}}_{r,1}^{\mathrm{H}} (\mathbf{\Phi}^{\mathrm{T}})^{+} \mathbf{\Phi}^{+} \tilde{\underline{\phi}}_{r,1} = 1, \tag{4.46}$$

or in terms of the nonlinear modal amplitude

$$\frac{1}{\tilde{q}_r^2} \tilde{\underline{\psi}}_{r,1}^{\mathrm{H}} (\mathbf{\Phi}^{\mathrm{T}})^{+} \mathbf{\Phi}^{+} \tilde{\underline{\psi}}_{r,1} = 1. \tag{4.47}$$

The normalized mode shapes can subsequently be used to derive a nonlinear modal damping measure which is also consistent with linear theory.

Nonlinear Modal Damping Measures

Although the methodology for NEMA which is proposed here aims at extracting the modal properties of the undamped nonlinear system, the damping can be quantified during the modal test. A quantification of the damping is useful to verify the hypothesis of weak, linear and proportional damping. Furthermore, the use of the derived nonlinear modal model, e.g., for the prediction of the response to different excitation scenarios (c.f. Chapter 5.1), requires an estimate of the damping.

A simple means of damping quantification can be obtained based on the linear modal damping ratios δ_i which are estimated by a linear modal analysis. However, the nonlinear modal frequency $\tilde{\omega}_{0,r}$ and the nonlinear mode shape $\tilde{\underline{\psi}}_{r,n}$ may be different to the linear modal parameters of the same mode. To be more precise, the nonlinear mode shape is generally a combination of contributions of several linear modal coordinates. If the

---

[5]The generalized Moore-Penrose inverse is used, because the eigenvector matrix may be non-square as the number of measured points can exceed the number of extracted modes, i.e., $N \geq N_i$.

linear modes have significantly different damping values, then this coupling of several linear modes may change the damping properties of the system. An experimental representation of the linear modal damping matrix can be calculated as

$$\mathbf{\Phi}^{\mathrm{T}}\mathbf{D}_{\mathrm{exp}}\mathbf{\Phi} = \mathbf{D}_{\mathrm{mod}} = \mathrm{diag}\left\{2\delta_i\omega_{0,i}\right\}. \tag{4.48}$$

Using this damping representation, the nonlinear mode shapes can be projected onto the experimentally extracted damping matrix, analogously to Eq. (4.46), yielding a *projected linear modal damping* coefficient

$$\tilde{\delta}_r^{\mathrm{pl}} = \frac{1}{2\tilde{\omega}_{0,r}}\tilde{\boldsymbol{\phi}}_{r,1}^{\mathrm{H}}(\mathbf{\Phi}^{\mathrm{T}})^{+}\mathbf{D}_{\mathrm{mod}}\mathbf{\Phi}^{+}\underline{\tilde{\boldsymbol{\phi}}}_{r,1}, \tag{4.49}$$

which takes into account the coupling of different modes and the change in modal frequency. This projected linear damping measure is essentially based on the damping quantification of the linear EMA and the hypothesis of proportional damping. It is well-known that damping quantification is the most elaborate part of EMA and the hypothesis of amplitude independent modal damping is in many cases only a rough approximation of reality.

In view of the problems of damping quantification in EMA, an alternative damping measure, which is entirely based on the NEMA measurements is proposed. The steady-state measurements which are used in the proposed NEMA procedure allow for the quantification of the effective damping for every point of the measured backbone curve. To this end, the active power of the excitation forces P which is defined in Eq. (4.21) can be used. The active power is in balance with the mean dissipated power over one period

$$P_{\mathrm{diss}} = \frac{1}{T}\int_0^T \dot{\boldsymbol{x}}(t)^{\mathrm{T}}\mathbf{D}\dot{\boldsymbol{x}}(t)\mathrm{d}t, \tag{4.50}$$

which can be evaluated in the frequency domain using Parseval's theorem yielding

$$P_{\mathrm{diss}} = \sum_{n=1}^{\infty}\frac{1}{2}(n\tilde{\omega})^2\underline{\boldsymbol{x}}_n^{\mathrm{H}}\mathbf{D}\underline{\boldsymbol{x}}_n, \tag{4.51}$$

or in terms of nonlinear modal quantities (see Eq. (4.43)) as

$$P_{\text{diss}}^r = \sum_{n=1}^{\infty} \frac{1}{2} (n\tilde{\omega}_{0,r})^2 \tilde{q}_r^2 \underline{\tilde{\phi}}_{r,n}^{\text{H}} \mathbf{D} \underline{\tilde{\phi}}_{r,n}. \tag{4.52}$$

In analogy to linear theory, a damping measure $\tilde{\delta}_{r,n}^{\text{nl}}$ for the r-th nonlinear mode and the n-th harmonic can be defined as

$$\underline{\tilde{\phi}}_{r,n}^{\text{H}} \mathbf{D} \underline{\tilde{\phi}}_{r,n} = 2\tilde{\omega}_{0,r} \tilde{\delta}_{r,n}^{\text{nl}}, \tag{4.53}$$

which will henceforth be referred to as *nonlinear modal damping* coefficient. Under the assumption of viscous damping, i.e., a linear dependency of attenuation and frequency, the damping coefficient is the same for all harmonics $\tilde{\delta}_{r,1}^{\text{nl}} = \tilde{\delta}_{r,n}^{\text{nl}} = \tilde{\delta}_r^{\text{nl}}$ (Laxalde and Thouverez, 2009). Thus, the modal damping measure can be evaluated based on the fundamental harmonic component of the dissipated power, yielding

$$P_{\text{diss},1}^r = \tilde{\delta}_r^{\text{nl}} \tilde{\omega}_{0,r}^3 \tilde{q}_r^2. \tag{4.54}$$

Note that this definition is consistent with linear theory, i.e., for $\tilde{\delta}_r^{\text{nl}} = \delta_r$. Under the assumption that the active power of the excitation is in balance with the power of the damping forces, the nonlinear modal damping coefficient can be calculated as

$$\tilde{\delta}_r^{\text{nl}} = \frac{P_1}{\tilde{q}_r^2 \tilde{\omega}_{0,r}^3}, \tag{4.55}$$

where P_1 is the first harmonic of the active power of the excitation. This nonlinear modal damping coefficient is generally an amplitude dependent measure, which can be used to capture the amplitude dependence of the damping behavior.

4.3 Numerical Example

This section comprises an illustrative numerical example which demonstrates the functionality of the method and elucidates some of the advantages compared to previous methods for NEMA. A numerical example provides the advantage that the nonlinear modes, as periodic solution of the autonomous conservative system, can be easily calculated as a reference solution using the numerical algorithm described in Chapter 3. Additional

numerical examples, which discuss tuning aspects of the PLL controller and the effect of internal resonances can be found in Peter et al. (2016) and Peter and Leine (2017).

The numerical example system resembles the experimental benchmark used in Chapter 6 and is inspired by the so-called ECL-beam proposed by Thouverez (2003) as a benchmark for system identification methods. The structure is depicted in Fig. 4.7(a) and consists of a beam with the thickness 12 mm and length 700 mm, which is clamped at the left end and supported by a cubic spring, a linear translational and linear rotational spring at the right end. The beam is discretized with seven Timoshenko beam elements and the parameters are given in Tab. 4.1.

To verify the results obtained with the proposed NEMA procedure a numerical nonlinear modal analysis with nine harmonics is carried out. The frequency-energy plot of the first fundamental nonlinear mode of the beam is depicted in Fig. 4.7(b) and the linear bending eigenfrequencies are listed in Tab. 4.1. The frequency-energy plot reveals two modal interactions in the high energy regime, a 3:1 interaction with the second bending mode and a 7:1 interaction with the third bending mode. Both modal interactions, however, are beyond the regime of realistic deformations in experiments such that they are not further investigated here.

For the numerical experiment with the PLL based NEMA procedure, a model of the structure and the PLL controller are implemented in Matlab/Simulink. To account for the effect of shaker structure interactions the shaker is modeled and included in the simulations[6]. In the numerical experiment, light proportional damping $\mathbf{D} = \alpha_1 \mathbf{K} + \alpha_2 \mathbf{M}$ with the parameters included in Tab. 4.1 is added to the structure, leading to the modal damping ratios listed in Tab. 4.1.

For the extraction of the backbone curve, the force appropriation strategy described in Section 4.2.3 is pursued, i.e., the excitation force is generated by a sinusoidal input voltage into to shaker, of which the phase is controlled by the PLL[7]. The actual excitation force is, therefore, the reaction force between shaker and structure which results from the input voltage to the shaker. The resulting excitation force is then used as an input for the PLL. The displacement at the excitation point is used as reference signal of the response. The input voltage is incrementally increased from low to high every ten seconds and overall 36 forcing levels

---

[6]For details regarding the shaker model the reader is referred to Appendix F.

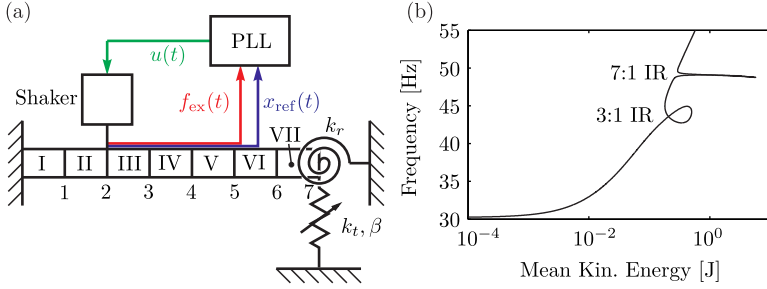[7]The parameters of the PLL are listed in Appendix G, Tab. G.1.

Figure 4.7: Schematic sketch of the numerical experiment (a) and frequency-energy plot of the first bending mode of the beam (b).

Parameter	Value	Unit	Frequency [Hz]	Damping [%]
E	200	GPA	30.23	0.18
ρ	7830	kg/m^3	126.21	0.23
k_c	4000	N/m	340.16	0.55
k_r	100	Nm/rad	657.46	1.04
β	10^9	N/m^3	1075.72	1.69
α_1	$5 \cdot 10^{-6}$	s	1562.01	2.46
α_2	0.5	s^{-1}	1984.53	3.11

Table 4.1: Parameters of the beam model (left) and linear eigenfrequencies and modal damping ratios of the bending modes of the beam (right).

are measured. The displacements and velocity at all DOFs and the output frequency of the PLL are recorded. For the following analysis, the response and force signals are transferred into the frequency domain using a FFT. Therefore, the output frequency of the PLL is used to isolate the last 20 periods of each forcing level. Thus, leakage in the FFT can be avoided as an integer multiple of the period length can be used for the analysis.

In the first example, the structure is excited with the shaker at the second point and the tracked backbone curve for the drive point is visualized in Fig. 4.8(a). In this plot, the first harmonic of the displacement obtained with the PLL (black o) is shown along with the simulated nonlinear mode
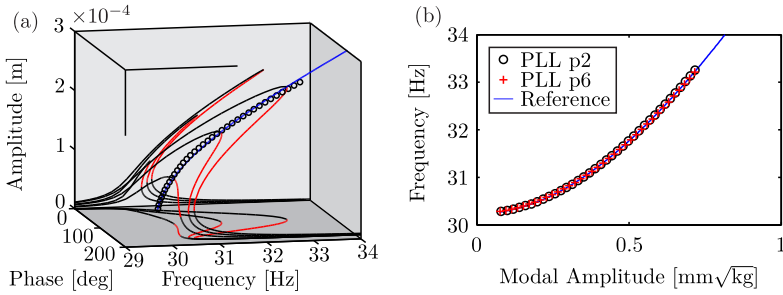
Figure 4.8: Illustration of the PLL based backbone (black o), the reference back-
bone (blue) and the FRF (black: stable, red: unstable) of the example
system (a) and nonlinear modal frequency over amplitude for two ex-
citation points and reference solution (b).

of the conservative system (blue curve) and the frequency response for
three different levels of sinusoidal excitation (stable solutions: black curve,
unstable solutions: red curve[8]). It can be seen that the PLL is capable
of keeping track of the backbone curve and that the results obtained with
the PLL method are very similar to the backbone curve of the autonomous
system. Moreover, it can be observed that the measured points are very
close to the fold bifurcation point of the FRF such that the measurement
with manual tuning would be very difficult in practice.

The nonlinear modal parameters of the PLL results are extracted as de-
scribed in Section 4.2.4. Additionally, the modal parameters are extracted
for a PLL excitation at point six of the beam and for the reference results,
i.e., the nonlinear modes of the autonomous system. The obtained non-
linear modal frequency is plotted against the extracted modal amplitude
in Fig. 4.8(b). It can be seen that, independently of the excitation point,
the PLL results almost perfectly overlay the reference curve.

Next, the attention is drawn to the PBMIF and a more detailed analysis
of the extracted mode shapes. Firstly, the PBMIF Λ for an excitation at
the second point is compared against the MPI for a single harmonic Δ_1 and

---

[8]The FRF is calculated with an algorithm analogous to the algorithm for nonlinear
mode calculation presented in Chapter 3 and the stability calculation based on
Hill's determinant is implemented similarly to the methods described by Von Groll
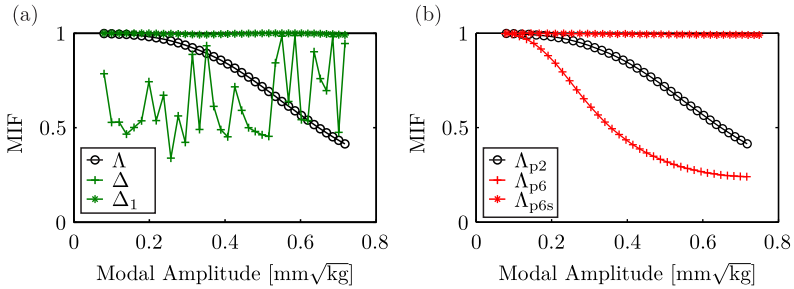and Ewins (2001) and Detroux et al. (2015).

Figure 4.9: Comparison PBMIF, fundamental harmonic MPI and higher harmonic MPI (a) and PBMIF for different forcing scenarios (b).

for multiple harmonics Δ in Fig. 4.9(a). It can be seen that the PBMIF successively decreases for increasing excitation level indicating some imperfections in the excitation. In contrast, the MPI for multiple harmonics jumps from one point to another, which can be attributed to the influence of higher harmonics, the phase of which is uncontrolled. As the MPI takes the arithmetic mean of all harmonics, the phase of frequency components with small or even negligible amplitudes are weighted the same as the phase of the fundamental harmonic. If only the fundamental harmonic, of which the phase is controlled, is taken into account, then the MPI suggests that the nonlinear mode is perfectly isolated. These results confirm the observation made in literature, that the MPI is not a conclusive measure for the estimation of the mode isolation quality, whereas the PBMIF shows a clear trend. In Fig. 4.9(b) the PBMIF for the excitation at point two Λ_{p2} is compared to the PBMIF for an excitation at point six Λ_{p6}. Additionally, the PBMIF Λ_{p6s} for an excitation at point six with a sinusoidal force with controlled phase is shown for comparison[9]. It can be seen that, if the shaker model is included in the simulation, then the PBMIF suggests that the excitation at point two yields superior results compared to point six. It is interesting to note, that the PBMIF is close to unity for the excitation at point six, if the shaker model is not included, i.e., a sinusoidal force is enforced. This is attributed to the fact that the decrease of the PBMIF

---

[9]The sinusoidal excitation force is then generated by replacing the shaker model with a sinusoidal signal generator of which the frequency is generated by the PLL.
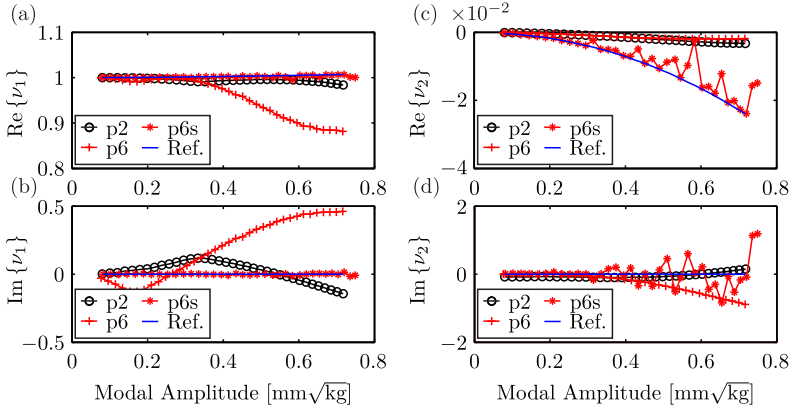
Figure 4.10: Comparison of linear modal participation factors of the first mode (real part (a), imaginary part (b)) and the second mode (real part (c), imaginary part (d)) for different forcing scenarios.

is mainly caused by strong distortions in the excitation force, due to the nonlinear feedback from the structure to the shaker.

The consequences of these distortions are illustrated by a more detailed analysis of the obtained nonlinear mode shapes. To this end, the extracted nonlinear modal motion is projected onto the linear modes to obtain the vector of modal participation factors

$$\boldsymbol{\nu} = \sum_{n}^{N_h} \boldsymbol{\Phi}^+ \underline{\tilde{\boldsymbol{\phi}}}_{r,n}. \tag{4.56}$$

The nonlinear modal motion is dominated by contributions ν_1 and ν_2 of the first and second linear modes and these are therefore considered in the following. The real and imaginary parts of the first modal participation factor ν_1 for the excitation at point two (p2) and six (p6) (with and without shaker model) and the reference solution are shown in Fig. 4.10(a) and (b), respectively. Regarding the reference solution, it can be seen that the real part of ν_1 is close to unity, whereas the imaginary part is zero. This means that the nonlinear modal motion is indeed very similar to the linear mode
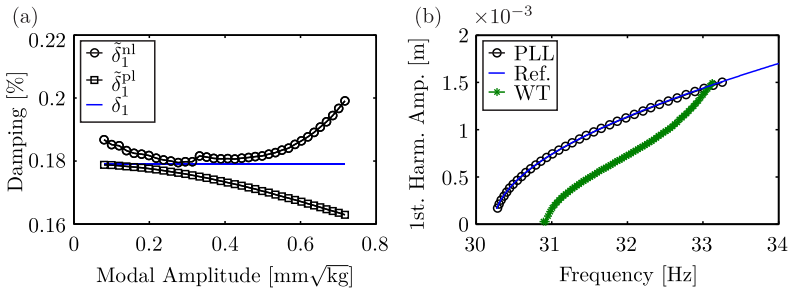
Figure 4.11: Comparison of linear, projected linear and nonlinear modal damping ratio (a) and comparison of the PLL based backbone with the backbone obtained by a free-decay analysis (b).

shape of the first mode. For sinusoidal excitation at point six (p6s), the curves almost perfectly overlay the reference solution, whereas there is some deviation for the nonsinusoidal excitation, i.e., the simulations including the shaker dynamics. For the excitation at point two, the deviation in the real part is very small, but there is some deviation in the imaginary part, i.e., a deviation from a monophase motion. For the excitation at point six with shaker model, the deviation is larger compared to point two. The contribution of the second linear modal coordinate, which is shown in Fig. 4.10(c) and (d), is almost two orders of magnitude smaller compared to the first linear modal coordinate. However, the same trend can be observed, i.e., the distortion of the mode shape for the sinusoidal excitation is smaller compared to the nonsinusoidal excitation at point two and the nonsinusoidal excitation at point six yields the highest distortions. It is interesting to note that this observation perfectly correlates with the values of the PBMIF (c.f. Fig. 4.9(b)).

The damping measures that can be extracted with the proposed NEMA framework are shown in Fig. 4.11(a). It can be seen that the linear, projected linear and nonlinear damping measure yield different results for higher amplitudes. However, it is difficult to validate these damping measures, as the reference solution is obtained by solution of the undamped system. The study of the damping measures, therefore, has to be done in

the verification step of the methodology proposed in Fig. 1.1. The verification of the extracted models is addressed in Chapters 5 and 6.

Finally, the results obtained with the novel NEMA approach are compared against the results obtained with the previous method. To this end, the input voltage to the shaker is set to zero at the end of the PLL based NEMA and the free-decay is recorded. During free-decay the shaker remains connected to the structure as it is the case in real experiments. The free-decay is analyzed using a self-coded Morlet WT algorithm[10]. Exemplary, the backbone curve for the beam tip obtained with the PLL method for an excitation at point two, the free-decay and the reference solution are shown in Fig. 4.11(b). It can be seen that the free-decay significantly deviates from the reference solution and the PLL results. The differences can be explained by the influence of the shaker. Firstly, the switching off of the excitation induces an impulsive force, which changes the shape of the backbone curve at the beginning of the decay process. Secondly, the passive shaker changes the mechanical properties of the structure such that the measured linear eigenfrequencies are affected. Therefore, the backbone curve is shifted in frequency. These differences also have been observed in laboratory measurements as described in Peter and Leine (2017). It can be seen that the PLL method significantly increases the accuracy of the backbone curve compared to the free-decay, at least in cases where shaker excitation is used. This aspect of the free-decay method has been rarely discussed in literature before.

4.4 Extension to Nonsmooth Systems

The previous studies using nonlinear phase resonance approaches exclusively treat systems with smooth nonlinearities. However, nonsmooth nonlinearities such as unilateral constraints inducing impacts are of high practical relevance in industrial application. The strong nonlinear effects induced by nonsmooth nonlinearities greatly complicate the manual tuning of the excitation. Moreover, strong and sudden changes may occur during a freely decaying vibration such that a high resolution is required for the TFA and transient effects may bias the obtained results.

The phase controlled approach which is proposed here, however, is robust also in the case of severe nonlinear effects, such as high harmonic

---

[10]The implemented algorithm is mainly based on the publications by Jordan et al. (1997) and Staszewski (1997).

distortions. The steady-state analysis allows for an arbitrary resolution of the backbone curve, such that strong energy dependence can be analyzed in great detail. Thus, in a first approximation, essentially the same experimental procedure can be used for nonsmooth systems as proposed for smooth systems. This first approach is based on the assumptions that (i) a single harmonic and single point force is still sufficient for nonlinear mode isolation and (ii) that the nonsmooth interactions do not lead to strongly nonlinear damping effects. These assumptions can provide reasonable results in some cases (c.f. Section 6.2), but the limitations need to be thoroughly investigated. However, the new approach provides the potential for an extension to more complicated forcing scenarios and to nonlinearly damped systems as addressed in the next section.

In conclusion, the new NEMA procedure provides an interesting technique for the analysis of the dynamic behavior of nonsmooth systems. This is particularly interesting due to the fact that the experimental analysis of nonsmooth systems is, in many ways, still a difficult endeavor.

4.5 Extension to Nonconservative Nonlinearities

A generalization of the proposed NEMA approach is possible in the framework of the extended periodic motion concept for nonconservative systems (c.f. Definition 2.3). The method, which is referred to as *extended phase resonance testing*, is briefly outlined here and the details are published in Scheel et al. (2018b).

The ENMs as defined in Definition 2.3 are periodic solutions of the differential equation

$$\mathbf{M}\ddot{\boldsymbol{x}}(t) + \mathbf{D}\dot{\boldsymbol{x}}(t) + \mathbf{K}\boldsymbol{x}(t) + \boldsymbol{f}_{\mathrm{nl}}(\boldsymbol{x}(t), \dot{\boldsymbol{x}}(t)) - \xi\mathbf{M}\dot{\boldsymbol{x}}(t) = \mathbf{0}. \qquad (4.57)$$

which approximates the behavior of the damped autonomous system. Therefore, the parameter ξ in the artificial self-excitation term $\xi\mathbf{M}\dot{\boldsymbol{x}}(t)$ is chosen such, that the motion becomes periodic. In numerical simulations, for which the extended periodic motion concept has originally been proposed by Krack (2015), this leads to an additional unknown ξ which can be calculated such that the periodicity condition is fulfilled (c.f. Section 3.5). In experiments, the mass proportional self-excitation term cannot be simply imposed. However, the behavior of the self-excitation can be imitated by

an appropriate excitation force, i.e.,

$$\xi \mathbf{M} \dot{\boldsymbol{x}}(t) = \boldsymbol{f}_{\text{ex}}(t), \tag{4.58}$$

which can, analogously to the case of conservative nonlinear modes (c.f. Section 4.1.1), be written in frequency domain

$$\mathrm{i}n\omega\xi \mathbf{M}\underline{\boldsymbol{x}}_n = \underline{\boldsymbol{f}}_{\text{ex},n} \quad \forall n. \tag{4.59}$$

The self-excitation term has similar properties to the viscous damping in Eq. (4.6) which ought to be balanced in conventional phase resonance testing. In particular, both quantities are velocity proportional leading to similar characteristics of an appropriated excitation force. Due to the velocity dependence, the self-excitation is, in analogy to viscous damping forces, fully described by its active power component. Hence, the excitation force has the same characteristics as in the conservative case yielding the power condition

$$S_j = |P_j| . \tag{4.60}$$

Therefore, for the j-th excitation point the phase of the excitation has to be shifted in phase by $\pi/2$ with respect to the displacement which can be achieved with a PLL controller, just as in the conservative case. Furthermore, the PBMIF is also valid for ENMs and the modal parameters can be extracted analogously to the conservative case. The ENMs are periodic solutions of Eq. (4.57), i.e., the nonlinear modal motion of the r-th ENM can be written as Fourier series

$$\boldsymbol{x}_{\text{em},r}(t) = \mathrm{Re}\left\{ \sum_{n=0}^{\infty} \tilde{q}_r \underline{\tilde{\boldsymbol{\phi}}}_{r,n} \mathrm{e}^{\mathrm{i}n\tilde{\omega}_{\text{em},r}t} \right\}, \tag{4.61}$$

with the ENM frequency $\tilde{\omega}_{\text{em},r}$. Furthermore, the damping behavior can be characterized by means of the equivalent modal damping measure, which is related to the self-excitation parameter ξ by (Krack, 2015)

$$\xi = 2\tilde{\delta}_r^{\text{nl}}\tilde{\omega}_{0,r} = \frac{2P_1}{\tilde{q}_r^2\tilde{\omega}_{0,r}^2} \tag{4.62}$$

This damping measure can be evaluated based on the measured active power of the excitation force, as in the case of conservative nonlinear modes (c.f. Eq. (4.55)).

Besides the apparent analogies of extended and conventional phase resonance testing, an important conceptual difference shall be pointed out. Whereas conventional phase resonance testing aims at imitating the behavior of the autonomous conservative system by balancing out the damping terms by external forcing, extended phase resonance testing aims at creating a forced system imitating the behavior of the self-excited surrogate system in Eq. (4.57). It is therefore accepted in extended phase resonance testing that the external force causes distortions compared to the original autonomous systems, as long as the distortions have a specific form.

4.6 Summary

A novel framework for nonlinear phase resonance testing has been proposed in this chapter, which covers the key issues of previous approaches. In particular the following contributions are made:

- A novel theoretical framework for nonlinear modal testing based on power quantities borrowed from electrical engineering and a generalization of the phase condition to non-monophase nonlinear modes is derived.

- The assessment of mode isolation quality is addressed and a new mode indicator function, the PBMIF, is proposed.

- An automatic phase control strategy for the efficient and robust practical realization of the appropriated excitation is suggested.

- The extraction of nonlinear modal parameters, which are consistent to linear theory, is explained.

The proposed method is illustrated using a realistic numerical example of a beam structure with cubic nonlinearity and the quality of the obtained results is discussed. Finally, it is indicated how the proposed method can be applied to systems with *nonsmooth nonlinearities* and how systems with *nonlinear damping* can be treated in the framework of the extended periodic motion concept. An experimental demonstration for nonsmooth and nonlinearly damped structures is included in Chapter 6.

Chapter 5

Identification of Predictive Models Based on Nonlinear Modes

In this chapter, three different methods for the derivation of predictive models based on NEMA are presented. The approaches pursue fundamentally different philosophies. The first approach, described in Section 5.1, aims at directly using the identified nonlinear modal parameters for building a predictive model. Hence, the modal parameters from the NEMA form the foundation of a (dark) *gray-box identification* strategy in nonlinear modal domain. The other approaches follow the typical system identification process described in Chapter 1. The second approach, described in Section 5.2, combines an experimentally derived linear modal model with the analytically derived frequency domain representation of the nonlinear forces in physical coordinates using the HBM. Therefore, the approach is referred to as *analytical-experimental* identification approach. For this method, the type and location of the nonlinear forces have to be known and the focus is put on the quantification of the nonlinearity. The third approach, described in Section 5.3, aims at deriving an FE model of a structure in physical coordinates. Again, special emphasis is put on the nonlinearity quantification step, which is performed by model updating. Therefore, in this approach NEMA is embedded in a *white-box model updating* strategy. The different approaches are briefly discussed in terms of their applicability and their limitations in Section 5.4. The contributions made in this chapter are summarized in Section 5.5.

5.1 Gray-Box Approach in Nonlinear Modal Coordinates

The extraction of nonlinear modal parameters has been addressed in Chapter 4. The extracted nonlinear modal parameters, i.e., nonlinear modal frequencies, shapes and damping values, constitute a *nonlinear modal model.*

This modal model can directly be used for vibration prediction of nonlinear structures. This approach, which is common practice for linear systems, is challenging for nonlinear systems due to the lack of a general superposition principle. The question of how models containing nonlinear modal data of single nonlinear modes or some superposition of multiple modes can be used for vibration prediction apart from the nonlinear modal vibration, is vividly discussed in nonlinear model order reduction context (see, e.g., Krack (2014)). The single nonlinear mode method, which has been proposed by Szemplinska-Stupnicka (1979) for the prediction of steady-state vibrations of a forced and damped system in the vicinity of an isolated resonance, forms the foundation of several numerical studies, e.g., by Laxalde and Thouverez (2009). In its original form, the method assumes that the motion of a forced and damped nonlinear system around an isolated nonlinear mode is dominated by a single nonlinear mode, i.e., it can be modeled by a single nonlinear modal oscillator. Modified versions of this approach assume that the steady-state response of nonlinear systems can be calculated as a linear superposition of the contributions of several nonlinear modes (Gibert, 2003; Setio et al., 1992) or a single nonlinear and several linear modes (Chong and Imregun, 2001; Krack et al., 2013). All of these studies have in common that they are based on numerical models of nonlinear modal oscillators, which are either used as a reduced order model to efficiently calculate the FRF or used to fit measured FRF data to identify the nonlinear modal parameters. In this thesis, however, the inverse procedure is proposed as a means of deriving a predictive model for the calculation of the steady-state forced response in the vicinity of a single nonlinear mode on the basis of modal parameters obtained with phase resonance testing.

Single Nonlinear Mode Method

The approach, of which the details have been published in Peter et al. (2018a), is purely based on experimental data and does not require any a priori model. However, some assumptions about the model structure have to be made and the range of validity is restricted, such that the approach is termed *gray-box* approach here. These limitations and assumptions are:

1. The method aims at calculating steady-state vibrations around resonance to, in first approximation, single harmonic forcing.

2. The nonlinear modes of the system are well-isolated and do not undergo pronounced nonlinear modal coupling in the energy range of interest, e.g., caused by internal resonances.

3. The vibration energy of the forced and damped system is mainly confined to a single nonlinear mode r.

Obviously, these assumptions are not met by arbitrary nonlinear systems and they have to be verified carefully for each individual case. Under the aforementioned assumptions the steady-state response around resonance is approximated by a nonlinear modal oscillator with the experimentally derived parameters (c.f. Eq. (4.43)), i.e.,

$$
\boldsymbol{x}_{\mathrm{nl}}(t) \approx \boldsymbol{x}_{\mathrm{nm},r}(t) = \mathrm{Re}\left\{ \sum_{n=0}^{N_h} \tilde{\underline{q}}_r \underline{\tilde{\boldsymbol{\phi}}}_{r,n} \mathrm{e}^{\mathrm{i}n\Omega t} \right\}, \tag{5.1}
$$

where $\Omega \approx \tilde{\omega}_{0,r}$ is the frequency of an external excitation and N_h is the number of harmonics to which the nonlinear modal motion is truncated for practical reasons. Using this approximation the response of the r-th nonlinear mode can be calculated for every harmonic individually by projection of the nonlinear mode shape onto the equation of motion of a forced and damped system (c.f. Eq. (4.1)). For the fundamental harmonic component this yields

$$
[-\Omega^2 + 2\mathrm{i}\Omega\tilde{\omega}_{0,r}\tilde{\delta}_r + \tilde{\omega}_{0,r}^2]\tilde{\underline{q}}_r = \underline{\tilde{\boldsymbol{\phi}}}_{r,1}^{\mathrm{H}} \boldsymbol{f}_{ex,1}, \tag{5.2}
$$

which is a complex implicit equation for $\tilde{\underline{q}}_r$, because the nonlinear modal parameters $\tilde{\omega}_{0,r}, \tilde{\delta}_r$ and $\underline{\tilde{\boldsymbol{\phi}}}_{r,1}$ depend on the nonlinear modal amplitude $\tilde{\underline{q}}_r$. Therefore, the equation has to be solved iteratively, e.g., using the predictor-corrector method described in Section 3.2.3. Furthermore, it should be noted that the modal parameters from the NEMA are only available at discrete measured points, such that an interpolation scheme is used to evaluate Eq. (5.2) during the iteration process. The formulation for higher harmonics $n \neq 1$ can be written as

$$
\underline{\tilde{\boldsymbol{\phi}}}_{r,n}^{\mathrm{H}}[-n^2\Omega^2\mathbf{M} + 2\mathrm{i}n\Omega\mathbf{D} + \mathbf{K}]\underline{\tilde{\boldsymbol{\phi}}}_{r,n}\tilde{\underline{q}}_r = \underline{\tilde{\boldsymbol{\phi}}}_{r,n}^{\mathrm{H}} \boldsymbol{f}_{\mathrm{ex},n}. \tag{5.3}
$$

If the systems vibrates exactly in a nonlinear mode, this equation would be fulfilled under the absence of damping and excitation forces. For purely fundamental harmonic forcing the excitation force of the higher harmonics

is zero, i.e., $\boldsymbol{f}_{\mathrm{ex},n} = \boldsymbol{0}$ for $n \neq 1$, but there are still damping forces affecting the higher harmonic vibrations. In the case of weak damping, however, Eq. (5.3) is approximately fulfilled in the vicinity of a nonlinear mode. Furthermore, in real experiments additional distortions in the excitation force are anticipated (c.f. Sections 4.3 and 6.1), such that $\boldsymbol{f}_{\mathrm{ex},n} \neq \boldsymbol{0}$. Nevertheless, it is expected that the response near resonance is dominated by the systems eigendynamics, which is also the reason why a comparatively good mode isolation can be achieved with single point single harmonic forcing.

Influence of Remaining Modes and Residual Flexibility

The FRF calculation method can be regarded as an extension of the FRF synthesis, which is commonly done in the process of linear EMA for the verification of the derived modal model. To be more precise, the method is closely related to single degree of freedom EMA methods, where one mode is fitted at a time to extract nonlinear modal parameters (c.f. Ewins (2000)). Similarly to linear systems, the FRF of the nonlinear system is affected by neighboring modes, particularly, if the excitation frequency departs from the resonance frequency. To correct this effect (i) the contribution of the remaining modes can be included in the model and (ii) the residual flexibility of modes which are outside the considered frequency band can be taken into account.

Method (i) corresponds to the approaches by Chong and Imregun (2001) and Krack et al. (2013) and can be justified based on the fact that the contribution of the remaining linear modes is negligible in close vicinity of the resonance, where the system behaves nonlinearly, but gains importance further away from resonance, where the amplitudes are small and the system essentially behaves as its linearization. Therefore, the modal contributions of the remaining linear modes is calculated as in linear EMA as

$$\underline{\boldsymbol{x}}_{\mathrm{ln}} = \sum_{i \neq r}^{N_i} \frac{\boldsymbol{\phi}_i \boldsymbol{\phi}_i^{\mathrm{T}}}{-\Omega^2 + 2\mathrm{i}\Omega\omega_{0,i}\delta_i + \omega_{0,i}^2} \boldsymbol{f}_{\mathrm{ex}} \tag{5.4}$$

and simply added to the response calculated according to Eq. (5.2). With this method the calculated FRF apart from the resonance is essentially the same as in the linear case.

Method (ii) aims at modeling the influence of modes which have not been considered in the modal analysis procedure by two simple correction terms: One term modeling low frequency modes and another term mod-

eling high frequency modes. For convenience, these terms are written as pseudo modes for the low frequency contribution

$$\underline{\boldsymbol{x}}_{\text{lf}} = \frac{\boldsymbol{\phi}_{\text{lf}}\boldsymbol{\phi}_{\text{lf}}^{\text{T}}}{-\Omega^2 + \omega_{\text{lf}}^2}\boldsymbol{f}_{\text{ex}} \tag{5.5}$$

and the high frequency contribution

$$\underline{\boldsymbol{x}}_{\text{hf}} = \frac{\boldsymbol{\phi}_{\text{hf}}\boldsymbol{\phi}_{\text{hf}}^{\text{T}}}{-\Omega^2 + \omega_{\text{hf}}^2}\boldsymbol{f}_{\text{ex}}, \tag{5.6}$$

where ω_{lf} and ω_{hf} denote the lower and upper limit of the considered frequency band, respectively. Both factors can be identified by fitting measured FRFs at the low end and the high end of the frequency range of interest with the calculated FRF. The total response is then calculated as the superposition of the nonlinear contribution, which determines the response around resonance, and the linear contribution as well as the low and high frequency residual influence, determining the response further away from resonance, yielding

$$\underline{\boldsymbol{x}} \approx \underline{\boldsymbol{x}}_{\text{nl}} + \underline{\boldsymbol{x}}_{\text{ln}} + \underline{\boldsymbol{x}}_{\text{lf}} + \underline{\boldsymbol{x}}_{\text{hf}}. \tag{5.7}$$

Process for Gray-Box Identification

An overview of the identification process with the gray-box approach is given in Fig. 5.1. The mandatory steps for deriving a predictive model for FRF calculation are shown in black, whereas the gray parts of the process are optional steps to increase the range of validity of the model. Starting from the NEMA and a linear EMA measurement, the parameters of the nonlinear modal model, i.e., nonlinear modal frequencies, normalized nonlinear mode shapes and damping coefficients, can be identified. For the damping quantification, the nonlinear or the projected linear approach can be used or, alternatively, the linear modal damping identified with the EMA can be included in the nonlinear model. The linear and nonlinear modal parameters can directly be used as a predictive model and are validated based on the training data for which they are extracted. This numerical model is specifically valid for steady-state FRF prediction, as indicated in Fig. 5.1. Using the nonlinear modal model, the nonlinear contribution to the FRF can be calculated according to Eq. (5.2), i.e., a model prediction is obtained. This nonlinear contribution is, according to
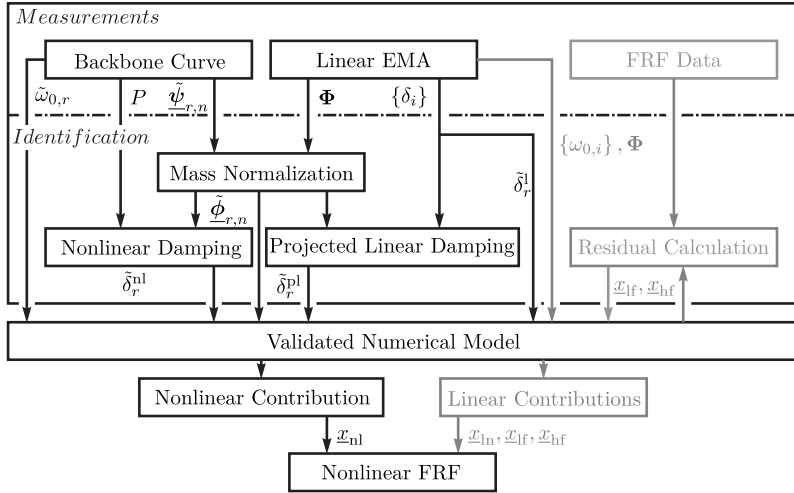
Figure 5.1: Gray-Box identification process (black: mandatory steps, gray: optional steps).

the single nonlinear mode assumption, sufficient to approximate the FRF in the close vicinity of an isolated nonlinear mode. To extend the range of validity of the model, additional linear modes can be taken into account using Eq. (5.4), based on the assumption that a linear superposition can be used in the low amplitude range further away from resonance. The linear contribution is based on the EMA, such that no additional measurement effort is required.

For a further improvement of the FRF in the frequency range far away from resonance, it is possible to identify the residual flexibilities modeled as shown Eq. (5.5) and Eq. (5.6). To this end, a set of measured FRF data is considered and the difference to the predicted FRF at the low and high end of the considered frequency range is minimized by suitable parameters for the residual flexibility. In this context, it is assumed that the system behaves essentially linear at the beginning and end of the considered frequency interval. Therefore, it is also possible to use an FRF extracted in the process of the linear EMA for this purpose. In experiments the residual flexibility has a higher relevance than in numerical studies using similar

concepts for FRF calculation. Firstly, the number of extracted modes is typically limited in EMA, whereas the extraction of additional linear modes does not present any difficulty in numerical studies. Secondly, the residual flexibility can be used to account for imperfect boundary conditions or local flexibility at the excitation point, which have an influence on the measured FRFs but are difficult to include in a modal model (Ewins, 2000).

Numerical Example

To briefly illustrate the influence of the linear modes and the chosen damping hypothesis, the numerical example detailed in Section 4.3 is revisited. In Section 4.3, it has not been possible to validate the extracted damping parameters with a reference solution, because the damping has not been included in the numerical calculation of the autonomous system. Therefore, the influence of the damping model on the FRF calculated with the gray-box approach is considered here. To this end, the nonlinear modal parameters, which have been extracted for an excitation at point two including the shaker model, are used (c.f. Section 4.3). In Fig. 5.2(a) the reference FRF for the drive point, calculated with the HBM with nine harmonics, for a sinusoidal excitation at node two with $f_{\mathrm{ex},1} = 0.3$ N is plotted in blue. The synthesized FRF around the first nonlinear mode with the nonlinear (green), the projected linear (red) and the linear damping model (black, dashed) are shown for comparison[1]. It can be seen that for the considered excitation level, the curves obtained with the linear and the nonlinear damping measure almost overlay each other. However, both damping measures seem to overestimate the damping leading to a slight deviation in the maximum amplitude compared to the reference solution. In contrast, the projected linear damping estimate yields almost the same result as the reference solution.

Next, the influence of the linear contribution of the remaining modes is demonstrated in Fig. 5.2(b). To this end, the reference FRF is plotted in a frequency range from 10 to 60 Hz (blue) and compared to the FRF calculated with the single nonlinear mode assumption (black, dashed) and the single nonlinear mode assumption with the additional linear contribution (red, dashed). The results clearly show that the influence of the remaining linear modes is negligible in the close vicinity of the resonance, where all three curves almost perfectly overlay, whereas the influence increases further away from resonance. In particular, the antiresonance at a

---

[1]The amplitude dependent damping coefficients can be found Fig. 4.11(a).
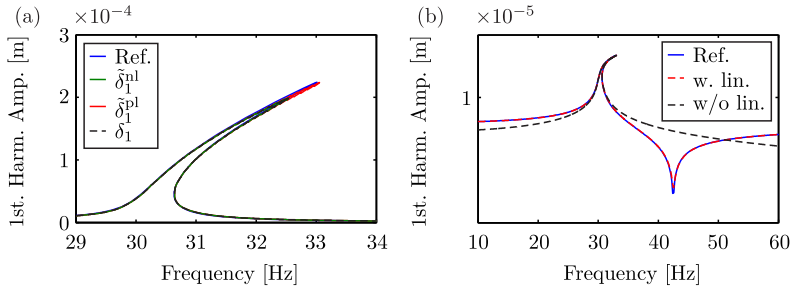
Figure 5.2: Comparison of reference FRF with FRFs calculated with linear, projected linear and nonlinear damping measure (a) and calculated FRF (log scale) with and without the influence of the remaining linear modes (b).

frequency of around 42 Hz cannot be captured with a single mode model. Furthermore, it is noted that in the frequency range away from resonance the amplitudes are generally small and the system can be represented accurately by a linearized model. This can be easily verified during the gray-box FRF calculation, as it is known which data point of the backbone curve is used for the calculation of each point of the FRF.

5.2 Analytical-Experimental Approach in Mixed-Modal-Physical Coordinates

The second identification method exploits the analytically derived frequency domain representation of the nonlinear forces using the HBM together with a linear modal model of the linear structure. The frequency domain representation of the autonomous conservative system is derived with the HBM yielding Eq. (3.26) which can be written in complex notation and split into blocks for each harmonic n yielding

$$\underline{\mathbf{H}}_n(n\omega)\underline{\boldsymbol{x}}_n + \underline{\boldsymbol{f}}_{\mathrm{nl},n}(\underline{\boldsymbol{x}},\omega) = \mathbf{0}, \ \forall n. \tag{5.8}$$

As explained in Chapter 4.1.1, these equations have to be fulfilled in the case of a nonlinear modal motion in the r-th nonlinear mode, i.e.,

$$\underline{\mathbf{H}}_n(n\tilde{\omega}_{0,r})\underline{\tilde{\boldsymbol{\psi}}}_{r,n} + \underline{\boldsymbol{f}}_{\mathrm{nl},n}(\underline{\tilde{\boldsymbol{\psi}}}_r, \tilde{\omega}_{0,r}) \overset{!}{=} \mathbf{0}, \; \forall n, \tag{5.9}$$

where $\tilde{\omega}_{0,r}$ denotes the nonlinear modal frequency and $\underline{\tilde{\boldsymbol{\psi}}}_r$ the nonlinear modal deflection shapes including all harmonic components. It is now assumed that $\tilde{\omega}_{0,r}$ and $\underline{\tilde{\boldsymbol{\psi}}}_r$ are known from the NEMA measurement, whereas the system matrices included in $\underline{\mathbf{H}}_n$ and the nonlinear forces $\underline{\boldsymbol{f}}_{\mathrm{nl},n}$ are unknown. If the linear modal parameters of the structure are known from an EMA measurement, then Eq. (5.9) can be written in linear modal coordinates (c.f. Eq. (4.12)) with the nonlinear mode shape described in linear modal coordinates (c.f. Eq. (4.56)) yielding

$$\left(-n^2\tilde{\omega}_{0,r}^2\mathbf{I}_{N_i} + \boldsymbol{\Omega}_0\right)\boldsymbol{\Phi}^+\underline{\tilde{\boldsymbol{\psi}}}_{r,n} + \boldsymbol{\Phi}^{\mathrm{T}}\underline{\boldsymbol{f}}_{\mathrm{nl},n}(\underline{\tilde{\boldsymbol{\psi}}}_r, \tilde{\omega}_{0,r}) = \mathbf{0}, \; \forall n, \tag{5.10}$$

where the nonlinear force law is kept in physical coordinates. Now, the only remaining unknown part in the equation is the nonlinear force law $\underline{\boldsymbol{f}}_{\mathrm{nl}}$ in the frequency domain. However, it is shown in Chapter 3 that for a class of nonlinear functions an analytical frequency domain representation of the nonlinear forces can be derived using the HBM (c.f. Tab. 3.1). The analytical form of the nonlinear force can then be evaluated for the measured $\tilde{\omega}_{0,r}$ and $\underline{\tilde{\boldsymbol{\psi}}}_r$ and Eq. (5.10) is solved for the parameter of the nonlinear force κ.

The analytical-experimental method is a rather simple procedure to quantify the nonlinearity. The method requires a linear modal model derived by a linear EMA and nonlinear modal parameters derived by the NEMA. Generally, any other frequency domain measurement, e.g., FRF measurements, could be used as training data. However, the advantage of the NEMA data is that it does not require an estimate of the damping properties of the linearized system, which is beneficial because the damping quantification is the most susceptible to errors in the process of EMA. Furthermore, it is noted that the analytical-experimental method requires some a priori knowledge of the functional form of the nonlinear forces and their locations as well as the analytical frequency domain representations of the nonlinear force laws.

5.3 White-Box Model Updating in Physical Coordinates

The third identification strategy is based on a minimization of the difference between the numerically calculated nonlinear modes obtained with the algorithm described in Chapter 3 and the experimental results obtained with the method described in Chapter 4. Therefore, the numerical model is updated until it provides a satisfying representation of experimental reality. The use of model updating strategies for nonlinear system identification has recently received increasing attention (Noël and Kerschen, 2016), which may be attributed to the ongoing development of efficient numerical methods. Generally, different experimental features and the corresponding numerical methods can be used for this purpose, such as nonlinear FRFs (Meyer and Link, 2003), proper orthogonal modes (Lenaerts et al., 2001) or empirical modes (Kurt et al., 2015). A model updating strategy based on experimentally extracted nonlinear modal data is proposed in Peter et al. (2015), which forms the foundation of the approach described below. The use of nonlinear modes as a basis for model updating provides the advantage that they contain information about the linearized and nonlinear model in a very condensed and physically meaningful form. Moreover, the resonances of nonlinear systems, which are usually the most relevant operating points from a design perspective, are typically located in the vicinity of nonlinear modes. It is expected that a model identified based on nonlinear modal data provides a high accuracy for these important operating conditions.

For the numerical calculations which are required for the updating, the HBM algorithm proposed in Chapter 3 is used. In this context, the HBM particularly provides the advantage that the filtering property can be exploited to speed up numerical calculation of nonlinear modes. Since the measurements are made prior to the updating, it is known to which extent higher harmonics are relevant and whether internal resonances have been found in the energy range of interest. Therefore, the HBM ansatz can be tailored according to the specific problem before the updating to save computational cost. An additional advantage of the HBM method is that the results are calculated in the frequency domain and can, thus, directly be compared to the experimental results which are at hand in the frequency domain.
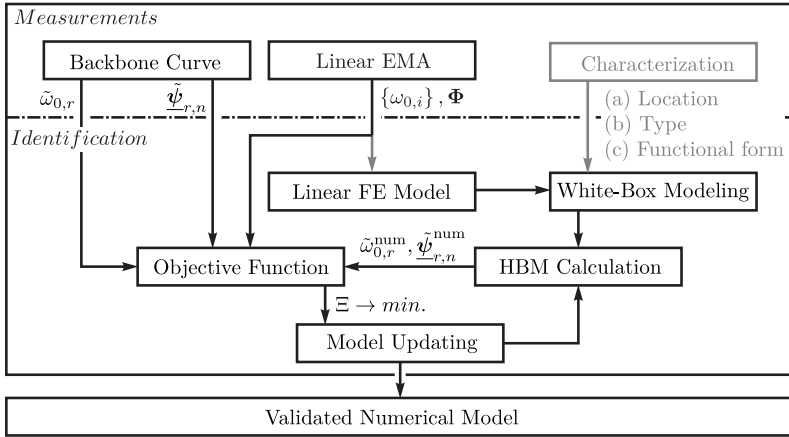
Figure 5.3: White-Box model updating process (black: mandatory steps, gray: optional steps).

A typical feature of model updating strategies is that some a priori model must be available as an initial guess for the updating process. This model can be either obtained by white-box modeling based on first principles, some preceded identification steps or a combination of both. It is acknowledged, that the choice of an appropriate initial model is anything but trivial for complex nonlinear systems and may require considerable expertise and experimental effort.

Process for White-Box Model Updating

The proposed model updating procedure is visualized in Fig. 5.3. Similarly to the other approaches, the model updating method relies on a backbone curve measurement and a linear EMA. The identification process is based on an a priori white-box model of the structure. This white-box model comprises a linear structure, which is modeled by finite elements, and some estimate of the character of the relevant nonlinear elements. Optionally, the linear FE model can be tuned with the results obtained from the linear EMA, i.e., a pre-optimization of the linear model with well-known linear model updating methods can be performed. In cases where the character of the nonlinear elements cannot be estimated by physical considerations,

their location and functional form can be estimated by some a priori characterization step. For instance, the RFSM can be used as a simple and effective method for characterizing the nonlinear elements.

The initial white-box model is then used for numerical simulation of a nonlinear mode of interest r using the HBM algorithm. The accordance of the numerical and the experimental results is evaluated using some objective function. Additionally, the linear modal parameters extracted by the EMA and numerical simulation can be included in the objective function. The objective function is minimized by an optimization algorithm through updating of the numerical model until convergence is achieved and a validated numerical model is at hand. The choice of the objective function and the optimization algorithm for the updating is briefly discussed in the following.

Objective Function

Linear model updating is, in most cases, based on the deviation of linear modal parameters of the experimental structure and the numerical model. For instance, the squared relative error of the linear eigenfrequencies

$$\Xi_{\mathrm{ln}}(\boldsymbol{\alpha}_{\mathrm{ln}}) = \sum_{i=1}^{N_i} \frac{\left(\omega_{0,i}^{\mathrm{exp}} - \omega_{0,i}^{\mathrm{num}}(\boldsymbol{\alpha}_{\mathrm{ln}})\right)^2}{\left(\omega_{0,i}^{\mathrm{exp}}\right)^2} \tag{5.11}$$

of N_i extracted modes can be minimized to identify the unknown parameters of the linearized model included in the parameter vector $\boldsymbol{\alpha}_{\mathrm{ln}}$. Additionally, the MAC value of the linear modes can be evaluated to verify the accordance of the experimental and numerical mode shapes (Allemang, 2002). These methods can be used for a pre-optimization of the linearized model.

A direct extension of these methods for the nonlinear updating is infeasible due to several reasons. First, the nonlinear eigenfrequencies as well as mode shapes may be energy dependent, such that the frequency difference and accordance of the mode shapes also depend on the energy. Second, the extraction of nonlinear modes involves higher experimental cost such that typically only a very limited number of experimental nonlinear modes is known. Therefore, in the following a few possible objective functions based on the amplitude dependent modal parameters of a measured nonlinear mode r are discussed.

A straightforward objective function, which has been used in Peter et al. (2015), is based on the squared difference of the numerical and experimental amplitude-frequency relation for a reference coordinate x_{ref} (or multiple reference coordinates) of the structure, i.e.,

$$\Xi_1(\boldsymbol{\kappa}) = \sum_{m=1}^{N_m} \left(\tilde{\omega}_{0,r,m}^{\text{exp}}(x_{\text{ref}}) - \tilde{\omega}_{0,r,m}^{\text{num}}(x_{\text{ref}}, \boldsymbol{\kappa}) \right)^2, \tag{5.12}$$

which is evaluated at N_m measured data points[2]. Herein, $\boldsymbol{\kappa}$ denotes the vector of unknown parameters of the nonlinear functions and may also contain additional unknown linear parameters of the model. It should be noted, that the choice of the reference coordinate is generally not obvious and depends on the system as well as the considered mode. Therefore, either multiple reference coordinates can be used (c.f. Peter et al. (2015)) or the minimization can be performed in the nonlinear modal domain, i.e., based on the relation of the nonlinear modal amplitude $\tilde{q}_r$ of the r-th mode and the associated nonlinear modal frequency. Then the entire nonlinear mode shape is inherently included in the normalization procedure of the mode shape (c.f. Eq. (4.46)). The objective function can then be chosen as

$$\Xi_2(\boldsymbol{\kappa}) = \sum_{m=1}^{N_m} \left(\tilde{\omega}_{0,r,m}^{\text{exp}}(\tilde{q}_{r,m}) - \tilde{\omega}_{0,r,m}^{\text{num}}(\tilde{q}_{r,m}, \boldsymbol{\kappa}) \right)^2, \tag{5.13}$$

which is minimized to obtain the parameter vector $\boldsymbol{\kappa}$. Generally, it is possible to take into account several nonlinear modes for the model updating. However, the practical examples in this thesis are limited to data of a single nonlinear mode. Moreover, it may be useful to simultaneously identify some of the linear parameters included in $\boldsymbol{\alpha}_{\text{ln}}$ and the nonlinear parameters included in $\boldsymbol{\kappa}$. To this end, the linear and nonlinear objective functions can be combined using a weighted summation, e.g.,

$$\Xi(\boldsymbol{\alpha}_{\text{ln}}, \boldsymbol{\kappa}) = \frac{\Xi_2(\boldsymbol{\kappa}) + \iota \Xi_{\text{ln}}(\boldsymbol{\alpha}_{\text{ln}})}{1 + \iota}, \tag{5.14}$$

where ι denotes the weighting factor. Finally, it is noted that the suitability of the objective function for the model updating strategy depends on the

---

[2]The numerical results can be easily interpolated to fit the amplitudes of measured data points.

specific problem and is influenced by several factors, e.g., the number of unknown parameters, the accuracy of the a priori linear model and the availability of experimental data, i.e., the number of extracted linear and nonlinear modes.

Optimization Algorithm

The linear and nonlinear parameters of the structure are identified by minimization of the objective function, i.e.,

$$\Xi \to \min. \tag{5.15}$$

For complex nonlinear systems, the dependence of the objective function on the parameter vectors is generally not known in closed form, such that the minimization has to be performed numerically. Furthermore, the optimization problem may be highly nonlinear and the gradients of the objective function are also unknown. Particularly, for cases in which multiple parameters are unknown the objective function is likely to have local minima. Even though it has been demonstrated in Peter et al. (2015) that for a simple benchmark structure a standard Nelder-Mead-Simplex algorithm implemented in MATLAB can be sufficient for this purpose[3], the HBM algorithm is integrated in the optimization software HYPERSTUDY in this thesis. This implementation allows for a greater flexibility regarding the optimization algorithm. For instance, problems which are likely to cause local minima in the objective function can be solved with globally convergent optimization methods such as genetic algorithms, whereas local methods such as the adaptive response surface method allow for an efficient optimization with a limited number of function evaluations, which is beneficial in cases where the numerical computation of nonlinear modes is expensive. Moreover, parallelization of function evaluations, combinations of several optimization algorithms or a pre-optimization of a linear FE model can be used without additional programming effort. Since the choice of the most efficient updating algorithm is highly dependent on the system which is to be identified, this thesis refrains from recommending a best possible updating algorithm for all conceivable identification problems.

---

[3]It has been observed that local minima may be reached in this case depending on the configuration of the optimization problem, i.e., start values, unknown parameters, objective function.

5.4 Discussion of the Identification Approaches

The aforementioned methods for system identification based on nonlinear modes have a fundamentally different scope and therefore pursue different strategies. The gray-box approach presented in Section 5.1 yields a model with a limited range of validity and several a priori assumptions have to be made. The parameters of the model are obtained in the nonlinear modal domain and are not directly related to physical parameters of the nonlinear forces. Apart from these limitations the approach is very easy to implement and neither requires the modeling of a linearized model nor the characterization and quantification of nonlinear forces. Furthermore, the numerical effort for vibration prediction is kept at a minimum, because the derived model is a single DOF representation of the system, i.e., the approach directly yields a reduced order model.

In contrast to the gray-box approach the analytical-experimental method in Section 5.2 requires some a priori knowledge of the character and location of the nonlinear forces. The method is by concept limited to nonlinearities which allow for an analytical calculation of the nonlinear forces in the frequency domain. Moreover, the estimation of the nonlinear coefficients may be complicated for complex structures with multiple nonlinear elements. The advantage of the method lies in its simplicity and the fact that the physical parameters of the nonlinear forces are obtained. Therefore, the parameters can be included in any numerical model, which can then be used for vibration prediction in an appropriate operating range.

Compared to the other approaches the modeling effort is much higher for the white-box based model updating strategy proposed in Section 5.3. Additionally, the approach is more expensive from a computational point of view. However, the method is very general and can be customized to nearly arbitrary structures with generic nonlinearities. Even the treatment of sophisticated models with complicated nonlinear modal dynamics, such as internally resonant or close nonlinear modes does not seem to be an issue from an identification point of view. Yet, it is noted that, in this case, considerable computational resources may be required and the measurement of the nonlinear modes of such structures seems to be difficult at present. Finally, the derived model can be used for the prediction of any vibration state in the operating range in which the model has been identified, given that the model structure is chosen correctly.

The proposed identification methods provide a toolbox for the derivation of predictive models. The suitable identification strategy has to be chosen depending on the specific problem.

5.5 Summary

The identification of predictive models based on NEMA has been discussed. Three novel strategies for the use of nonlinear modes in system identification are proposed:

- A gray-box strategy, which is based on an extension of the single nonlinear mode method, is presented. For the first time, the issue of direct prediction of different vibration states, i.e., steady-state FRFs of the forced and damped system, based on experimentally derived nonlinear modes is addressed.

- An analytical-experimental strategy in mixed-modal physical coordinates is presented. The method exploits analytical HBM formulations of nonlinear force laws in the frequency domain for a direct nonlinearity quantification. The use of nonlinear modes as training data simplifies the identification as an experimental damping quantification becomes obsolete.

- The first model updating strategy based on measured nonlinear modes is proposed. The white-box model based framework is build upon the integration of experimentally derived nonlinear modes with efficient HBM calculations in an optimization process.

The strategies will be illustrated with the help of experimental application examples in the following chapter.

Chapter 6

Application Examples

In this chapter, several experimental application examples of the proposed methods are shown. In Section 6.1, a detailed study of the nonlinear modal testing and identification methods is carried out. The extendability to systems with nonsmooth nonlinearities is illustrated in Section 6.2. The example used in this section also sheds light on the applicability of the experimentally derived nonlinear modes for the purpose of numerical model validation. In contrast, Section 6.3 focuses on a purely experimental based approach applied to a system with nonconservative nonlinearity. Special emphasis in this example is put on damping quantification by NEMA. The contributions of the thesis to the field of experimental application of NEMA are summarized in Section 6.4.

6.1 Benchmark System: Beam with Geometric Nonlinearity

In this section, the applicability of the complete processes of NEMA based nonlinear system identification to a laboratory experiment is demonstrated. The section starts with a description of the used benchmark structure including the experimental setup and shows the results of the NEMA. Subsequently, the identification and validation of predictive models obtained with the methods discussed in Chapter 5 is shown. In the last part of the section, the verification of the models based on experimental data and numerical simulations is studied.

6.1.1 Test Rig and Experimental Results

The benchmark structure used in this section is similar to the so-called ECL-benchmark beam proposed by Thouverez (2003), which has been studied in various implementations by several researchers (Kerschen et al.,
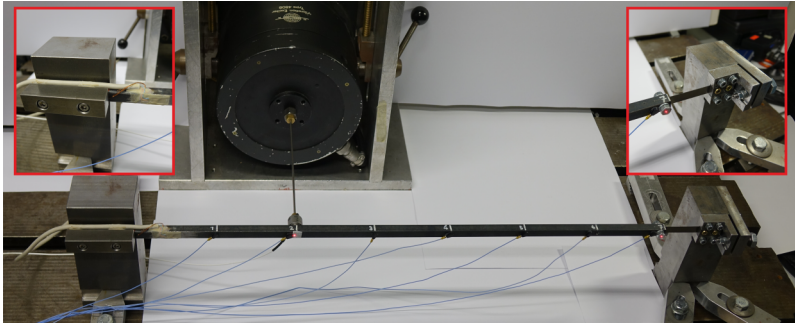
Figure 6.1: Photo of the beam test rig with close-up of the strain gauges for pretension measurement and the adjustable clamping mechanism of the thin beam.

2003; Meyer and Link, 2003; Shaw et al., 2016). The implementation used in this thesis is shown in Fig. 6.1. The setup consist of a long beam with square cross section that is clamped at one end and connected to a thin beam at the other end, which is also clamped. In the specimen used in this thesis, the clamping mechanism of the small beam can be moved to adjust the pretension of the setup, which can be measured by strain gauges attached to the long beam. The mechanism is primarily used to avoid buckling in the small beam, which may be caused by thermal expansion during testing. The long beam is excited by an electrodynamic shaker and the response is measured with seven accelerometers along the beam. Moreover, the displacement and velocity are recorded with laser Doppler vibrometers (LDVs) at the excitation point and the beam tip. The displacement and force at the excitation point are used as input signals for the PLL controller[1]. A schematic sketch of the setup is shown in Fig. 6.2(a)[2].

In this benchmark test, the beam is excited in its first bending mode leading to large deflections at the beam tip. This deflection causes a severe deformation of the thin beam compared to its thickness leading to a significant geometric stiffening nonlinearity. The nonlinear component of

---

[1]It is noted that the velocity or acceleration can also be used (see e.g., Peter and Leine (2017)) but the displacement is typically less distorted by higher harmonics increasing the accuracy of the phase control.

[2]Details about the instrumentation and the PLL parameters are included in Appendices H and G, respectively.
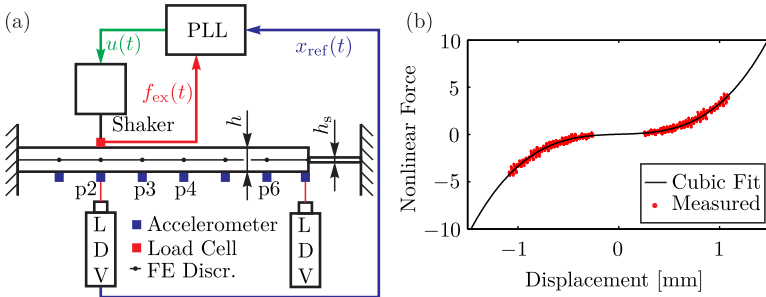
Figure 6.2: Schematic sketch of the experiment for excitation at point two with
FE discretization of the numerical model (a) and measured dimen-
sionless nonlinear force at the beam tip with cubic fit (b).

the nondimensional restoring force is shown in Fig. 6.2(b)[3]. Comparison
of the measured values with a cubic polynomial shows that the restoring
force of the small beam in lateral direction can indeed be modeled by a
cubic spring, as it is commonly done in literature.

For all NEMA based identification methods, which are discussed in the
following, the linear modes of the beam and the first fundamental nonlinear
mode are used. The first six linear bending modes, which are extracted
using a standard EMA with random excitation at point p2[4], are shown
in Tab. 6.1 along with the dimensions and nominal physical parameters of
the primary beam. For the extraction of the nonlinear modal parameters,
the beam is excited at point p2 and point p6, respectively, to investigate
the influence of the excitation point. The extraction of the nonlinear mode
is started at a low excitation level which is incrementally increased, mea-
suring in total 36 points of the backbone curve. The measured frequency-
amplitude curves for both excitation points are shown in Fig. 6.3(a). It
can be seen that the structure shows a significant stiffening nonlinearity
and the backbone curves extracted at both excitation points are very sim-
ilar. A small deviation may be attributed to a change in mass distribution
and stiffness due to the attachment of the shaker and stinger at different

---

[3]The RFSM has been used to characterize the restoring force at the beam tip. For
the purpose of visualization the linear component of the RFSM has been removed.

[4]For details of the EMA setup the reader is referred to Appendix H.

Frequency [Hz]	Damping [%]	Parameter	Value	Unit
30.05	0.21	E_{nom}	185	GPA
124.58	0.10	ρ	7830	kg/m^3
331.89	1.36	h	12	mm
663.85	0.10	h_{s}	0.5	mm
1106.09	0.15	l	700	mm
1576.56	0.43			

Table 6.1: Linear eigenfrequencies and modal damping ratios of the first six bend-
ing modes of the beam (left) and nominal parameters of the beam
(right).

points of the structure. The measured modal damping extracted with the
linear, projected linear and nonlinear modal damping hypothesis is shown
in Fig. 6.3(b) for both excitation points. It can be observed that for both
excitation points there is a significant deviation of the linear and projected
linear modal damping, which are both based on the EMA, compared to
the nonlinear modal damping measure. It is interesting to note, however,
that the deviation between the damping hypotheses is similar for both ex-
citation points in the low amplitude range. Furthermore, it can be seen
that the damping estimated with an excitation at point six is significantly
higher compared to the estimation for an excitation at point two. In the low
amplitude regime, this deviation is also approximately the same, indepen-
dently of the used damping hypothesis. For higher amplitudes, however,
the nonlinear modal damping coefficient estimated for an excitation at p6
approaches the nonlinear modal damping coefficient estimated for the ex-
citation at p2. A possible explanation for the discrepancies between the
excitation points is that the excitation forces applied at p6 are very small,
particularly for the measurements in the linear range, leading to a poor
signal to noise ratio which complicates an accurate measurement of the
excitation force for this point.

Additionally, the PBMIF for both excitation points in Fig. 6.4(a) indi-
cates that the excitation at point two yields a better mode isolation quality
than the excitation at point six, which is in line with the numerical study
of a similar test structure in Chapter 4.3. The PBMIF for both excita-
tion points suggests that there may be some imperfections with increasing
amplitude. It has been observed during experimentation, similarly to the
numerical study, that these imperfections are mainly due to harmonic dis-
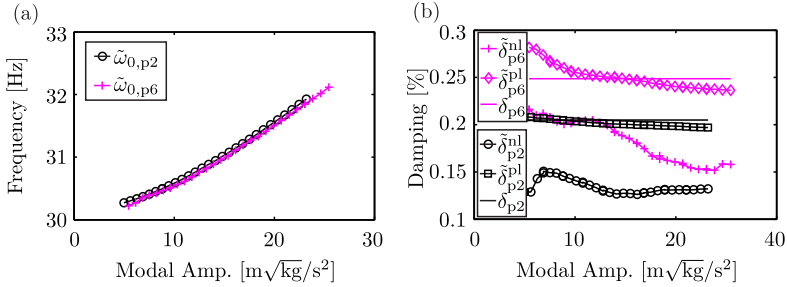
Figure 6.3: Frequency-amplitude plot (a) and damping-amplitude plot (b) for NEMA with excitation at point p2 and p6.

tortions in the excitation force[5]. Regarding the mode shapes shown in Fig. 6.4(b) it can be seen that the nonlinear modal motion is clearly dominated by the first linear mode. The second linear modal participation is increasing with increasing amplitude, however, its level is two orders of magnitude smaller compared to the first modal participation. Both excitation points yield similar results in this respect.

The experimental results show that the nonlinear modal parameters can be extracted with the proposed experimental procedure yielding the expected nonlinear stiffening behavior. It is further observed that the experiment can be performed with an excitation at different points of the structure. The nonlinear modal frequency and mode shape are similar for both excitation points, while the damping and mode isolation quality seems to be more sensitive. Since the mode isolation quality for an excitation at point two is, according to the PBMIF, better than for point six, the results for this excitation point are used for the following identification steps.

6.1.2 Identification and Validation of Numerical Models

In the next step, the predictive models are derived according to the three identification approaches presented in Chapter 5. For the gray-box approach, the nonlinear and linear modal parameters can directly be used

---

[5]A more detailed discussion of different power components is included in the publication Peter and Leine (2017).
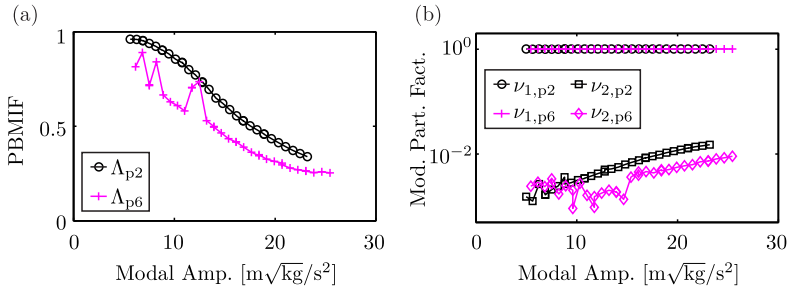
Figure 6.4: PBMIF over modal amplitude (a) and modal participation factor (b) for NEMA with excitation at point p2 and p6.

Parameter	Exp.-An.	Pre.-Opt.	Mod. Up.	Unit
E	n.a.	203	203	GPA
k_{c}	n.a.	4132.01	4202.17	N/m
k_{r}	n.a.	6.82	6.73	Nmm/rad
β	$871.91 \cdot 10^6$	n.a.	$828.75 \cdot 10^6$	N/m^3

Table 6.2: Identified parameters of the beam model obtained with analytical-experimental approach, linear pre-optimization and nonlinear model updating.

for building a predictive single nonlinear mode model, such that no further identification steps are required. The analytical-experimental method is applied using the linear modal data and assuming a cubic restoring force acting at the beam tip. Therefore, the only unknown parameter in the model is the cubic spring stiffness β. The analytical HBM formulation of the cubic spring force (c.f. Tab. 3.1) can then be used to calculate the parameter dependent nonlinear force, which is projected onto the linear modal space and has to be in balance with the linear modal forces (c.f. Eq. (5.10)). The equation is then solved for each measured data point to obtain the required nonlinear spring stiffness β.

For the model updating procedure, a physical FE model of the structure is required. Therefore, the main beam is modeled with seven Timo-

Pre-Optimization		Model Updating	
Frequency [Hz]	Error [%]	Frequency [Hz]	Error [%]
30.05	0.03	30.18	0.40
124.90	0.26	124.88	0.23
340.38	2.56	340.23	2.51
660.22	0.55	659.91	0.59
1082.21	2.16	1081.69	2.21
1573.17	0.21	1572.42	0.26

Table 6.3: First six linear bending eigenfrequencies of the beam and relative error after pre-optimization and nonlinear model updating.

shenko beam elements and the small beam is represented by a three parameter model with a linear translational and rotational spring with the stiffness parameters k_c and k_r, respectively, and a cubic spring (c.f. Chapter 4.3). Since all of these parameters are unknown and the nominal value of the Young's modulus of the main beam may also show some inaccuracy, the parameter vector for the white-box model updating is chosen as $\boldsymbol{\alpha} = [\beta, k_c, k_r, E]^{\mathrm{T}}$. The model updating is done in a two step process: (i) a linear pre-optimization and (ii) a nonlinear optimization. For step (i), the parameter vector $\boldsymbol{\alpha}_{\mathrm{ln}} = [k_c, k_r, E]^{\mathrm{T}}$ and the objective function is chosen according to Eq. (5.11). In step (ii), the difference between the numerical nonlinear modal amplitude-frequency curve to the experimental amplitude-frequency curve (c.f. Fig. 6.3(a), black curve) is minimized according to Eq. (5.13) to find the parameter β. Additionally, the design parameters k_c and k_r are varied within $\pm 10\%$ around the value obtained by the pre-optimization, leading to a parameter vector $\boldsymbol{\kappa} = [\beta, k_c, k_r]^{\mathrm{T}}$ for the nonlinear optimization. The variation of k_c and k_r is included to achieve a best possible estimate of the nonlinear modal results for the first mode, which may show some deviation to the natural frequency obtained by EMA due to experimental imperfections.

The obtained parameters for the analytical-experimental method, the pre-optimization and the nonlinear model updating are listed in Tab. 6.2. The pre-optimization and the nonlinear model updating yield similar parameters for the linearized model. The corresponding linear eigenfrequencies are listed in Tab. 6.3. The minor deviation to the experimental eigenfrequencies for all six bending modes indicates that the simplified model of
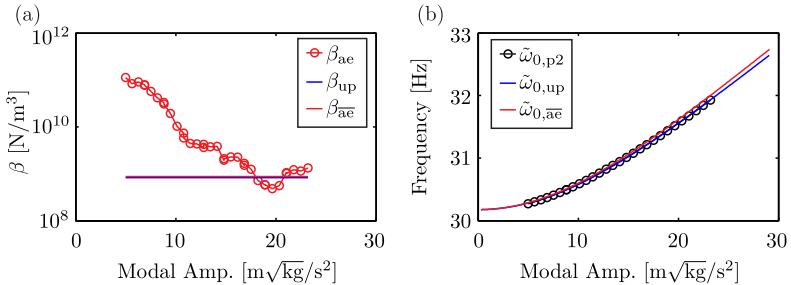
Figure 6.5: Cubic spring coefficient estimated with analytical-experimental method and model updating (a) and frequency-amplitude plot calculated with the identified parameters (b).

the small beam with two discrete linear stiffness parameters is sufficiently accurate. The most significant difference between both models is that the first eigenfrequency after the nonlinear model updating is slightly higher compared to the linear pre-optimization. This difference is mainly caused by the fact that the measured low amplitude frequency in the NEMA is slightly higher than in the EMA, which may be caused by the limited frequency resolution of the EMA or experimental imperfections.

The nonlinear model parameter β can either be estimated by the analytical-experimental method or the nonlinear model updating. The estimated parameter with the analytical-experimental method β_{ae} is plotted over the modal amplitude in Fig. 6.5(a). It can be seen that the obtained parameter is different for each measured data point, but stabilizes at around 10^9 for higher modal amplitudes. For comparison, the cubic spring constant obtained by the model updating β_{up} is shown. Particularly for low amplitudes, β_{ae} is significantly different to β_{up}, which can be attributed to the fact that the nonlinear forces in this amplitude range are very small which complicates the analytical-experimental estimation. In this amplitude range the parameter estimation is strongly biased by measurement errors and imperfections. Therefore, the obtained parameters for the last ten measured points of the backbone curve are averaged yielding the parameter $\beta_{\overline{ae}}$ shown in Fig. 6.5(a)(red line). This averaged parameter is similar to the parameter β_{up} (blue line) obtained with the updating method.
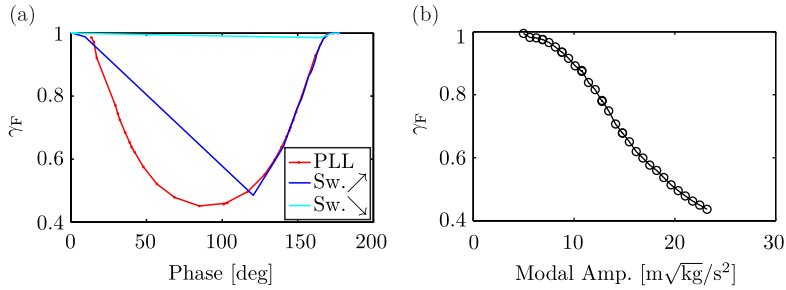
Figure 6.6: Fundamental harmonic content for FRF measurements (a) and NEMA measurement (b).

The frequency-amplitude curves of the updated nonlinear model and the model with $\beta_{\overline{ae}}$ are shown in Fig. 6.5(b). It can be seen that the model obtained by the white-box model updating almost perfectly represents the experimental data, whereas a small difference is observed if $\beta_{\overline{ae}}$ is used. Generally, it has been found that the analytical-experimental method is highly sensitive to imperfections in the linear modal model as well as experimental imperfections in the backbone curve test. The sensitivity may be reduced by including more training data, e.g., more nonlinear modes, into the analytical-experimental procedure but the robustness of the method seems to be limited. However, the simplicity of the analytical-experimental approach can, for instance, be exploited to estimate start values for nonlinear model updating.

6.1.3 Verification of the Identified Models

The last step of the identification process (c.f. Fig. 1.1) is the verification of the identified numerical models. To this end, two different sets of FRFs are considered. First, the calculated FRF using the identified gray-box model is compared to measured FRFs. Second, calculated FRFs using the updated white-box model are compared to calculated FRFs using the gray-box models obtained from NEMA with an excitation at the two different excitation points to investigate the consistency of the derived models.

For the first verification approach, a reference FRF measurement is required. Therefore, (i) a conventional sweep sine controller[6] and (ii) an augmented PLL controller[7] are used. For (i) slow sweeps with a sweep rate of 0.0125 Hz/s and two different sweep directions are used. This is necessary, because the Duffing-type behavior of the system leads to co-existing periodic solutions. The force level of $f_{\text{ex},1} = 0.45\text{N}$ is controlled based on the RMS value of the measured excitation force. The nonlinear feedback of the structure to the excitation mechanism leads to a significant distortion of the excitation force which can be quantified using the fundamental harmonic content (Shmilovitz, 2005)

$$\gamma_{\text{F}} = \sqrt{1 - \left(\frac{\sum_{n=2}^{N_h} f_{\text{ex},n}^2}{\sum_{n=1}^{N_h} f_{\text{ex},n}^2} \right)} \tag{6.1}$$

of the excitation force. A fundamental harmonic content $\gamma_{\text{F}} = 1$ indicates a purely sinusoidal force signal. The fundamental harmonic content for the FRF measurement is shown in Fig. 6.6(a) for the sweep up (Sw. ↗) and sweep down (Sw. ↘). It can be seen that the fundamental harmonic content of the excitation force significantly deviates from one, particularly near resonance. The measured amplitude and phase response with the conventional sweep controller are shown in Fig. 6.7(a) and (b), respectively. It can be observed that the characteristic jump occurs near resonance and the sweep up and down yield different branches of the FRF. Moreover, it can be seen that the jump for the sweep up occurs prior to the actual peak, which can also be seen in the phase response as the phase at which the jump occurs is below $90°$. Indeed, it is difficult to extract the complete branch of the FRF with a conventional sine controller due to the high sensitivity of the system near the bifurcation point. Therefore, a reference measurement with method (ii) is recorded. To this end, the PLL controller is augmented by a force amplitude control, which is also based on the RMS value of the measured excitation force. The PLL controller is capable of stabilizing the unstable branch of the FRF such that the complete FRF can be extracted. The measured FRF is shown in Fig. 6.7(a) and (b) and the fundamental harmonic content of the excitation force in Fig. 6.6(a). The force amplitude control based on the RMS value is generally more robust in the case of strong harmonic distortions compared to a control based

---

[6]The details of the experimental setup are included in Appendix H.
[7]The details of the PLL controller for FRF measurements are included in Appendix I.

on the fundamental harmonic, however, the distortions have to be taken into account in the FRF calculation to achieve comparable results to the reference measurement. Therefore, the fundamental harmonic content γ_F extracted in the NEMA (see Fig. 6.6(b)) is used as an amplitude dependent scaling factor of the excitation force in the FRF synthesis based on the gray-box model in Eq (5.2) yielding

$$[-\Omega^2 + 2i\Omega\tilde{\omega}_{0,r}\tilde{\delta}_r + \tilde{\omega}_{0,r}^2]\tilde{\underline{q}}_r = \gamma_F\tilde{\underline{\phi}}_{r,1}^H \boldsymbol{f}_{ex,1}. \tag{6.2}$$

Furthermore, the damping hypothesis has to be chosen for the FRF calculation. It is shown in Fig. 6.3(b) that the nonlinear damping coefficient is significantly lower compared to the linear and projected linear damping coefficient. However, it is expected that a phase resonance approach, as it is used for the measurement of the nonlinear mode, generally leads a more accurate damping measure compared to the conventional linear EMA using phase separation techniques (Géradin and Rixen, 2015). This hypothesis has been confirmed for the nonlinear case by the experimental study in Peter et al. (2018a). Thus, the nonlinear damping coefficient is used for the synthesized FRF. The comparison of the gray-box model based FRF with the directly measured FRFs for the beam tip in Fig. 6.7(a) and (b) shows a good agreement of the FRF measured with the PLL method and the synthesized FRF. There are small deviations around the peak and in the phase response which can be attributed to experimental imperfections. The comparison also reveals the difficulties to extract an accurate and complete FRF for a strongly nonlinear and lightly damped system with a conventional sine controller. Generally, it can be stated that the synthesized FRF yields a good representation of the frequency response around an isolated resonance and requires minimal experimental effort compared to the two reference measurements. The backbone curve measurement is a simple and robust technique compared to sine sweeps or the stepped phase FRF measurement with the PLL. The identification effort for the gray-box method is small and the numerical effort for the subsequent FRF calculation is negligible as the obtained model is a single DOF nonlinear modal oscillator.

The second study for verification of the derived models addresses the significance of the derived gray-box models for different excitation scenarios and a comparison of the updated white-box FE model with the gray-box model. To investigate the former, the FRF for an excitation at point p4 is synthesized with the gray-box models obtained for an excitation at point
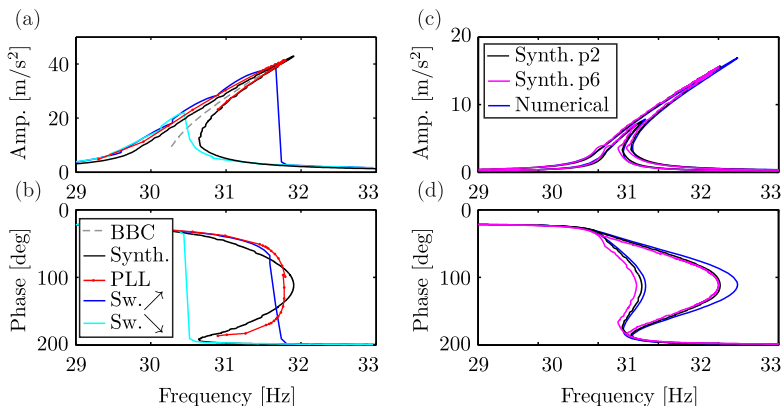
Figure 6.7: Calculated gray-box FRF for excitation at p2 and response at beam tip with reference measurements (a),(b) and comparison of gray-box model FRF with updated white-box model FRF for excitation at p4 and response at p3 with $f_{\mathrm{ex},1} = \{0.05, 0.1\}$N (c),(d).

p2 and point p6. To study the latter, the updated full FE model is used to calculate the FRF for an excitation at p4 with the HBM including nine harmonics and compared to the gray-box models[8]. The obtained amplitude and phase responses for two different excitation levels $f_{\mathrm{ex},1} = \{0.05, 0.1\}$N are shown in Fig. 6.7(c) and (d). It can be seen that the calculated FRF for an excitation at point p4 can be estimated based on gray-box models obtained with excitation at point p2 and p6, respectively. More importantly, both gray-box models yield very similar results indicating that the gray-box models are not limited to FRF predictions of the same excitation scenario as has been used as training data. The comparison of the gray-box model and white-box model FRF also shows a good agreement. There, is some deviation for the high excitation level which may be caused by imperfect mode isolation or additional nonlinear effects in the experiment which are not included in the white-box model.

---

[8]Here, the projected linear damping coefficient for the NEMA at p2 is used, as the damping coefficients obtained at both excitation points were significantly different. The projected linear damping hypothesis can be approximated in the HBM calculation by an appropriate Rayleigh damping.
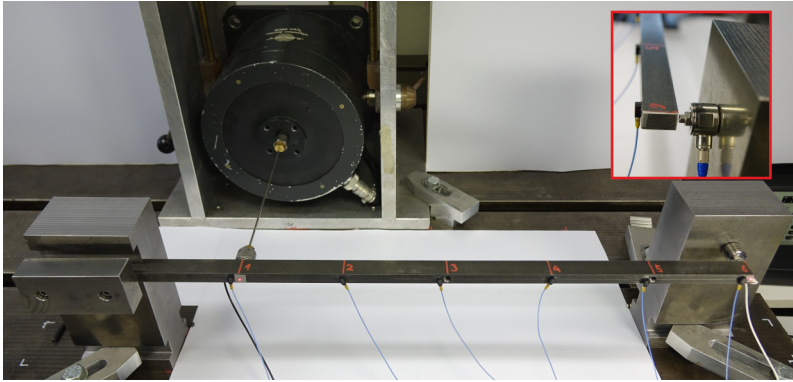
Figure 6.8: Photo of the beam test rig with close-up of the one-sided support element.

In conclusion, the verification of the derived models shows that the gray-box and white-box model updating strategy can be used to extract predictive models. The verification based on FRF data around resonance shows a good agreement with reference measurements and consistency of the derived models.

6.2 Extension to Nonsmooth Systems: Beam with Impact

In this section, it is demonstrated that the NEMA method can also be applied to systems subjected to nonsmooth nonlinearities. In this application example, the use of the NEMA method as a tool for model validation is shown. To this end, nonlinear modal parameters of a benchmark structure are measured and compared to predictions obtained by numerical simulations. Numerical results using two different numerical methods are considered: (i) the MSHBM introduced in Section 3.4 and (ii) the conventional HBM using a contact stiffness model. It is emphasized that the numerical models are derived independently of the NEMA, in case (i) based on first principles and in case (ii) based on measured time series. Therefore, the predictive accuracy of the derived models and the accordance of the experimental NEMA results with analytical results can be evaluated.

Frequency [Hz]	Damping [%]	Parameter	Value	Unit
40.10	0.19	E_{msh}	181.36	GPA
268.62	0.76	E_{hbm}	187.60	GPA
758.26	0.05	ρ	7730	kg/m^3
1371.82	0.17	h	20	mm
2427.72	0.10	b	12	mm
3508.31	0.14	l	600	mm

Table 6.4: Linear eigenfrequencies and modal damping ratios of the first six bending modes of the beam (left) and parameters of the numerical beam models (right).

The benchmark structure to which the methods are applied is a steel beam with rectangular cross section, clamped at one end, with a one-sided support at the beam tip. A photo of the used test rig with a magnification of the one-sided support is shown in Fig. 6.8. The one-sided support consists of a load cell which is mounted onto a rigid steel block and equipped with a steel cap serving as contact surface. The beam is excited using an electrodynamic shaker and the excitation force is recorded using a load cell. The response of the beam is measured with six accelerometers and two LDVs[9]. For the NEMA, the phase of the force with respect to the displacement at the excitation point is controlled with the PLL controller. A schematic sketch of the test setup is shown in Fig. 6.9(a). It has been observed during experimentation that the PLL method is robust in the case of the strong impulsive nonlinear force. It is remarkable that the tracking of the phase at the instant when the beam hits the support for the first time did not seem to present any difficulty. This is clearly in contrast to conventional sweep sine testing where the control of the force level is very difficult and sensitive on the controller settings at this point. Moreover, different excitation points and the influence of the parameters of the PLL have been investigated. It has been observed that the robustness and accuracy of the control increased with increasing distance from the contact point, which is why the results for an excitation at point one are presented here. The parameters of the PLL did not seem to have a significant influence on the robustness or the accuracy of the method[10].

---

[9]Details on the used equipment are included in Appendix H
[10]The parameters used for the presented results are included in Appendix G.
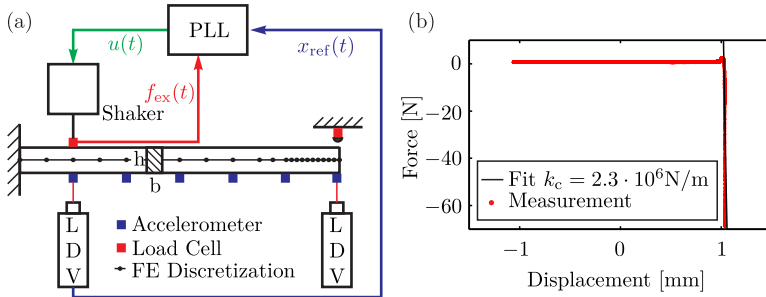
Figure 6.9: Schematic sketch of the experiment and numerical model (a) and measured contact force with linear fit (b).

The numerical model of the benchmark structure consists of 21 Timoshenko beam elements, i.e., 22 nodes with three DOFs each. The discretization, which is also symbolized in Fig. 6.9(a), is refined towards the beam end. The mesh is refined as the MSHBM uses a massless contact node and the influence of the mass redistribution is sought to be minimized. The parameters of the linear FE model are adjusted, such that the linear modes of the numerical model fit the linear modes of the experimental beam. To compensate the effect of the massless contact node the Young's modulus is slightly modified for the MSHBM, such that the linear eigenfrequencies for both approaches are approximately the same. The measured linear modes of the beam and the parameters used for the FE models are shown in Tab. 6.4. For the HBM approach, the one-sided support is modeled by a linear spring leading to a piecewise linear elastic restoring force at the contact node. This type of model requires a suitable stiffness parameter, which has to be identified experimentally. For the benchmark structure, this can be accomplished by analyzing a recorded time series during a measurement[11]. Since the contact force can directly be measured and the beam is modeled as one dimensional, i.e., the compression of the beam at the contact location is neglected, the contact force over the displacement at the beam tip can directly be extracted. The measured values are shown in Fig. 6.9(b). The contact stiffness of a purely elastic model of the one-sided support can be easily identified by fitting a linear function to the

---

[11]For the sake of simplicity the time data has been recorded during the PLL test.
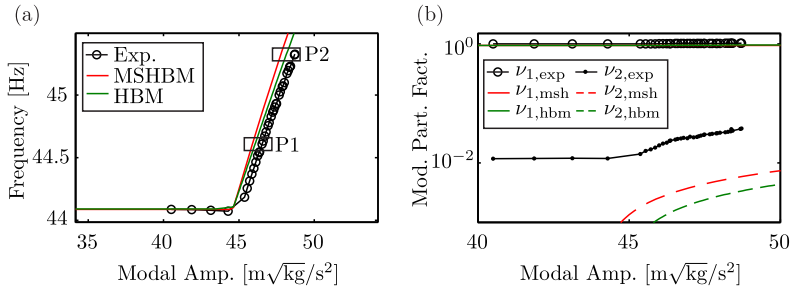
Figure 6.10: Frequency-amplitude plot for experimental and numerical (MSHBM and HBM) results of the first nonlinear mode (a) and modal participation factor of first and second linear modal coordinate (b).

measured values of the non-zero contact force. Using this procedure, a contact stiffness of $k_c = 2.3 \cdot 10^6 \text{N/m}$ is found which is then included in the HBM model. Both numerical calculations, i.e., the MSHBM and the HBM are carried out with five harmonics.

The experimental results as well as the results of the numerical calculations are shown in Fig. 6.10(a) in a frequency-amplitude representation. To this end, the results obtained for the acceleration are used to extract the nonlinear modal amplitude and the nonlinear modal frequency. The comparison of the frequency-amplitude curves shows that the experimental and numerical curves agree very well. It can be observed that the HBM method seems to be slightly closer to the experimental curve, whereas the MSHBM seems to predict a stiffer contact behavior. However, it is emphasized that the contact stiffness, which is required for the HBM, can only be measured in special cases like the present one. In most practical problems a direct measurement of the contact force is not feasible[12]. Moreover, the accuracy of the MSHBM can be increased by including an FE model of the one-sided support element rather than simply regarding the contact as a unilateral constraint.

The analysis of the mode shape is carried out by projecting the nonlinear mode shapes onto the linear mode shapes obtained by EMA (c.f.

---

[12]In this case the proposed model updating strategy (see Chapter 5) may be an alternative for the estimation of the contact parameters.

Section 4.3, Eq. (4.56)). The results for the modal participation factor of the first two modes[13] for the measurement as well as the simulations are shown in Fig. 6.10(b). It can be observed that the motion is dominated by the first linear modal coordinate. To be more precise, the change in mode shape due to the contact is comparatively small yielding a modal participation of the first mode of approximately one for both numerical methods as well as the experimental results. The contribution of the second linear mode is around two orders of magnitude smaller. It can be seen that for the experimental results the contribution of the second mode is generally larger, even before the impact is reached. This can be attributed to experimental imperfections. Once the impact is reached the course of the contributions of both numerical methods is qualitatively similar to the experimental results. However, it is noted that contribution predicted by the numerical simulations is smaller compared to the experiment. This can again be attributed to experimental imperfections but the limited number of considered harmonics in the simulation may also play a role. Further, it is interesting to note that, regarding the mode shapes, the MSHBM results seem to be closer to the experimental results compared to the HBM.

In Fig. 6.11 the motion of the beam is analyzed in more detail in the time domain. To this end, the displacement of the beam tip and the contact force is plotted for two exemplary points, which are indicated in Fig. 6.10(a). The time instant in which the beam hits the stop in the experiment is indicated by a red circle (Cont.) and the time instant in which the beam is separated from the stop by a green circle (Sep.). Furthermore, the position of the stop element is indicated by a blue line. It can be observed that the displacement of the beam tip at point P1 and P2 (Fig. 6.11(a) and (c)) are almost perfectly predicted by the MSHBM as well as by the HBM simulation. It is also interesting to note that the displacements appear to be approximately sinusoidal. This also explains why a comparatively rough approximation with five harmonics already yields a good representation of the system's response.

In Fig. 6.11(b) and (d) the time history of the contact forces are shown for both points. It can be observed that the HBM approximation cannot capture the impulsive character of the contact force leading to a significant broadening of the peak and an underestimation of the maximum contact force. In contrast, the contact force predicted by the MSHBM qualitatively

---

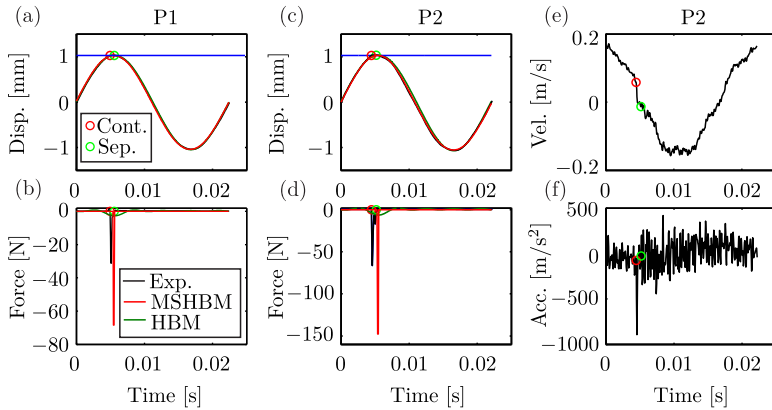[13]All other modal contributions were found to be negligible.

Figure 6.11: Time histories for the displacement (a) and contact force (b) for P1
            and time histories for displacement (c), contact force (d), velocity
            (e) and acceleration (f) for P2.

matches the measured contact force in the time domain[14]. The prediction
overestimates the maximum contact force by a factor of two indicating that
the contact behavior with the MSHBM is too stiff. It is also interesting
to note that for P2 the experimental contact force shows a small peak
next to the primary peak. It has been found that this peak is caused by
local high frequency vibrations in the contact element. Obviously, this
effect cannot be captured in simulations, where the contact element is not
explicitly modeled. Finally, it is noted that the contact instant in the
experiment seems to be slightly shifted compared to the simulations. This
may be caused by the discrete nature of the measured data, such that the
nearest periodic solution of the simulation has a slightly different frequency
compared to the experiment. Additionally, the contact time is very short
which is difficult to resolve experimentally even though high sampling rates
(20kHz) have been used.

In Fig. 6.11(e) and (f) the measured velocity and acceleration at the
beam tip are shown. These time histories reveal that, although the dis-

[14]Note, that the time domain solution for the contact force is subsequently approx-
imated by its Fourier transform for the calculation of the global dynamics of the
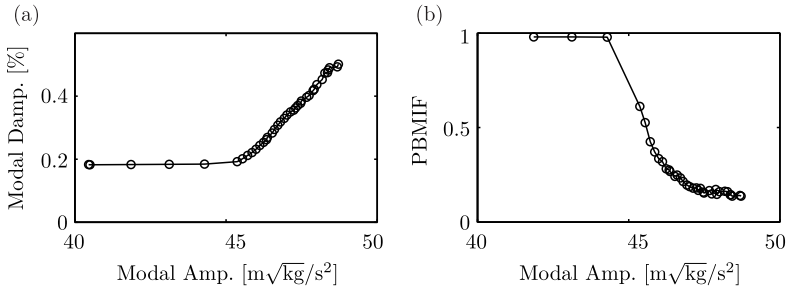system, which also leads to a similar smearing effect as in the HBM case.

Figure 6.12: Experimentally extracted amplitude dependent damping (a) and PB-MIF (b).

placement seemed to be approximately harmonic, the velocity and especially the acceleration show significant high frequency content. Obviously, these effects cannot be captured by the numerical solutions with five harmonics. The influence of these high frequency vibrations on the global behavior of the beam seems to be negligible. However, they may need to be considered in practical applications as they may lead to noise and fatigue.

The extracted nonlinear modal damping measure and the PBMIF are shown in Fig. 6.12. It can be seen that the effective damping in the structure in Fig. 6.12(a) shows a clear amplitude dependence and increases with amplitude. The damping measure is difficult to compare to numerical simulations, because damping is not included in the nonlinear mode definition used here. Moreover, it is noted that the numerical modeling of the damping mechanisms due to impacts is still an open question. However, it seems plausible that damping increases because of the impact, since the impact causes a energy transfer to higher frequencies where the vibration energy is then attenuated. Regarding the PBMIF in Fig. 6.12(b) it can be seen that the mode isolation quality significantly decreases when the impact is reached. This indicates that the single harmonic single point force may not be sufficient for an exact mode isolation. Particularly, high distortions in the excitation force and velocity may require the control of higher harmonic frequencies to increase the mode isolation quality. Remarkably,
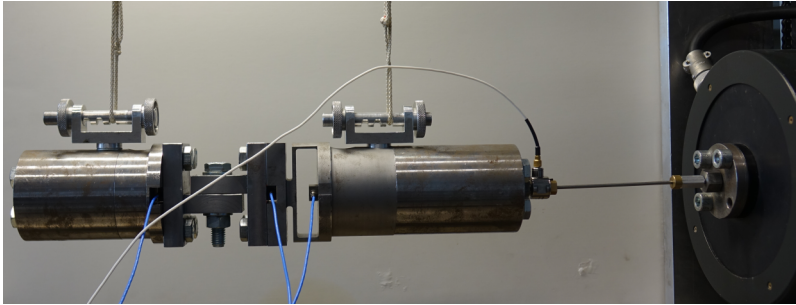
Figure 6.13: Photo of the joint resonator test rig.

despite these discrepancies, the measurements agree very well with the numerical calculation of the nonlinear modes.

6.3 Extension to Nonconservative Systems: Joint Resonator

This section addresses the applicability of the proposed NEMA method to nonlinearly damped systems in the framework of the extended periodic motion concept for nonconservative systems (c.f. Definition 2.3). As opposed to the previous examples no high fidelity numerical model of the test structure is available, such that the approach is purely experimental. This includes the NEMA measurement as well as the processes of model validation and verification, which are performed exclusively based on experimental data of reference measurements. Thereby, it is demonstrated that NEMA can be used to derive predictive models with minimal a priori knowledge of the structure under test and the nonlinear system identification process (c.f. Fig. 1.1) can be replaced by cost-efficient dark gray-box modeling. The body of the following example is published in Scheel et al. (2018b).

The test structure is a benchmark system for the characterization of bolted joints, which has originally been proposed by Bohlen (1987) and has subsequently been used in different implementations in numerous studies (Ehrlich, 2016; Gaul and Lenz, 1997; Segalman et al., 2009; Süß, 2016). The specimen used in this thesis, shown in Fig. 6.13, is borrowed from Ehrlich
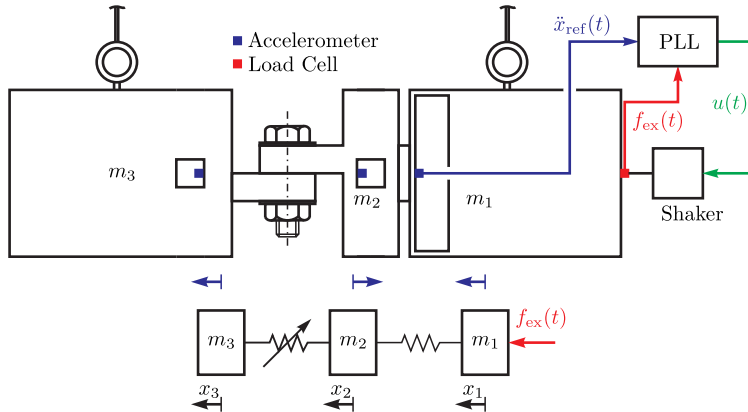
Figure 6.14: Schematic sketch of the experimental setup and minimal model with indicated mode shape of the first axial mode (blue arrows).

(2016). A salient feature of the benchmark system is that its axial dynamics can be accurately described by a chain of three lumped masses, two of which are connected with a bolted joint. A scheme of the experimental setup including a schematic sketch of the shape of the first axial linear mode is shown in Fig. 6.14. The masses m_1 and m_2 are connected by a leaf spring which can be represented by a linear model. The contact interface in the joint, connecting the masses m_2 and m_3, causes nonlinear stiffness and damping behavior due to friction (Bograd et al., 2011; Gaul and Nitsche, 2001). The structure is supported with cords yielding quasi-free boundary conditions and excited with an electrodynamic shaker at mass m_1. The excitation force is measured using a load cell and the response is measured by three accelerometers attached to each of the masses[15].

For the nonlinear modal test, the excitation force as well as the acceleration response at m_1 are fed into the PLL controller[16] of which the output is used to drive the shaker. The voltage is incrementally increased from low, starting from an approximately linear mode of operation, to a high level, where significant nonlinear behavior is expected. The extracted nonlinear modal frequency over modal amplitude is shown in Fig. 6.15(a). A

---

[15]Details on the used hardware are included in Appendix H

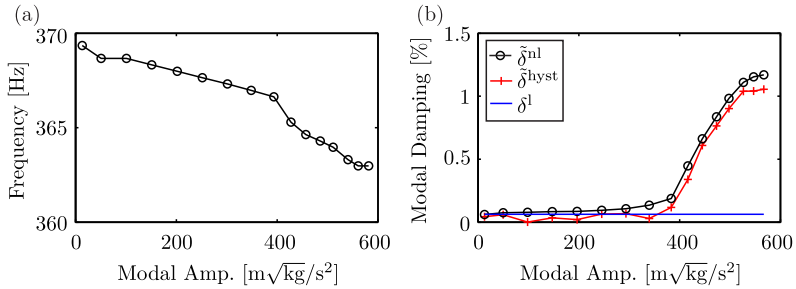[16]The parameters of the PLL controller are included in Appendix G.

Figure 6.15: Experimentally extracted amplitude dependent nonlinear modal frequency (a) and damping measures (b).

clear amplitude dependence of the nonlinear modal frequency can be observed indicating nonlinear behavior. Particularly at a modal amplitude of around 400 m$\sqrt{\text{kg}}$/s^2 a sharp bend in the frequency amplitude curve can be observed which is typical for the transition from mostly sticking to micro-slip behavior of the joint (Bograd et al., 2011; Gaul and Nitsche, 2001). This hypothesis is supported by the amplitude dependent nonlinear modal damping coefficient $\tilde{\delta}^{\text{nl}}$ shown in Fig. 6.15(b), which also shows a similar bend followed by a significant increase in modal damping at the same amplitude. The damping curve reveals that the nonlinearity due to sliding in the joint leads to a strong increase in damping by a factor of more than 20 compared to the linear modal damping δ^{l}. It is interesting to note that even for lower amplitudes, where linear behavior has been expected, a small softening characteristic and an increase in damping is indicated by the modal results. This behavior may be attributed to additional nonlinearities which are not included in the lumped mass model or imperfections in the experimental setup and excitation mechanism.

In Fig. 6.16(a) the PBMIF is plotted over modal amplitude. The PBMIF indicates a good mode isolation quality for the whole amplitude range. Interestingly, the mode isolation quality seems to be better in the nonlinear regime of motion, which may be caused by an increasing signal quality for
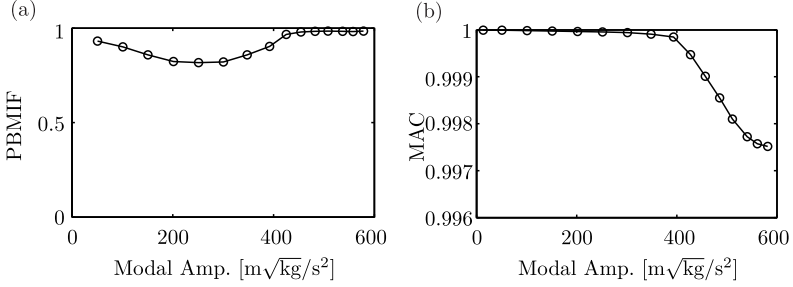
Figure 6.16: PBMIF (a) and MAC value of linear and nonlinear mode shape (b).

higher load levels. In Fig. 6.16(b) the Modal Assurance Criterion (MAC)

$$\text{MAC} = \frac{\left| \boldsymbol{\phi}_1^{\text{T}} \tilde{\boldsymbol{\phi}}_1 \right|^2}{\boldsymbol{\phi}_1^{\text{T}} \boldsymbol{\phi}_1 \tilde{\boldsymbol{\phi}}_1^{\text{H}} \tilde{\boldsymbol{\phi}}_1}, \tag{6.3}$$

between the linear and the nonlinear mode shape is shown. It can be observed that the correlation is very high indicating that the change in mode shape due to the nonlinearity is negligible. A small drop can be observed in the micro-slip regime, however, the MAC value remains close to unity.

In the following, the attention is drawn towards the validation of the experimental results. To be more precise, the extracted modal damping measure is validated against the damping measure extracted with the methods used in previous work on the joint resonator. An important feature of the joint resonator is that the only force acting on m_3 is the nonlinear force $f_{\text{nl}}(t)$ transmitted by the joint. Therefore, the balance of linear momentum

$$m_3 \ddot{x}_3(t) = f_{\text{nl}}(t), \tag{6.4}$$

can be used to calculate the nonlinear force, because the acceleration $\ddot{x}_3(t)$ is measured and the mass $m_3 = 4095$ g (estimated by weighing) is known. Furthermore, the relative displacement in the joint $x_{\text{rel}}(t) = x_3(t) - x_2(t)$ can be calculated by integration of the measured accelerations $\ddot{x}_2(t)$ and

$\ddot{x}_3(t)$ in the frequency domain. Then the nonlinear force over relative displacement in the joint is known. The measured nonlinear forces are shown in Fig. 6.17(a). It can be observed that the force in the joint for low relative displacements is almost linear. However, for increasing relative displacements, the nonlinear force forms a hysteresis loop of increasing size, which is the typical behavior for a frictional joint. The dissipated work per cycle can be calculated based on the area enclosed by these hysteresis loops, i.e.,

$$W_{\mathrm{diss}}^{\mathrm{hyst}} = \oint f_{\mathrm{nl}} \; \mathrm{d}x_{\mathrm{rel}}. \tag{6.5}$$

Using the dissipated work per cycle, an equivalent modal damping ratio of a periodic resonant vibration can be calculated as (Bograd et al., 2011; Ungar, 1962)

$$\tilde{\delta}^{\mathrm{hyst}} = \frac{W_{\mathrm{diss}}^{\mathrm{hyst}}}{4\pi E_{\mathrm{pot}}^{\mathrm{max}}}, \tag{6.6}$$

where $E_{\mathrm{pot}}^{\mathrm{max}}$ denotes the maximum potential energy in the structure

$$E_{\mathrm{pot}}^{\mathrm{max}} = \int_0^{x_{\mathrm{rel,max}}} f_{\mathrm{nl}} \; \mathrm{d}x_{\mathrm{rel}} + \int_0^{x_{\mathrm{k,max}}} f_{\mathrm{k}} \; \mathrm{d}x_{\mathrm{k}}. \tag{6.7}$$

The maximum potential energy can be calculated under the assumption that the oscillator approximately moves in unison, such that the maximum displacements in the joint, i.e., $x_{\mathrm{rel,max}} = x_{\mathrm{rel}}(t^*)$ and the leaf spring, i.e., $x_{\mathrm{k,max}} = x_{\mathrm{k}}(t^*) = x_2(t^*) - x_1(t^*)$, are reached at the same time t^*. Herein, the force in the leaf spring can be obtained by the balance of linear momentum for the first mass

$$f_{\mathrm{k}}(t) = m_1 \ddot{x}_1(t) - f_{\mathrm{ex}}(t) \tag{6.8}$$

with $m_1 = 5300$ g. The obtained damping measure $\tilde{\delta}^{\mathrm{hyst}}$ and the nonlinear modal damping measure $\tilde{\delta}^{\mathrm{nl}}$ are plotted in Fig. 6.15(b) for validation. It can be observed that the nonlinear modal damping measure yields very similar results compared to the hysteresis based damping measure. The modal damping measure $\tilde{\delta}^{\mathrm{nl}}$ is slightly higher which can be attributed to the fact that $\tilde{\delta}^{\mathrm{nl}}$ includes the global damping behavior of the structure whereas $\tilde{\delta}^{\mathrm{hyst}}$ only includes local damping effects in the joint. Therefore,
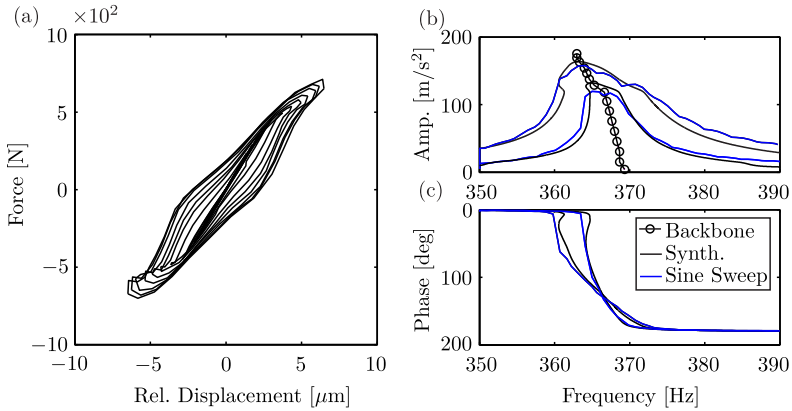
Figure 6.17: Measured hysteresis in the jointed connection (a), synthesized and measured amplitude (b) and phase (c) of the FRF.

additional sources of damping due to the other joints in the structure, material and aerodynamic damping are not included in $\tilde{\delta}^{\mathrm{hyst}}$. Finally, it is emphasized that $\tilde{\delta}^{\mathrm{hyst}}$ can be only extracted in the special case of a lumped mass system whereas $\tilde{\delta}^{\mathrm{nl}}$ can be extracted in the same way for more complex or continuous structures.

In the last part of this example, the experimental verification of the extracted nonlinear modal model is addressed. To this end, the identified gray-box model is used for the prediction of FRFs in the vicinity of the considered nonlinear mode which are then compared to measured FRFs. Two different levels of sinusoidal forcing, $f_{\mathrm{ex},1} = \{14.65, 38.15\}$ N are used to calculate the FRF using Eq. (5.2). Additionally, the contributions of low and high frequency residuals are superimposed (c.f. Eq. (5.7)) as no further linear modes have been extracted. The results of the synthesis are shown in Fig. 6.17(b) for the amplitude and in Fig. 6.17(c) for the phase response. The synthesized FRF is compared against the measured FRF for sine sweep measurements in a frequency range from 350 Hz to 390 Hz measured at a sweep rate of 0.2 Hz/s with the same excitation levels. It can be seen that the synthesized FRFs agree well with the directly measured FRFs. Some deviation can be seen around the peak that may be attributed to small

errors in the modal damping estimation or imperfections in controlling the force level during the sine sweeps, which have been observed during experimentation.

In conclusion, the example shows that the NEMA method can be readily used for nonlinearly damped structures based on ENMs. The experimental validation of the modal results and the verification of the gray-box model prediction shows that the results agree well to results obtained with well-known methods for similar benchmark structures. It is emphasized that NEMA is more generally applicable compared to the previous damping estimation method as well as faster and more robust compared to sine sweep measurements.

6.4 Summary

The applicability of NEMA for the identification of nonlinear dynamic structures is demonstrated in laboratory experiments. In particular, the following contributions are made:

- The robustness of the novel NEMA method in experimental situations is demonstrated.

- The capability of NEMA for the identification of predictive models is assessed by several validation and verification studies. Thereby, the significance of experimentally derived nonlinear modal parameters is addressed.

- Different potential fields of application of NEMA, such as the validation of numerical models or the purely experimental based prediction of vibration responses are illustrated.

- The examples in this chapter demonstrate the applicability of phase resonance testing to nonsmooth and nonlinearly damped systems for the very first time, revealing the potential of NEMA for such systems.

Chapter 7

Concluding Remarks

This chapter summarizes the main contributions made in this thesis, draws a conclusion and indicates directions of future research.

7.1 Summary of Contributions and Conclusion

This thesis proposes a novel framework for NEMA and discusses how nonlinear modes can be applied for nonlinear system identification. Therefore, several conceptual and practical issues of previous modal based approaches are addressed to drive the development towards a versatile nonlinear modal based identification strategy for complex nonlinear structures. In particular the following contributions are made:

- For the first time, NEMA has been embedded in a rigorous nonlinear system identification framework. Thereby, the various aspects included in a system identification process, such as numerical and experimental analysis as well as the connection of both fields, are organized in Chapter 1. The proposed framework gives a clear structure to the developments made in this thesis, but also simplifies the integration of new research in the individual disciplines involved in a system identification process.

- A numerical algorithm which particularly matches the requirements for nonlinear modal based system identification has been proposed in Chapter 3. The HBM based approach with the analytical calculation of the nonlinear forces in the frequency domain provides a high computational efficiency and direct insight in the frequency domain characteristics of nonlinear functions. It has been demonstrated that complex high fidelity models with many DOFs and several nonlinear elements can be treated with this algorithm.

- A novel theoretical framework for the experimental extraction of nonlinear modal parameters has been proposed in Chapter 4. It has been shown that the excitation power is a central quantity for the assessment of the nonlinear mode isolation quality and a new nonlinear mode indicator function, the PBMIF, has been proposed. Furthermore, the extraction of nonlinear modal parameters which are consistent to linear theory has been addressed.

- In Chapter 4, additionally, a new method for the practical realization of an appropriate excitation force has been proposed. The PLL based approach outperforms the commonly used manual force appropriation methods in terms of robustness and accuracy. Moreover, the method can be easily automated.

- The open problem of identification of predictive models based on experimentally derived nonlinear modal parameters has been addressed in Chapter 5. Three different identification methods have been proposed: a gray-box approach in nonlinear modal domain, an analytical-experimental approach in mixed-modal-physical domain and a white-box model updating strategy. The three approaches provide a toolbox from which the suitable method can be selected based on the specific identification problem.

- The application of NEMA to the identification of nonlinear structures has been illustrated with several laboratory experiments in Chapter 6. A thorough discussion of the validation and verification of the derived predictive models has shed light on the significance of experimentally extracted nonlinear modal parameters, which is an issue that has hitherto rarely been discussed.

- In this thesis, for the first time, the applicability of nonlinear modal testing to systems with nonsmooth and nonlinearly damped structures has been addressed. The extendability of all aspects included in the proposed identification methodology to such systems has briefly been discussed. The experimental examples in Chapter 6 have shown that the methodology can be readily applied to benchmark systems with impacts and frictional joints.

The developments in this thesis show that NEMA is a promising concept for the identification of nonlinear structures. Particularly, the novel

framework for the experimental extraction of nonlinear modes, which is robust and easy to implement, marks an important step towards the identification of more complex structures and its potential for industrial applications. The integration in a rigorous nonlinear system identification framework, the combination with efficient numerical algorithms and the derivation of predictive models based on NEMA are also crucial steps in this respect. The thorough validation and verification of the derived models in the application examples has illuminated the significance of experimentally extracted nonlinear modal parameters. Another important step in the development of NEMA is the treatment of nonsmooth nonlinearities and nonlinear damping effects, due to their high practical relevance. The application examples in this thesis have revealed the potential of the proposed method to identify such structures.

7.2 Open Research Questions

There are still numerous open questions in the field of NEMA that need to be studied in future research. The influence of the mode isolation quality, which can be estimated with the PBMIF, on the extracted nonlinear modal parameters is not fully understood. The measured frequency-amplitude curves seem to be rather robust to imperfect mode isolation, while the influence on the damping estimation is more substantial. However, further numerical, theoretical and experimental work is required to confirm this hypothesis. Moreover, the influence of the optimal shaker position and a method for a priori estimation of the optimal excitation location requires further investigations. The test structures used in this thesis all have had in common that the change in the nonlinear mode shape over amplitude has been comparatively small. Therefore, the investigation of the robustness of NEMA to systems with stronger changes in mode shape requires additional research.

The framework presented in this thesis has been applied to rather academic test structures. The transfer to industrial scale applications is accompanied by several practical and theoretical issues. For such structures, as the one considered in the numerical example in Chapter 3.3, close modes and internal resonances are expected. Therefore, the measurement of internally resonant structures and structures with close modes has to be studied. It is expected that the experimental extraction of the nonlinear modes of such structures requires multiple excitation locations and mul-

tiple excitation frequencies. The realization of such excitation scenarios requires an extension of the proposed PLL controller. Furthermore, alternative control concepts, such as a direct velocity feedback, may provide an interesting alternative to realize the appropriated excitation. The applicability of the nonlinear modal based identification concepts to structures of higher complexity and their robustness to complex nonlinear modal dynamics also requires additional research. It is expected that the extension of the gray-box strategy to structures with complex modal dynamics is very difficult. The other two approaches are not limited in this respect, however, the treatment of more complex models poses additional challenges from a numerical point of view. Moreover, it is noted that the identification concepts that have been proposed in this thesis are by no means exhaustive and further concepts should be studied.

The application examples have shown that NEMA is not restricted to structures with smooth and conservative nonlinearities. The measurement of nonlinear modes of nonsmooth systems is a particularly interesting concept for the design of nonsmooth vibration absorbers. Since nonlinear vibration absorbers are designed based on numerical and theoretical nonlinear modal analysis, NEMA seems to be the ideal complement from an experimental point of view. It is noted, however, that in this context the capability of NEMA to treat structures with a strong change in nonlinear mode shape and internal resonances is a crucial requirement. The accurate characterization of nonlinear damping mechanisms is still regarded as a major challenge in nonlinear system identification. It has been shown in this thesis, that nonlinear phase resonance testing is a promising concept in this respect. Yet, future research is required to confirm this statement, particularly for structures with higher complexity.

Appendix A

Fourier series

In this thesis, different notations for the Fourier series are used for different purposes. The relation between these different notations is for completeness shown in the following. For the sake of simplicity this derivation is made for a scalar quantity $x(t)$, keeping in mind that for a higher dimensional vector $\boldsymbol{x}(t)$ the same procedure can be applied for each entry of $\boldsymbol{x}(t)$ separately. For the numerical simulations a trigonometric notation is used

$$x(t) = x_0 + \sum_{n=1}^{\infty} x_{\mathrm{c},n} \cos(n\omega t) + x_{\mathrm{s},n} \sin(n\omega t). \tag{A.1}$$

In the context of experimental nonlinear mode extraction a complex Fourier series is used

$$x(t) = \sum_{n=-\infty}^{\infty} \underline{x}_n \mathrm{e}^{in\omega t}, \tag{A.2}$$

allowing for a more compact derivation of the different power components. Both notations are fully equivalent and can be transferred in one another using Euler's formula. The n-th harmonic component of Eq. A.1 can be written as

$$
\begin{aligned}
x_n(t) &= x_{\mathrm{c},n} \cos(n\omega t) + x_{\mathrm{s},n} \sin(n\omega t) \\
&= \frac{1}{2} x_{\mathrm{c},n} (\mathrm{e}^{in\omega t} + \mathrm{e}^{-in\omega t}) + \frac{1}{2i} x_{\mathrm{s},n} (\mathrm{e}^{in\omega t} - \mathrm{e}^{-in\omega t}),
\end{aligned} \tag{A.3}
$$

which can be rearranged to

$$x_n(t) = \frac{1}{2} (x_{\mathrm{c},n} - i x_{\mathrm{s},n}) \mathrm{e}^{in\omega t} + \frac{1}{2} (x_{\mathrm{c},n} + i x_{\mathrm{s},n}) \mathrm{e}^{-in\omega t}. \tag{A.4}$$

By the introduction of the complex Fourier coefficient for the n-th harmonic

$$\underline{x}_n = \frac{1}{2}(x_{c,n} - ix_{s,n}) \tag{A.5}$$

and its conjugate complex

$$\underline{x}_{-n} = \bar{\underline{x}}_n = \frac{1}{2}(x_{c,n} + ix_{s,n}) \tag{A.6}$$

one can write Eq. (A.1) in the compact form of Eq. (A.2).
Another way of writing Eq. (A.1) is in terms of an amplitude $\hat{x}_n$ and phase φ_n for every harmonic n as

$$x(t) = x_0 + \sum_{n=1}^{\infty} \hat{x}_n \cos(n\omega t + \varphi_n) \tag{A.7}$$

with

$$\hat{x}_n = \sqrt{(x_{c,n})^2 + (x_{s,n})^2} \tag{A.8}$$

and

$$\varphi_n = \arctan\left(\frac{x_{s,n}}{x_{c,n}}\right). \tag{A.9}$$

For the complex coefficients introduced in Eq. (A.5) and (A.6) this notation yields

$$\underline{x}_n = \frac{1}{2}\hat{x}_n e^{-in\varphi_n} \tag{A.10}$$

and

$$\underline{x}_{-n} = \frac{1}{2}\hat{x}_n e^{in\varphi_n}. \tag{A.11}$$

With this notation the complex Fourier series in Eq. (A.2) can be expressed in terms of the amplitudes $\hat{x}_n$ and phases φ_n as

$$x(t) = x_0 + \sum_{n=1}^{\infty} \text{Re}\left\{\hat{x}_n e^{i(n\omega t - \varphi_n)}\right\}, \tag{A.12}$$

or equivalently as

$$x(t) = x_0 + \sum_{n=1}^{\infty} 2 \operatorname{Re} \left\{ \underline{x}_n \mathrm{e}^{\mathrm{i}n\omega t} \right\}. \tag{A.13}$$

Appendix B

Analytical Gradients

This appendix includes the derivatives of the residual in Eq. (3.36), which are required for the Newton-like solution method. The derivative of the nonlinear force is treated separately, in Chapter 3.2.4, such that only the derivatives of the linear parts are explicitly evaluated here.

The derivative of the residual $\boldsymbol{r}$ with respect to the Fourier coefficient of the displacements reads

$$\frac{\partial \boldsymbol{r}(\boldsymbol{x}_{\mathrm{nl}}, \omega)}{\partial \boldsymbol{x}_{\mathrm{nl}}} = \mathbf{H}_{\mathrm{red}}(\omega) + \frac{\partial \boldsymbol{g}_{\mathrm{nl}}(\boldsymbol{x}_{\mathrm{nl}}, \omega)}{\partial \boldsymbol{x}_{\mathrm{nl}}}. \tag{B.1}$$

The derivative with respect to the frequency ω can be calculated as

$$\frac{\partial \boldsymbol{r}(\boldsymbol{x}_{\mathrm{nl}}, \omega)}{\partial \omega} = \frac{\partial \mathbf{H}_{\mathrm{red}}(\omega)}{\partial \omega} \boldsymbol{x}_{\mathrm{nl}} + \frac{\partial \boldsymbol{g}_{\mathrm{nl}}(\boldsymbol{x}_{\mathrm{nl}}, \omega)}{\partial \omega}, \tag{B.2}$$

which is more complicated to evaluate as it involves the derivative of the reduced dynamic stiffness matrix

$$\frac{\partial \mathbf{H}_{\mathrm{red}}}{\partial \omega} = \frac{\partial \mathbf{H}_{\mathrm{nlnl}}}{\partial \omega} - \left[\frac{\partial \mathbf{H}_{\mathrm{nlln}}}{\partial \omega} \mathbf{H}_{\mathrm{lnln}}^{-1} \mathbf{H}_{\mathrm{lnnl}} \right.$$
$$\left. + \mathbf{H}_{\mathrm{nlln}} \frac{\partial \mathbf{H}_{\mathrm{lnln}}^{-1}}{\partial \omega} \mathbf{H}_{\mathrm{lnnl}} + \mathbf{H}_{\mathrm{nlln}} \mathbf{H}_{\mathrm{lnln}}^{-1} \frac{\partial \mathbf{H}_{\mathrm{lnnl}}}{\partial \omega} \right], \tag{B.3}$$

where the dependence on ω is omitted for the sake of brevity. The evaluation of the derivative of the respective partitions of the dynamic stiffness matrix $\mathbf{H}_*$ is straightforward

$$\frac{\partial \mathbf{H}_*}{\partial \omega} = \frac{2}{\omega} \nabla^2 \otimes \mathbf{M}_*, \tag{B.4}$$

whereas the derivative of the inverse matrix $\mathbf{H}_{\mathrm{lnln}}^{-1}$ must be calculated as[1]

$$\frac{\partial \mathbf{H}_{\mathrm{lnln}}^{-1}}{\partial \omega} = -\mathbf{H}_{\mathrm{lnln}}^{-1}\frac{\partial \mathbf{H}_{\mathrm{lnln}}}{\partial \omega}\mathbf{H}_{\mathrm{lnln}}^{-1}. \tag{B.5}$$

The calculation of the derivative of the energy equation with respect to the Fourier coefficients of the displacements yields

$$\frac{\partial E_{\mathrm{kin}}}{\partial \boldsymbol{x}_{\mathrm{nl}}} = -\frac{1}{2}\boldsymbol{x}_{\mathrm{nl}}^{\mathrm{T}}\check{\mathbf{M}}_{\mathrm{red}}. \tag{B.6}$$

The derivative with respect to the frequency can be calculated based on Eq. (3.35) as

$$\begin{aligned}
\frac{\partial E_{\mathrm{kin}}}{\partial \omega} = -\frac{1}{4}\boldsymbol{x}_{\mathrm{nl}}^{\mathrm{T}}&\left(\frac{2}{\omega}\check{\mathbf{M}}_{\mathrm{nlnl}} + \frac{\partial \mathbf{A}^{\mathrm{T}}}{\partial \omega}\check{\mathbf{M}}_{\mathrm{lnnl}}\right.\\
&\left.+\check{\mathbf{M}}_{\mathrm{nlln}}\frac{\partial \mathbf{A}}{\partial \omega} + \frac{\partial \mathbf{A}^{\mathrm{T}}}{\partial \omega}\check{\mathbf{M}}_{\mathrm{lnln}}\mathbf{A} + \mathbf{A}^{\mathrm{T}}\check{\mathbf{M}}_{\mathrm{lnln}}\frac{\partial \mathbf{A}}{\partial \omega}\right)\boldsymbol{x}_{\mathrm{nl}},
\end{aligned} \tag{B.7}$$

where the derivative of the matrix $\mathbf{A} = \mathbf{H}_{\mathrm{lnln}}^{-1}\mathbf{H}_{\mathrm{lnnl}}$ can be calculated using the derivative of the dynamic stiffness matrix in Eq. (B.5). It should be noted that the only inverse matrix which is used for the calculation of all these parts of the Jacobian matrix is the inverse $\mathbf{H}_{\mathrm{lnln}}^{-1}$, which is already available from the condensation procedure described in Section 3.2.2.

---

[1]In cases where a mixed modal/physical formulation is used (see Section 3.2.5) the evaluation of the derivative is straightforward.

Appendix C

Generalized Condensation in Mixed-Modal-Physical Coordinates

For systems with Caughey-type damping, the damping matrix can be diagonalized with the eigenvectors of the undamped eigenvalue problem. Therefore, the transformation with the CB matrix also yields a diagonal matrix for the linear partition of the damping matrix, i.e.,

$$\mathbf{D}_{\text{CB,lnln}} = \text{diag}\left\{d_1, \dots d_{N_{\text{ln}}}\right\}. \tag{C.1}$$

The linear partition of the dynamic stiffness matrix in Eq. (3.31) can be written for each harmonic n in CB coordinates as

$$\mathbf{H}_{n,\text{lnln}}(\omega) = \begin{bmatrix} (-\omega^2\mathbf{I}_{N_{\text{ln}}} + \mathbf{K}_{\text{CB,lnln}}) & \omega\mathbf{D}_{\text{CB,lnln}} \\ -\omega\mathbf{D}_{\text{CB,lnln}} & (-\omega^2\mathbf{I}_{N_{\text{ln}}} + \mathbf{K}_{\text{CB,lnln}}) \end{bmatrix}, \tag{C.2}$$

where all matrices are diagonal. The dynamic stiffness matrix can be written more compact in complex form as

$$\underline{\mathbf{H}}_{n,\text{lnln}}(\omega) = -n^2\omega^2\mathbf{I}_{N_{\text{ln}}} + in\omega\mathbf{D}_{\text{CB,lnln}} + \mathbf{K}_{\text{CB,lnln}}, \tag{C.3}$$

the inversion of which is trivial

$$\underline{\mathbf{H}}_{n,\text{lnln}}^{-1}(\omega) = \text{diag}\left\{ \frac{1}{-n^2\omega^2 + ind_1 + \omega_{0,\text{ln},1}^2}, \cdots, \right.$$
$$\left. \frac{1}{-n^2\omega^2 + ind_{N_{\text{ln}}} + \omega_{0,\text{ln},N_{\text{ln}}}^2} \right\}. \tag{C.4}$$

The inverse of the dynamic stiffness matrix can then be transformed back into the trigonometric form, yielding a block matrix for each harmonic n

as

$$\mathbf{H}^{-1}_{n,\mathrm{lnln}}(\omega) = \begin{bmatrix} \mathrm{Re}\left\{\underline{\mathbf{H}}^{-1}_{n,\mathrm{lnln}}(\omega)\right\} & \mathrm{Im}\left\{\underline{\mathbf{H}}^{-1}_{n,\mathrm{lnln}}(\omega)\right\} \\ -\mathrm{Im}\left\{\underline{\mathbf{H}}^{-1}_{n,\mathrm{lnln}}(\omega)\right\} & \mathrm{Re}\left\{\underline{\mathbf{H}}^{-1}_{n,\mathrm{lnln}}(\omega)\right\} \end{bmatrix}. \tag{C.5}$$

Herein, the real and imaginary part of the inverse dynamic stiffness matrix can be explicitly evaluated as

$$\mathrm{Re}\left\{\underline{\mathbf{H}}^{-1}_{n,\mathrm{lnln}}(\omega)\right\} = \mathrm{diag}\left\{ \frac{-n^2\omega^2 + \omega^2_{0,\mathrm{ln},1}}{(-n^2\omega^2 + \omega^2_{0,\mathrm{ln},1})^2 + d_1^2 n^2\omega^2}, \cdots, \right.$$
$$\left. \frac{-n^2\omega^2 + \omega^2_{0,\mathrm{ln},N_{\mathrm{ln}}}}{(-n^2\omega^2 + \omega^2_{0,\mathrm{ln},N_{\mathrm{ln}}})^2 + d_{N_{\mathrm{ln}}}^2 n^2\omega^2} \right\} \tag{C.6}$$

and

$$\mathrm{Im}\left\{\underline{\mathbf{H}}^{-1}_{n,\mathrm{lnln}}(\omega)\right\} = \mathrm{diag}\left\{ \frac{d_1 n\omega}{(-n^2\omega^2 + \omega^2_{0,\mathrm{ln},1})^2 + d_1^2 n^2\omega^2}, \cdots, \right.$$
$$\left. \frac{d_{N_{\mathrm{ln}}} n\omega}{(-n^2\omega^2 + \omega^2_{0,\mathrm{ln},N_{\mathrm{ln}}})^2 + d_{N_{\mathrm{ln}}}^2 n^2\omega^2} \right\}. \tag{C.7}$$

Therefore, the inverse of the linear partition of the dynamic stiffness matrix is available in closed form, if the system is written in CB coordinates and the damping matrix can be diagonalized.

Appendix D

Truck Model

Nonlinear Element	Direction	Used Monomial		
		lin.	cub.	quin.
1 Air Spring Front	x	✓		
	y	✓		
	z	✓		✓
	φ_{xx}	✓		
	φ_{yy}	✓		
	φ_{zz}	✓		
2 Rotational Bearing	x	✓	✓	
	y	✓	✓	✓
	z	✓	✓	
	φ_{xx}	✓	✓	✓
	φ_{yy}	✓		
	φ_{zz}	✓	✓	✓
3 Guide Bearing	x	✓		✓
	y	✓	✓	✓
	z	✓		✓
	φ_{xx}	✓	✓	✓
	φ_{yy}	✓		✓
	φ_{zz}	✓		✓

Table D.1: Used monomials for the nonlinear elements in the driver's cabin model in Chapter 3.3 (part 1 of 2)

This appendix includes an overview of the used nonlinear elements in the numerical demonstration in Chapter 3.3. The coefficients of the nonlinear elements have been identified by fitting of measured force-displacement

curves. For the fitting polynomials up to order five have been used. The
tables Tab. D.1 and Tab. D.2 provide a summary which monomial has
been used to approximate the force laws in each direction of the nonlinear
elements. For confidentiality reasons, neither the coefficients nor the force-
displacement curves are shown in this thesis.

Nonlinear Element	Direction	Used Monomial		
		lin.	cub.	quin.
4 Steel Spring Front	x	✓		
	y	✓		
	z	✓		✓
	φ_{xx}	✓		
	φ_{yy}	✓		
	φ_{zz}	✓		
5 Bolt Bearing	x	✓		✓
	y	✓	✓	✓
	z	✓	✓	✓
	φ_{xx}	✓		
	φ_{yy}	✓		
	φ_{zz}	✓		
6 Wishbone Bearing	x	✓		
	y	✓	✓	✓
	z	✓	✓	✓
	φ_{xx}	✓		
	φ_{yy}	✓		
	φ_{zz}	✓		

Table D.2: Used monomials for the nonlinear elements in the driver's cabin model
in Chapter 3.3 (part 2 of 2).

Appendix E

Proof of Power Inequality

The power triangular relation, well-known from linear theory, becomes an inequality in the nonlinear case, i.e.,

$$S_j^2 \geq P_j^2 + Q_j^2, \tag{E.1}$$

which has been stated in Chapter 4, Eq. (4.26). For completeness, the proof of this inequality relation is included in this appendix.

Using the definitions of apparent (c.f. Eq. (4.25)), active (c.f. Eq. (4.23)) and reactive power (c.f. Eq. (4.24)) the inequality in Eq. (E.1) reads

$$\sum_{n=1}^{\infty} F_n^2 \sum_{n=1}^{\infty} V_n^2 \geq \left(\sum_{n=1}^{\infty} F_n V_n \cos(\varphi_n) \right)^2 + \left(\sum_{n=1}^{\infty} F_n V_n \sin(\varphi_n) \right)^2, \tag{E.2}$$

where the index j is omitted for the sake of brevity. This inequality can be proven by mathematical induction. Let k denote the upperbound of the summation.

Base case $k = 1$

$$F_1^2 V_1^2 \geq (F_1 V_1 \cos(\varphi_1))^2 + (F_1 V_1 \sin(\varphi_1))^2 = F_1^2 V_1^2. \tag{E.3}$$

Inductive step Suppose that

$$\sum_{n=1}^{k} F_n^2 \sum_{n=1}^{k} V_n^2 \geq \left(\sum_{n=1}^{k} F_n V_n \cos(\varphi_n) \right)^2 + \left(\sum_{n=1}^{k} F_n V_n \sin(\varphi_n) \right)^2 \tag{E.4}$$

149

holds. It has to be shown that

$$\sum_{n=1}^{k+1} F_n^2 \sum_{n=1}^{k+1} V_n^2 \geq \left(\sum_{n=1}^{k+1} F_n V_n \cos\left(\varphi_n\right) \right)^2 + \left(\sum_{n=1}^{k+1} F_n V_n \sin\left(\varphi_n\right) \right)^2 \quad \text{(E.5)}$$

follows from Eq. (E.4). Therefore, Eq. (E.5) is written as

$$\sum_{n=1}^{k+1} F_n^2 \sum_{n=1}^{k+1} V_n^2 - \left(\sum_{n=1}^{k+1} F_n V_n \cos\left(\varphi_n\right) \right)^2 - \left(\sum_{n=1}^{k+1} F_n V_n \sin\left(\varphi_n\right) \right)^2 \geq 0. \quad \text{(E.6)}$$

Equation (E.6) can be rearranged as

$$\left(\sum_{n=1}^{k} F_n^2 + F_{k+1}^2 \right) \left(\sum_{n=1}^{k} V_n^2 + V_{k+1}^2 \right) -$$
$$\left(\sum_{n=1}^{k} F_n V_n \cos\left(\varphi_n\right) + F_{k+1} V_{k+1} \cos\left(\varphi_{k+1}\right) \right)^2 - \quad \text{(E.7)}$$
$$\left(\sum_{n=1}^{k} F_n V_n \sin\left(\varphi_n\right) + F_{k+1} V_{k+1} \sin\left(\varphi_{k+1}\right) \right)^2 \geq 0$$

or

$$\sum_{n=1}^{k} F_n^2 \sum_{n=1}^{k} V_n^2 + F_{k+1}^2 \sum_{n=1}^{k} V_n^2 + V_{k+1}^2 \sum_{n=1}^{k} F_n^2 + F_{k+1}^2 V_{k+1}^2$$
$$- \left(\sum_{n=1}^{k} F_n V_n \cos\left(\varphi_n\right) \right)^2 - 2 F_{k+1} V_{k+1} \cos\left(\varphi_{k+1}\right) \sum_{n=1}^{k} F_n V_n \cos\left(\varphi_n\right)$$
$$- F_{k+1}^2 V_{k+1}^2 \cos^2\left(\varphi_{k+1}\right) \quad \text{(E.8)}$$
$$- \left(\sum_{n=1}^{k} F_n V_n \sin\left(\varphi_n\right) \right)^2 - 2 F_{k+1} V_{k+1} \sin\left(\varphi_{k+1}\right) \sum_{n=1}^{k} F_n V_n \sin\left(\varphi_n\right)$$
$$- F_{k+1}^2 V_{k+1}^2 \sin^2\left(\varphi_{k+1}\right) \geq 0.$$

Equation (E.8) can be simplified with the trigonometric identity $\sin^2(\varphi_{k+1}) + \cos^2(\varphi_{k+1}) = 1$. Furthermore, Eq. (E.4) provides an estimate of the brack-

eted terms yielding

$$\sum_{n=1}^{k} F_n^2 \sum_{n=1}^{k} V_n^2 + F_{k+1}^2 \sum_{n=1}^{k} V_n^2 + V_{k+1}^2 \sum_{n=1}^{k} F_n^2 + F_{k+1}^2 V_{k+1}^2$$

$$- \sum_{n=1}^{k} F_n^2 \sum_{n=1}^{k} V_n^2 - 2F_{k+1} V_{k+1} \cos(\varphi_{k+1}) \sum_{n=1}^{k} F_n V_n \cos(\varphi_n) \qquad \text{(E.9)}$$

$$- 2F_{k+1} V_{k+1} \sin(\varphi_{k+1}) \sum_{n=1}^{k} F_n V_n \sin(\varphi_n) - F_{k+1}^2 V_{k+1}^2 \geq 0,$$

or simply

$$\overbrace{F_{k+1}^2 \sum_{n=1}^{k} V_n^2 + V_{k+1}^2 \sum_{n=1}^{k} F_n^2}^{:=a} \underbrace{-2F_{k+1} V_{k+1}}$$

$$\underbrace{\left(\cos(\varphi_{k+1}) \sum_{n=1}^{k} F_n V_n \cos(\varphi_n) + \sin(\varphi_{k+1}) \sum_{n=1}^{k} F_n V_n \sin(\varphi_n) \right)}_{:=b} \geq 0,$$

$$\text{(E.10)}$$

i.e., $a - 2F_{k+1}V_{k+1}b \geq 0$. The upper bound of term b can be estimated by trigonometric transformations as

$$\sqrt{\left(\sum_{n=1}^{k} F_n V_n \cos(\varphi_n) \right)^2 + \left(\sum_{n=1}^{k} F_n V_n \sin(\varphi_n) \right)^2} \geq$$

$$\cos(\varphi_{k+1}) \sum_{n=1}^{k} F_n V_n \cos(\varphi_n) + \sin(\varphi_{k+1}) \sum_{n=1}^{k} F_n V_n \sin(\varphi_n), \qquad \text{(E.11)}$$

which can be inserted in Eq. (E.10) and multiplied by $a + 2F_{k+1}V_{k+1}b \geq 0$, yielding

$$F_{k+1}^4 \left(\sum_{n=1}^k V_n^2 \right)^2 + V_{k+1}^4 \left(\sum_{n=1}^k F_n^2 \right)^2 + 2F_{k+1}^2 V_{k+1}^2 \sum_{n=1}^k F_n^2 \sum_{n=1}^k V_n^2$$
$$- 4F_{k+1}^2 V_{k+1}^2 \left[\left(\sum_{n=1}^k F_n V_n \cos(\varphi_n) \right)^2 + \left(\sum_{n=1}^k F_n V_n \sin(\varphi_n) \right)^2 \right] \geq 0.$$

$$\tag{E.12}$$

The term in square brackets can, once again, be simplified using the estimation in Eq. (E.4) yielding

$$F_{k+1}^4 \left(\sum_{n=1}^k V_n^2 \right)^2 + V_{k+1}^4 \left(\sum_{n=1}^k F_n^2 \right)^2 + 2F_{k+1}^2 V_{k+1}^2 \sum_{n=1}^k F_n^2 \sum_{n=1}^k V_n^2$$
$$- 4F_{k+1}^2 V_{k+1}^2 \sum_{n=1}^k F_n^2 \sum_{n=1}^k V_n^2 \geq 0,$$

$$\tag{E.13}$$

which can be rearranged as

$$F_{k+1}^4 \left(\sum_{n=1}^k V_n^2 \right)^2 + V_{k+1}^4 \left(\sum_{n=1}^k F_n^2 \right)^2 - 2F_{k+1}^2 V_{k+1}^2 \sum_{n=1}^k F_n^2 \sum_{n=1}^k V_n^2 \geq 0.$$

$$\tag{E.14}$$

Using the binomial theorem, Eq. (E.14) can be written in a compact form as

$$\left(F_{k+1}^2 \sum_{n=1}^k V_n^2 - V_{k+1}^2 \sum_{n=1}^k F_n^2 \right)^2 \geq 0, \tag{E.15}$$

which is always positive. $\qquad\square$

Appendix F

Numerical Model of an Electrodynamic Shaker

In Chapter 4, the dynamics of the excitation mechanism is included in the numerical experiments to obtain a realistic representation of the actual experiment. The shaker model and its parameterization is described in this appendix.

Various shaker models of different level of detail have been introduced in the literature depending on the phenomena under investigation (McConnel and Varoto, 2008). Following Della Flora and Gründling (2008) the shaker is modeled here with two mechanical DOFs and one electrical DOF. The shaker model assumes that the power amplifier is driven in voltage mode of operation, such that the amplifier can be modeled as a constant gain[1]. The model of the shaker, which is shown in Fig. F.1, consists of the electrical circuit and the model of the mechanical properties. The electrical circuit includes a voltage source $u_0(t)$, the inductance L and the resistance R of the shaker's armature. Moreover, a second voltage source is included, which represents the electromagnetic feedback voltage $u_{\text{em}}(t)$, which is proportional to the coil velocity, i.e.,

$$u_{\text{em}}(t) = \Pi \dot{x}_{\text{C}}(t), \tag{F.1}$$

where Π is an electromagnetic coupling constant which depends on the flux density and the length of the armature conductors. Using Eq. (F.1) the differential equation describing the electrical circuit can be derived using

---

[1]This assumption is based on the consideration that only the fundamental harmonic of the force is controlled, whereas higher harmonics are expected to play a role in practice due to the nonlinearity of the test specimen. In voltage mode the comparatively strong damping of the electric circuit is expected to reduce the uncontrolled higher harmonics.
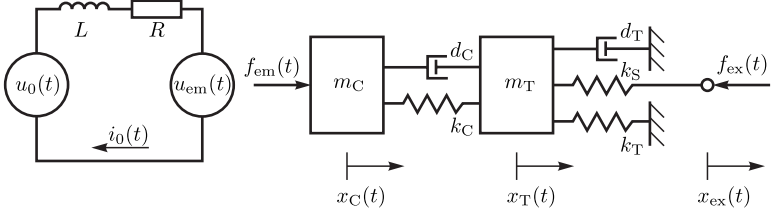
Figure F.1: Numerical model of a shaker.

Kirchhoff's laws yielding

$$u_0(t) = L\frac{\mathrm{d}i_0(t)}{\mathrm{d}t} + Ri_0(t) + \Pi\dot{x}_\mathrm{C}(t). \tag{F.2}$$

The mechanical model consists of one mass representing the shaker coil and one mass representing the shaker table. The masses are connected by a spring damper combination modeling the coil's stiffness and damping properties. The shaker table is connected to the environment by the suspension, which is also modeled by a spring-damper combination. Moreover, the shaker table is connected to the structure with a stinger. The stinger is represented by the stinger stiffness k_S[2]. In experiments, typically the excitation force is measured, i.e., the force

$$f_\mathrm{ex}(t) = k_\mathrm{S}\left(x_\mathrm{T}(t) - x_\mathrm{ex}(t)\right) \tag{F.3}$$

is known. The electromagnetic force, which acts on the shaker coil is proportional to the current in the shaker and can be calculated as

$$f_\mathrm{em}(t) = \Pi i_0(t). \tag{F.4}$$

Hence, the equation of motion of the mechanical properties of the shaker can be derived as[3]

$$\begin{aligned}
m_\mathrm{C}\ddot{x}_\mathrm{C} + d_\mathrm{C}(\dot{x}_\mathrm{C} - \dot{x}_\mathrm{T}) + k_\mathrm{C}(x_\mathrm{C} - x_\mathrm{T}) &= \Pi i_0, \\
m_\mathrm{T}\ddot{x}_\mathrm{T} + d_\mathrm{C}(\dot{x}_\mathrm{T} - \dot{x}_\mathrm{C}) + k_\mathrm{C}(x_\mathrm{T} - x_\mathrm{C}) + d_\mathrm{T}\dot{x}_\mathrm{T} + k_\mathrm{T}x_\mathrm{T} &= -f_\mathrm{ex}.
\end{aligned} \tag{F.5}$$

---

[2]The stinger stiffness in the numerical simulations is estimated based on the static stiffness of a rod with realistic geometry and material properties (see Tab. F.1).

[3]Time dependence is omitted here for the sake of brevity.

Parameter	Value	Unit
m_C	19	g
m_T	24.3	g
k_C	84222	N/mm
k_T	20.7	N/mm
k_S	$1.32 \cdot 10^8$	N/mm
d_C	57.2	N/m^3
d_T	28.3	s
Π	15.5	N/A
R	0.8	Ω
L	140	μH

Table F.1: Parameters of the numerical shaker model.

Thus, the total shaker dynamics is modeled by Eq. (F.2) and Eq. (F.5). This shaker model involves several electrical and mechanical parameters. The parameters are adjusted in this thesis such that they resemble the behavior of a BRÜEL & KJÆR TYPE 4808 shaker, which has been used in the laboratory experiments. The mechanical parameters and the electromechanical coupling constant Π have been identified based on experimental data obtained for the real shaker. The shaker has two mechanical modes: The suspension mode, where coil and table move in phase and the coil mode, where coil and table move anti-phase. To identify the physical parameters Chen and Liaw (1999) proposes to compare the transfer function, which covers the frequency range of both modes, of the unloaded shaker to the transfer function of a shaker loaded with a rigid mass. Using this method the mechanical parameters and the electromechanical coupling constant have been identified to be the values in Tab. F.1[4]. The electrical parameters R and L have a minor influence on the shaker dynamics and have been chosen based on the shaker specifications (see Tab. F.1)

---

[4]For details the reader is referred to the thesis of Morlock (2015).

Appendix G

PLL Parameters

It is shown in Chapter 4 that the PLL controller, which is used for the NEMA has several tuning parameters. The tuning has been done in a heuristic way. This appendix includes tables with the tuning parameters of the PLL controllers used in the numerical study in Chapter 4 and the experimental applications in Chapter 6.

Parameter	Value	Unit
ω_c	$29 \cdot 2\pi$	rad/s
ω_L	π	rad/s
T_I	$2/\pi$	s
K_P	5	-

Table G.1: Parameters of the PLL used for the numerical study in Chapter 4.3 and the experimental application in Chapter 6.1.

Parameter	Value	Unit
ω_c	$43 \cdot 2\pi$	rad/s
ω_L	π	rad/s
T_I	$2/\pi$	s
K_P	5	-

Table G.2: Parameters of the PLL used for the experimental study in Chapter 6.2.

Parameter	Value	Unit
ω_c	$370 \cdot 2\pi$	rad/s
ω_L	π	rad/s
T_I	$2/\pi$	s
K_P	10	-

Table G.3: Parameters of the PLL used for the experimental study in Chapter 6.3.

Appendix H

Experimental Equipment

The setup and instrumentation for the different experimental applications in Chapter 6 is similar. The schematic sketch of the setup used for NEMA and FRF tests is shown in Fig. H.1. Time dependence of the measured signals is omitted for the sake of clarity. The used hardware for all experiments is essentially the same and listed in Tab. H.1. Peculiarities of specific experiments are indicated by footnotes. In the beam experiments, the signals have been recorded at a sampling rate of 20 kHz and for the joint resonator at 10 kHz. The EMA has been carried out with a SIEMENS LMS SCADAS MOBILE system with white noise shaker excitation with a bandwidth of 10 to 2000 Hz.
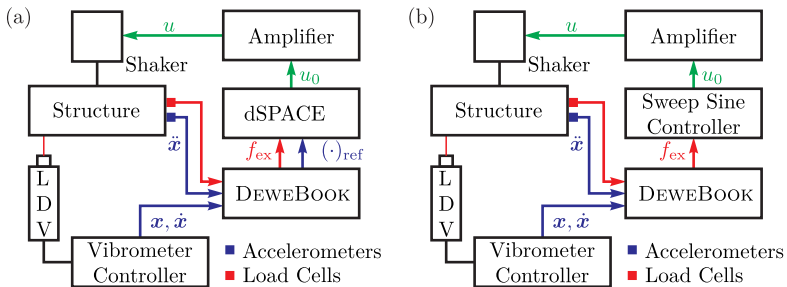

Figure H.1: Schematic sketch of the experimental hardware used for NEMA and PLL based measurements (a) and for sweep sine FRF measurements (b).

---

[1] Applicable for both beam experiments.

[2] Applicable the beam with impact.

[3] Applicable for the joint resonator.

Device	Hardware	Details
Shaker	Brüel&Kjær	Type 4808
Amplifier	Brüel&Kjær	Type 2712
		low impedance mode
Controller	dSPACE	DS1103
Data	DeweBook	2 units: DEWE-50-USB2-8
acquisition		5 voltage input channels,
		8 IEPE input channels
Vibrometer[1]	Polytec	2 units:
controller		1 OFV-3001,
		1 OFV-5000
LDV[1]	Polytec	2 units:
		1 OFV-505,
		1 OFV-353
Accelerometers[1]	PCB Piezotronics	7(6^2) units: 352C22 (IEPE)
Accelerometers[3]	PCB Piezotronics	3 units: 356A24 (IEPE)
Load cell	Brüel&Kjær	Type 8230
excitation		
Load cell[2]	Endevco	2311-100
contact		
Sweep sine	Brüel&Kjær	Type 1050
controller		

Table H.1: Used hardware in the experimental applications in Chapter 6.

Appendix I

PLL Controller for FRF Measurement

For the measurement of the FRF, which is used for verification of the gray-box model prediction in Chapter 6.1, the PLL controller (c.f. Fig. 4.6) is extended by a phase shifter element and an amplitude controller. A block diagram of the augmented PLL is shown in Fig. I.1. The phase shifter element adds a constant value to the output of the phase detector to modify the phase of the excitation force with respect to the reference signal to values different from $\pi/2$. The amplitude controller is based on the RMS value of the excitation force, which can be easily estimated in real time. The desired force amplitude is divided by $\sqrt{2}$ to obtain the RMS value and then subtracted from the measured RMS value of the force. The difference is then minimized by a PI controller, the output of which is used as voltage amplitude for the input voltage to the shaker.
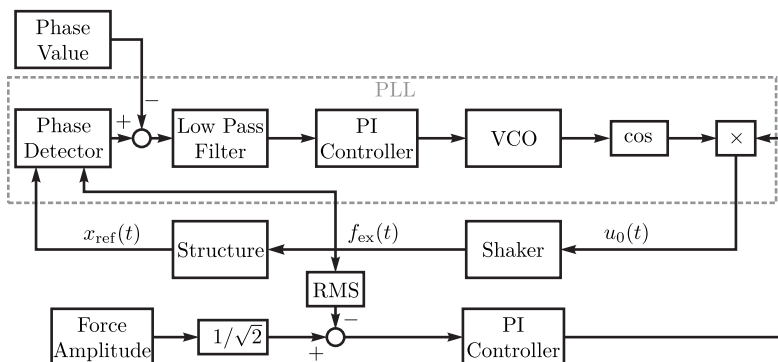

Figure I.1: Augmented PLL for force controlled FRF measurement.

Bibliography

D. Abramovitch. Lyapunov redesign of analog phase-lock loops. *IEEE Transactions on Communications*, 38(12):2197–2202, 1990.

D. Abramovitch. Phase-locked loops: a control centric tutorial. In *Proceedings of the 2002 American Control Conference (IEEE Cat. No.CH37301)*, volume 1, pages 1–15, Anchorage, 2002.

D. Adams and R. Allemang. A frequency domain method for estimating the parameters of a non-linear structural dynamic model through feedback. *Mechanical Systems and Signal Processing*, 14(4):637–656, 2000.

M. A. Al-Hadid and J. R. Wright. Developments in the force-state mapping technique for non-linear systems and the extension to the location of non-linear elements in a lumped-parameter system. *Mechanical Systems and Signal Processing*, 3(3):269–290, 1989.

M. A. Al-Hadid and J. R. Wright. Application of the force-state mapping approach to the identification of non-linear systems. *Mechanical Systems and Signal Processing*, 4(6):463–482, 1990.

R. J. Allemang. The Modal Assurance Criterion - Twenty years of use and abuse. In *Proceedings of IMAC XX*, pages 397–405, Los Angeles, 2002.

E. L. Allgower and K. Georg. Numerical path following. Technical report, Colorado State University, 1994.

R. Arquier, S. Bellizzi, R. Bouc, and B. Cochelin. Two methods for the computation of nonlinear modes of vibrating systems at large amplitudes. *Computers & Structures*, 84(24):1565–1576, 2006.

P. A. Atkins, J. R. Wright, and K. Worden. An extension of force appropriation to the identification of non-linear multi-degree of freedom systems. *Journal of Sound and Vibration*, 237(1):23–43, 2000.

K. V. Avramov and Y. V. Mikhlin. Review of applications of nonlinear normal modes for vibrating mechanical systems. *Applied Mechanics Reviews*, 65(2):020801–1–020801–20, 2013.

V. I. Babitsky and I. J. Sokolov. Autoresonant homeostat concept for engineering application of nonlinear vibration modes. *Nonlinear Dynamics*, 50(3):447–460, 2007.

R. E. Best. *Phase-Locked Loops: Design, simulation, and applications*. McGraw-Hill, New York, 6. edition, 2007.

F. Blanc, C. Touzé, J. F. Mercier, K. Ege, and A. S. Bonnet Ben-Dhia. On the numerical computation of nonlinear normal modes for reduced-order modelling of conservative vibratory systems. *Mechanical Systems and Signal Processing*, 36(2):520–539, 2013.

S. Bograd, P. Reuss, A. Schmidt, L. Gaul, and M. Mayer. Modeling the dynamics of mechanical joints. *Mechanical Systems and Signal Processing*, 25(8):2801–2826, 2011.

S. Bohlen. *Zur Berechnung und Messung mechanischer Schwingungen in Strukturen mit nichtlinearem Fügestellenverhalten*. VDI-Verlag, Düsseldorf, 11. edition, 1987.

J. P. Boyd. Computing the zeros, maxima and inflection points of Chebyshev, Legendre and Fourier series: Solving transcendental equations by spectral interpolation and polynomial rootfinding. *Journal of Engineering Mathematics*, 56(3):203–219, 2006.

C. Budeanu. *Puissances réactives et fictives*. Impr. Cultura Nationala, Bucharest, 1927.

T. M. Cameron and J. H. Griffin. An alternating frequency/time domain method for calculating the steady-state response of nonlinear dynamic systems. *Journal of Applied Mechanics*, 56(1):149, 1989.

A. Cardona, T. Coune, A. Lerusse, and M. Geradin. A multiharmonic method for non-linear vibration analysis. *International Journal for Numerical Methods in Engineering*, 37(9):1593–1608, 1994.

A. Carrella and D. J. Ewins. Identifying and quantifying structural non-linearities in engineering applications from measured frequency response functions. *Mechanical Systems and Signal Processing*, 25(3):1011–1027, 2011.

T. K. Caughey. Classical normal modes in damped linear dynamic systems. *Journal of Applied Mechanics*, 27(2):269, 1960.

T. H. Chen and C. M. Liaw. Vibration acceleration control of an inverter-fed electrodynamic shaker. *IEEE/ASME Transactions on Mechatronics*, 4(1):60–70, 1999.

Y. Chong and M. Imregun. Development and application of a nonlinear modal analysis technique for MDOF systems. *Journal of Vibration and Control*, 7(2):167–179, 2001.

B. Cochelin and C. Vergez. A high order purely frequency-based harmonic balance formulation for continuation of periodic solutions. *Journal of Sound and Vibration*, 324(1-2):243–262, 2009.

S. B. Cooper, D. Di Maio, and D. J. Ewins. Nonlinear vibration analysis of a complex aerospace structure. In G. Kerschen, editor, *Nonlinear Dynamics, Volume 1: Proceedings of the 35th IMAC, A Conference and Exposition on Structural Dynamics 2017*, chapter 6, pages 55–68. Springer International Publishing, Cham, 2017.

R. R. Craig. Coupling of substructures for dynamic analysis: An overview. In *Proceedings of the 41st AIAA/ASME/ASCE/AHS/ASC Structures, Structural Dynamics, and Materials Conference*, Atlanta, 2000.

R. R. Craig and M. C. C. Bampton. Coupling of substructures for dynamic analyses. *AIAA Journal*, 6(7):1313–1319, 1968.

R. R. Craig and A. J. Kurdila. *Fundamentals of structural dynamics*. John Wiley & Sons, 2. edition, 2006.

E. F. Crawley and K. J. O'Donnell. Identification of nonlinear system parameters in joints using the force-state mapping technique. *AIAA Journal*, Paper 86-1:659–667, 1986.

L. S. Czarnecki. What is wrong with the Budeanu concept of reactive and distortion power and why it should be abandoned. *IEEE Transactions on Instrumentation and Measurement*, IM-36(3):834–837, 1987.

L. S. Czarnecki. Energy flow and power phenomena in electrical circuits: Illusions and reality. *Electrical Engineering (Archiv für Elektrotechnik)*, 82(3-4):119–126, 2000.

W. Dahmen and A. Reusken. *Numerik für Ingenieure und Naturwissenschaftler*. Springer-Verlag, Berlin, 2. edition, 2008.

H. de Bellescize. *La réception synchrone*. E. Chiron, Paris, 1932.

D. De Klerk, D. J. Rixen, and S. N. Voormeeren. General framework for dynamic substructuring: History, review and classification of techniques. *AIAA Journal*, 46(5):1169–1181, 2008.

L. Della Flora and H. A. Gründling. Time domain sinusoidal acceleration controller for an electrodynamic shaker. *IET Control Therory and Applications*, 2(12):1044–1053, 2008.

V. Denis, M. Jossic, C. Giraud-Audine, B. Chomette, A. Renault, and O. Thomas. Identication of nonlinear modes using phase-locked-loop experimental continuation and normal form. *Mechanical Systems and Signal Processing*, 106(June):430–452, 2018.

T. Detroux. *Performance and Robustness of Nonlinear Systems Using Bifurcation Analysis*. PhD thesis, Université de Liège, 2016.

T. Detroux, L. Renson, L. Masset, and G. Kerschen. The harmonic balance method for bifurcation analysis of large-scale nonlinear mechanical systems. *Comput. Methods Appl. Mech. Eng.*, 296:18–38, 2015.

A. Dhooge, W. Govaerts, and Y. A. Kuznetsov. MATCONT: A MATLAB package for numerical bifurcation analysis of ODEs. *ACM Transactions on Mathematical Software*, 29(2):141–164, 2003.

G. Duffing. *Erzwungene Schwingungen bei veränderlicher Eigenfrequenz und ihre technische Bedeutung*. Vieweg, Braunschweig, 1918.

D. A. Ehrhardt and M. S. Allen. Measurement of nonlinear normal modes using multi-harmonic stepped force appropriation and free decay. *Mechanical Systems and Signal Processing*, 76-77:612–633, 2016.

C. Ehrlich. *Modellierung der Fügestellendämpfung in zusammengesetzten Strukturen*. Dissertation, University of Stuttgart, 2016.

M. Eriten, M. Kurt, G. Luo, D. M. McFarland, L. A. Bergman, and A. F. Vakakis. Nonlinear system identification of frictional effects in a beam with a bolted joint connection. *Mechanical Systems and Signal Processing*, 39(1):245–264, 2013.

D. J. Ewins. *Modal testing: Theory, practice and application.* Research Studies Press Ltd., Baldock, 2. edition, 2000.

D. J. Ewins, B. Weekes, and A. D. Carri. Modal testing for model validation of structures with discrete nonlinearities. *Philosophical Transactions of the Royal Society A: Mathematical , Physical and Engineering Sciences*, 373(2051), 2015.

M. Fan, M. Clark, and Z. C. Feng. Implementation and stability study of phase-locked-loop nonlinear dynamic measurement systems. *Communications in Nonlinear Science and Numerical Simulation*, 12(7):1302–1315, 2007.

M. Feldman. Non-linear system vibration analysis using Hilbert transform - i. free vibration analysis method 'freevib'. *Mechanical Systems and Signal Processing*, 8(2):119–127, 1994.

U. Fuellekrug and D. Goege. Identification of weak non-linearities within complex aerospace structures. *Aerospace Science and Technology*, 23(1): 53–62, 2012.

R. García and R. Pérez. Dynamic atomic force microscopy methods. *Surface Science Reports*, 47:197–301, 2002.

F. M. Gardner. *Phaselock techniques.* Wiley-Interscience, Hoboken, 3. edition, 2005.

L. Gaul and J. Lenz. Nonlinear dynamics of structures assembled by bolted joints. *Acta Mechanica*, 125:169–181, 1997.

L. Gaul and R. Nitsche. The role of friction in mechanical joints. *Applied Mechanics Reviews*, 54(2), 2001.

M. Géradin and D. J. Rixen. *Mechanical vibrations: Theory and application to structural dynamics.* Wiley, Chichester, 3. edition, 2015.

C. Gibert. Fitting measured frequency response using non-linear modes. *Mechanical Systems and Signal Processing*, 17(1):211–218, 2003.

M. Guskov and F. Thouverez. Harmonic balance-based approach for quasi-periodic motions and stability analysis. *Journal of Vibration and Acoustics*, 134(3):031003, 2012.

G. Haller and S. Ponsioen. Nonlinear normal modes and spectral sub-manifolds: Existence, uniqueness and use in model reduction. *Nonlinear Dynamics*, 86(3):1493–1534, 2016.

T. L. Hill, A. Cammarano, S. A. Neild, and D. J. Wagg. Relating backbone curves to the forced responses of nonlinear systems. In G. Kerschen, editor, *Nonlinear Dynamics, Volume 1, Proceedings of the 34th IMAC, A Conference and Exposition on Structural Dynamics 2016*, chapter 9, pages 113–122. Springer, Cham, 2016.

G.-C. Hsieh and J. C. Hung. Phase-locked loop techniques - A survey. *IEEE Transactions on Industrial Electronics*, 43(6):609–615, 1996.

N. Huang, H. Shih, C. Tung, S. Long, N. Yen, Q. Zheng, M. Wu, Z. Shen, and H. Liu. The empirical mode decomposition and the Hilbert spectrum for nonlinear and non-stationary time series analysis. *Proceedings of the Royal Society A: Mathematical, Physical and Engineering Sciences*, 454 (1971):995, 903, 1998.

P. Huchler. *Die Harmonische Balance Methode zur Simulation der Dynamik von Nutzfahrzeugen mit nichtlinearen Lagerelementen*. Master thesis, University of Stuttgart, 2018.

R. A. Ibrahim. *Vibro-impact dynamics: modeling, mapping and applications*, volume 43 of *Lecture Notes in Applied and Computational Mechanics*. Springer Science & Business Media, 2009.

R. Isermann and M. Münchhof. *Identification of dynamic systems: An introduction with applications*. Springer Science & Business Media, 2010.

M. Jerschl, D. Süß, and K. Willner. Numerical continuation methods for the concept of non-linear normal modes. In F. N. Catbas, editor, *Dynamics of Civil Structures, Volume 4*, pages 19–26, Cham, 2014a. Springer.

M. Jerschl, D. Süß, K. Willner, and M. Jerschl. Path continuation for the concept of non-linear normal modes using a normal flow algorithm. In *Proceedings of ISMA*, pages 3059–3064, Leuven, 2014b.

D. Jordan, R. W. Miksad, and E. J. Powers. Implementation of the continuous wavelet transform for digital time series analysis. *Review of Scientific Instruments*, 68(3):1484, 1997.

H. Kauderer. *Nichtlineare Mechanik*. Springer, Berlin, 1958.

G. Kerschen, J.-C. Golinval, and K. Worden. Theoretical and experimental identification of a non-linear beam. *Journal of Sound and Vibration*, 244 (4):597–613, 2001.

G. Kerschen, V. Lenaerts, and J. C. Golinval. Identification of a continuous structure with a geometrical non-linearity. Part I: Conditioned reverse path method. *Journal of Sound and Vibration*, 262(4):889–906, 2003.

G. Kerschen, J.-C. Golinval, A. F. Vakakis, and L. A. Bergman. The method of proper orthogonal decomposition for dynamical characterisation and order reduction of mechanical systems: An overview. *Nonlinear Dynamics*, 41:147–169, 2005.

G. Kerschen, K. Worden, A. F. Vakakis, and J.-C. Golinval. Past, present and future of nonlinear system identification in structural dynamics. *Mechanical Systems and Signal Processing*, 20(3):505–592, apr 2006.

G. Kerschen, M. Peeters, J. C. Golinval, and A. F. Vakakis. Nonlinear normal modes, part I: A useful framework for the structural dynamicist. *Mechanical Systems and Signal Processing*, 23(1):170–194, 2009.

G. Kerschen, M. Peeters, J. C. Golinval, and C. Stéphan. Nonlinear modal analysis of a full-scale aircraft. *Journal of Aircraft*, 50(5):1409–1419, 2013.

H. K. Khalil. *Nonlinear Systems*. Prentice-Hall, New Jersey, 2. edition, 1996.

A. A. Khan and N. S. Vyas. Application of Volterra and Wiener theories for nonlinear parameter estimation in a rotor-bearing system. *Nonlinear Dynamics*, 24(3):285–304, 2001.

H. B. Khenous, P. Laborde, and Y. Renard. Mass redistribution method for finite element contact problems in elastodynamics. *European Journal of Mechanics, A/Solids*, 27(5):918–932, 2008.

M. Krack. *The concept of nonlinear modes applied to friction-damped systems.* Dissertation, Leibniz Universität Hannover, 2014.

M. Krack. Nonlinear modal analysis of nonconservative systems: Extension of the periodic motion concept. *Computers and Structures*, 154:59–71, 2015.

M. Krack, L. Panning-von Scheidt, and J. Wallaschek. A method for nonlinear modal analysis and synthesis: Application to harmonically forced and self-excited mechanical systems. *Journal of Sound and Vibration*, 332(25):6798–6814, 2013.

M. Krack, L. Panning-von Scheidt, and J. Wallaschek. On the interaction of multiple traveling wave modes in the flutter vibrations of friction-damped tuned bladed disks. *Journal of Engineering for Gas Turbines and Power*, 139(4):042501, 2016.

M. Krack, L. Salles, and F. Thouverez. Vibration prediction of bladed disks coupled by friction joints. *Archives of Computational Methods in Engineering*, 24(3):589–636, 2017.

N. M. Krylov and N. N. Bogoliubov. *Introduction to Non-Linear Mechanics.* Princeton University Press, London, 1936.

M. Kurt, M. Eriten, D. M. McFarland, L. A. Bergman, and A. F. Vakakis. Methodology for model updating of mechanical components with local nonlinearities. *Journal of Sound and Vibration*, 357:331–348, 2015.

D. Laxalde and F. Thouverez. Complex non-linear modal analysis for mechanical systems : Application to turbomachinery bladings with friction interfaces. *Journal of Sound and Vibration*, 322:1009–1025, 2009.

D. Laxalde, L. Salles, L. Blanc, and F. Thouverez. Non-linear modal analysis for bladed disks with friction contact interfaces. *Proceedings of ASME Turbo Expo*, pages 457–467, 2008.

Y. S. Lee, F. Nucera, A. F. Vakakis, D. M. McFarland, and L. A. Bergman. Periodic orbits, damped transitions and targeted energy transfers in oscillators with vibro-impact attachments. *Physica D: Nonlinear Phenomena*, 238(18):1868–1896, 2009.

Y. S. Lee, A. F. Vakakis, D. M. McFarland, and L. A. Bergman. Non-linear system identification of the dynamics of aeroelastic instability suppression based on targeted energy transfers. *Aeronautical Journal*, 114(1152): 61–82, 2010.

R. I. Leine and H. Nijmeijer. *Dynamics and Bifurcations of Non-Smooth Mechanical Systems*, volume 18 of *Lecture Notes in Applied and Computational Mechanics*. Springer-Verlag, Berlin Heidelberg New-York, 2004.

V. Lenaerts, G. Kerschen, and J. C. Golinval. Proper orthogonal decomposition for model updating of non-linear mechanical systems. *Mechanical Systems and Signal Processing*, 15(1):31–43, 2001.

I. J. Leontaritis and S. A. Billings. Input-output parametric models for non-linear systems Part I: Deterministic non-linear systems. *International Journal of Control*, 41(2):303–328, 1985a.

I. J. Leontaritis and S. A. Billings. Input-output parametric models for non-linear systems Part II: Stochastic non-linear systems. *International Journal of Control*, 41(2):329–344, 1985b.

A. M. Ljapunov. *The general problem of the stability of motion*. Taylor & Francis, London, 1992.

J. M. Londono, S. A. Neild, and J. E. Cooper. Identification of backbone curves of nonlinear systems from resonance decay responses. *Journal of Sound and Vibration*, 348:224–238, 2015.

S. Marchesiello and L. Garibaldi. A time domain approach for identifying nonlinear vibrating structures by subspace methods. *Mechanical Systems and Signal Processing*, 22(1):81–101, 2008.

S. F. Masri and T. K. Caughey. A nonparametric identification technique for nonlinear dynamic problems. *Journal of Applied Mechanics*, 46(2): 433, 1979.

S. F. Masri, S. H, and C. T. K. Nonparametric identification of nearly arbitrary nonlinear systems. *Journal of Applied Mechanics*, 49(September): 619–628, 1982.

K. G. McConnel and P. S. Varoto. *Vibration Testing: Theory and Practice*. John Wiley & Sons Inc., Hoboken, 2. edition, 2008.

S. Meyer and M. Link. Modelling and updating of local non-linearities using frequency response residuals. *Mechanical Systems and Signal Processing*, 17(1):219–226, 2003.

Y. V. Mikhlin and K. V. Avramov. Nonlinear normal modes for vibrating mechanical systems. Review of theoretical developments. *Applied Mechanics Reviews*, 63(6):060802–1–060802–21, 2010.

K. Mohammad, K. Worden, and G. Tomlinson. Direct parameter estimation for linear and non-linear structures. *Journal of Sound and Vibration*, 152(3):471–499, 1992.

S. Mojrzisch, I. Ille, and J. Wallaschek. Phase controlled frequency response measurement for nonlinear vibration systems. In *Proceedings of ICSV*, Bangkok, Thailand, 2013.

F. Morlock. *Force Control of an Electrodynamic Shaker for Experimental Testing of Nonlinear Mechanical Structures*. Master thesis, University of Stuttgart, 2015.

J. E. Mottershead and M. I. Friswell. Model updating in structural dynamics: A survey. *Journal of Sound and Vibration*, 167(2):347–375, 1993.

S. Nacivet, C. Pierre, F. Thouverez, and L. Jezequel. A dynamic Lagrangian frequency-time method for the vibration of dry-friction-damped systems. *Journal of Sound and Vibration*, 265(1):201–219, 2003.

A. H. Nayfeh. *Nonlinear interactions: Analytical, computational and experimental methods*. Wiley, New York, 2000.

A. D. Niet. *Step-size control and corrector methods in numerical continuation of ocean circulation and fill-reducing orderings in multilevel ILU methods*. Master thesis, University of Groningen, 2002.

J. P. Noël and G. Kerschen. Frequency-domain subspace identification for nonlinear mechanical systems. *Mechanical Systems and Signal Processing*, 40(2):701–717, 2013.

J. P. Noël and G. Kerschen. Nonlinear system identification in structural dynamics: 10 more years of progress. *Mechanical Systems and Signal Processing*, 83:2–35, 2016.

J. P. Noël, S. Marchesiello, and G. Kerschen. Subspace-based identification of a nonlinear spacecraft in the time and frequency domains. *Mechanical Systems and Signal Processing*, 43(1-2):217–236, 2014.

J.-P. Noël, L. Renson, C. Grappasonni, and G. Kerschen. Identification of nonlinear normal modes of engineering structures under broadband forcing. *Mechanical Systems and Signal Processing*, 74:95–110, 2016.

M. Peeters, R. Viguié, G. Sérandour, G. Kerschen, and J. C. Golinval. Nonlinear normal modes, part II: Toward a practical computation using numerical continuation techniques. *Mechanical Systems and Signal Processing*, 23(1):195–216, 2009.

M. Peeters, G. Kerschen, and J. C. Golinval. Modal testing using nonlinear normal modes: An experimental demonstration. In *Proceedings of ISMA*, pages 3221–3236, Leuven, 2010.

M. Peeters, G. Kerschen, and J. C. Golinval. Dynamic testing of nonlinear vibrating structures using nonlinear normal modes. *Journal of Sound and Vibration*, 330(3):486–509, 2011.

E. Pesheck, C. Pierre, and S. W. Shaw. A new Galerkin-based approach for accurate non-linear normal modes through invariant manifolds. *Journal of Sound and Vibration*, 249(5):971–993, 2002.

S. Peter and R. I. Leine. Excitation power quantities in phase resonance testing of nonlinear systems with phase-locked-loop excitation. *Mechanical Systems and Signal Processing*, 96:139–158, 2017.

S. Peter, P. Reuss, and L. Gaul. Identification of sub- and higher harmonic vibrations in vibro-impact systems. In G. Kerschen, editor, *Nonlinear Dynamics, Volume 2: Proceedings of the 32nd IMAC, A Conference and Exposition on Structural Dynamics, 2014*, pages 131–140. Springer, Cham, 2014.

S. Peter, A. Grundler, P. Reuss, L. Gaul, and R. I. Leine. Towards finite element model updating based on nonlinear normal modes. In G. Kerschen, editor, *Nonlinear Dynamics, Volume 1, Proceedings of the 33rd IMAC, A Conference and Exposition on Structural Dynamics 2015*, pages 209–217. Springer, Cham, 2015.

S. Peter, R. Riethmüller, and R. I. Leine. Tracking of backbone curves of nonlinear systems using phase-locked-loops. In G. Kerschen, editor, *Nonlinear Dynamics, Volume 1, Proceedings of the 34th IMAC, A Conference and Exposition on Structural Dynamics, 2016*, chapter 11, pages 107–120. Springer, 2016.

S. Peter, M. Scheel, M. Krack, and R. I. Leine. Synthesis of nonlinear frequency responses with experimentally extracted nonlinear modes. *Mechanical Systems and Signal Processing*, 101:498–515, 2018a.

S. Peter, F. Schreyer, and R. I. Leine. A method for numerical and experimental nonlinear modal analysis of nonsmooth systems. *Mechanical Systems and Signal Processing*, in prep., 2018b.

E. P. Petrov. Analysis of flutter-induced limit cycle oscillations in gas-turbine structures with friction, gap, and other nonlinear contact interfaces. *Journal of Turbomachinery*, 134(6):061018, 2012.

E. P. Petrov and D. J. Ewins. Analytical formulation of friction interface elements for analysis of nonlinear multi-harmonic vibrations of bladed discs. *Proceedings of ASME Turbo Expo*, 2002.

C. Pierre, D. Jiang, and S. Shaw. Nonlinear normal modes and their application in structural dynamics. *Mathematical Problems in Engineering*, pages 1–15, 2006.

M. F. Platten, J. R. Wright, G. Dimitriadis, and J. E. Cooper. Identification of multi-degree of freedom non-linear systems using an extended modal space model. *Mechanical Systems and Signal Processing*, 23(1): 8–29, 2009.

H. Poincaré. *Solutions périodiques. Non-existence des intégrales uniformes. Solutions asymptotiques.* Gauthier-Villars, Paris, 1892.

L. Renson and G. Deli. Finite element computation of nonlinear normal modes of nonconservative systems. In *Proceedings of ISMA*, pages 2519–2534, Leuven, 2012.

L. Renson, G. Kerschen, and A. Newerla. Nonlinear modal analysis of the Smallsat spacecraft. In D. Adams, G. Kerschen, and A. Carrella, editors, *Topics in Nonlinear Dynamics, Volume 3: Proceedings of the 30th IMAC, A Conference on Structural Dynamics, 2012*, pages 45–60. Springer, New York, 2012.

L. Renson, A. Gonzalez-Buelga, D. Barton, and S. Neild. Robust identification of backbone curves using control-based continuation. *Journal of Sound and Vibration*, 367:145–158, 2016.

P. Reuss, B. Zeumer, J. Herrmann, and L. Gaul. Consideration of interface damping in dynamic substructuring. In R. Mayes, D. Rixen, D. T. Griffith, D. De Klerk, S. Chauhan, S. N. Voormeeren, and M. S. Allen, editors, *Topics in Experimental Dynamics Substructuring and Wind Turbine Dynamics, Volume 2: Proceedings of the 30th IMAC, A Conference on Structural Dynamics, 2012*, pages 81–88. Springer, New York, 2012.

C. Richards and R. Singh. Identification of multi-degree-of-freedom nonlinear systems under random excitations by the reverse path spectral method. *Journal of Sound and Vibration*, 213(4):673–708, 1998.

R. M. Rosenberg. Normal modes of nonlinear dual-mode systems. *Journal of Applied Mechanics*, 27(2):263–268, 1960.

M. Scheel, G. Kleyman, A. Tatar, M. R. W. Brake, S. Peter, J.-P. Noël, M. S. Allen, and M. Krack. Nonlinear system identification: A comparison of nonlinear modal testing and state-space model identification. *Journal of Sound and Vibration*, in prep., 2018a.

M. Scheel, S. Peter, R. I. Leine, and M. Krack. A phase resonance approach for modal testing of structures with nonlinear dissipation. *Journal of Sound and Vibration*, under rev., 2018b.

F. Schreyer and R. I. Leine. A mixed shooting-harmonic balance method for unilaterally constrained mechanical systems. *Archive of Mechanical Engineering*, 63(2):297–314, 2016a.

F. Schreyer and R. I. Leine. Mixed Shooting-HBM : A periodic solution solver for unilaterally constrained systems. In *Proceedings of IMSD*, Montreal, 2016b.

C. W. Schwingshackl, E. P. Petrov, and D. J. Ewins. Measured and estimated friction interface parameters in a nonlinear dynamic analysis. *Mechanical Systems and Signal Processing*, 28:574–584, 2012.

D. J. Segalman, D. L. Gregory, M. J. Starr, B. R. Resor, M. D. Jew, J. P. Lauffer, and N. M. Ames. Handbook on Dynamics of Jointed Structures. Technical report, Sandia National Laboratories, Albuquerque, 2009.

S. Setio, H. D. Setio, and L. Jezequel. Modal analysis of nonlinear multi-degree-of-freedom structure. *The International Journal of Analytical and Experimental Modal Analysis*, 7(0):75–93, 1992.

R. Seydel. *Practical bifurcation and stability analysis.* Springer Science & Business Media, New York, 3. edition, 2009.

A. D. Shaw, T. L. Hill, S. A. Neild, and M. I. Friswell. Experimental identification of a structure with internal resonance. In G. Kerschen, editor, *Nonlinear Dynamics, Volume 1, Proceedings of the 34th IMAC, A Conference and Exposition on Structural Dynamics 2016*, pages 37–45. Springer, Bethel, 2016.

S. W. Shaw and C. Pierre. Non-linear normal modes and invariant manifolds. *Journal of Sound and Vibration*, 150(1):170–173, 1991.

D. Shmilovitz. On the definition of total harmonic distortion and its effect on measurement interpretation. *IEEE Transactions on power delivery*, 20(1):526–528, 2005.

J. C. Slater. A numerical method for determining nonlinear normal modes. *Nonlinear Dynamics*, 10(1):19–30, 1996.

I. Sokolov and V. Babitsky. Phase control of self-sustained vibration. *Journal of Sound and Vibration*, 248(4):725–744, 2001.

W. J. Staszewski. Identification of damping in MDOF systems using time-scale decomposition. *Journal of Sound and Vibration*, 203(2):283–305, 1997.

W. J. Staszewski. Analysis of non-linear systems using wavelets. *Proceedings of the Institution of Mechanical Engineers Part C – Journal of Mechanical Engineering Science*, 214:1339–1353, 2000.

D. M. Storer. *Dynamic analysis of nonlinear structures using higher order frequency response functions*. PhD thesis, University of Manchester, 1991.

D. Süß. *Multi-Harmonische-Balance-Methoden zur Untersuchung des Übertragungsverhaltens von Strukturen mit Fügestellen*. Dissertation, Friedrich-Alexander-Universität Erlangen-Nürnberg, 2016.

S. Svensson. *Power measurement techniques for non-sinusoidal conditions*. PhD thesis, Chalmers University of Technology, 1999.

W. Szemplinska-Stupnicka. The modified single mode method in the investigations of the resonant vibration of non-linear systems. *Journal of Sound and Vibration*, 63(4):475–489, 1979.

W. Szemplinska-Stupnicka. Non-linear normal modes and the generalized Ritz method in the problems of vibrations of non-linear elastic continous systems. *Int. J. Non-Linear Mechanics*, 18(2):149–165, 1983.

I. Tawfiq and T. Vinh. Nonlinear behaviour of structures using the Volterra Series – Signal processing and testing methods. *Nonlinear Dynamics*, 37: 129–149, 2004.

F. Thouverez. Presentation of the ECL benchmark. *Mechanical Systems and Signal Processing*, 17(1):195–202, jan 2003.

F. Thouverez and L. Jezequel. Identification of Narmax models on a modal base. *Journal of Sound and Vibration*, 189(2):193–213, 1996.

E. E. Ungar. Loss factors of viscoelastic systems in terms of energy concepts. *The Journal of the Acoustical Society of America*, 34(7):741, 1962.

A. F. Vakakis. Non-linear normal modes (NNMs) and their applications in vibration theory: An overview. *Mechanical Systems and Signal Processing*, 11(1):3–22, 1997.

A. F. Vakakis, L. I. Manevitch, V. N. Pilipchuk, and A. A. Zevin. *Nonlinear modes and localization in nonlinear systems*. John Wiley & Sons Inc., New York, 1996.

G. Von Groll and D. Ewins. The harmonic balance method with arclength continuation in rotor/stator contact problems. *Journal of Sound and Vibration*, 241(2):223–233, 2001.

S. N. Voormeeren, P. L. C. van der Valk, and D. J. Rixen. Practical aspects of dynamic substructuring in wind turbine engineering. In T. Proulx, editor, *Structural Dynamics and Renewable Energy, Volume 1, Proceedings of the 28th IMAC*, pages 163–185. Springer, Cham, 2011.

K. Worden and R. J. Barthorpe. Identification of hysteretic systems using NARX models, part I: Evolutionary identification. In T. Simmermacher, S. Cogan, L. G. Horta, and R. Barthorpe, editors, *Topics in Model Validation and Uncertainty Quantification, Volume 4: Proceedings of the 30th IMAC, A Conference on Structural Dynamics, 2012*, pages 49–56. Springer, New York, 2012.

K. Worden and P. L. Green. A machine learning approach to nonlinear modal analysis. *Mechanical Systems and Signal Processing*, 84:34–53, 2017.

K. Worden and G. R. Tomlinson. *Nonlinearity in structural dynamics: Detection, identification and modelling.* CRC Press, Boca Raton, 2001.

K. Worden, R. J. Barthorpe, and J. J. Hensman. Identification of hysteretic systems using NARX models, part II: A Bayesian approach. In T. Simmermacher, S. Cogan, L. G. Horta, and R. Barthorpe, editors, *Topics in Model Validation and Uncertainty Quantification, Volume 4: Proceedings of the 30th IMAC, A Conference on Structural Dynamics, 2012*, pages 57–65. Springer, New York, 2012.

J. R. Wright, J. E. Cooper, and M. J. Desforges. Normal-mode force appropriation – Theory and application. *Mechanical Systems and Signal Processing*, 13(2):217–240, 1999.

J. L. Zapico-Valle, M. García-Diéguez, and R. Alonso-Camblor. Nonlinear modal identification of a steel frame. *Engineering Structures*, 56:246–259, 2013.